OPEN ACCESS

University of BRISTOL

# This electronic thesis or dissertation has been downloaded from Explore Bristol Research, http://research-information.bristol.ac.uk

*Author:*
**Mfon, Rebecca**

*Title:*
**Characterisation of silver and zinc oxide nanoparticles biosynthesized using Ocimum gratissimum and Vernonia amygdalina plant leaf extracts**

**General rights**
Access to the thesis is subject to the Creative Commons Attribution - NonCommercial-No Derivatives 4.0 International Public License. A copy of this may be found at https://creativecommons.org/licenses/by-nc-nd/4.0/legalcode This license sets out your rights and the restrictions that apply to your access to the thesis so it is important you read this before proceeding.

**Take down policy**
Some pages of this thesis may have been removed for copyright restrictions prior to having it been deposited in Explore Bristol Research. However, if you have discovered material within the thesis that you consider to be unlawful e.g. breaches of copyright (either yours or that of a third party) or any other law, including but not limited to those relating to patent, trademark, confidentiality, data protection, obscenity, defamation, libel, then please contact collections-metadata@bristol.ac.uk and include the following information in your message:

• Your contact details
• Bibliographic details for the item, including a URL
• An outline nature of the complaint

Your claim will be investigated and, where appropriate, the item in question will be removed from public view as soon as possible.

OPEN ACCESS

University of BRISTOL

# This electronic thesis or dissertation has been downloaded from Explore Bristol Research, http://research-information.bristol.ac.uk

*Author:*
**Mfon, Rebecca**

*Title:*
**Characterisation of silver and zinc oxide nanoparticles biosynthesized using Ocimum gratissimum and Vernonia amygdalina plant leaf extracts**

**General rights**
Access to the thesis is subject to the Creative Commons Attribution - NonCommercial-No Derivatives 4.0 International Public License. A copy of this may be found at https://creativecommons.org/licenses/by-nc-nd/4.0/legalcode This license sets out your rights and the restrictions that apply to your access to the thesis so it is important you read this before proceeding.

**Take down policy**
Some pages of this thesis may have been removed for copyright restrictions prior to having it been deposited in Explore Bristol Research. However, if you have discovered material within the thesis that you consider to be unlawful e.g. breaches of copyright (either yours or that of a third party) or any other law, including but not limited to those relating to patent, trademark, confidentiality, data protection, obscenity, defamation, libel, then please contact collections-metadata@bristol.ac.uk and include the following information in your message:

• Your contact details
• Bibliographic details for the item, including a URL
• An outline nature of the complaint

Your claim will be investigated and, where appropriate, the item in question will be removed from public view as soon as possible.

# Characterisation of Silver and zinc oxide nanoparticles biosynthesized using Ocimum gratissimum and Vernonia amygdalina plant leaf extracts


## By

**Rebecca Emmanuel Mfon**

**(School of Physics, H.H. Wills Physics Laboratory)**



*A thesis submitted to the University of Bristol in accordance with the requirements for award of the degree of **Doctor of Philosophy** in the Faculty of Science*

*September 2018* *~ 41,000 words*

# Abstract

The need to reduce environmental pollution and make planet Earth safer for her inhabitants has led to the adoption of scientific methods which yield safer by-products. Nanoparticles which have in the Science world recently attracted much attention, have been synthesized and put into a wide range of applications but the main concern has been to ensure that the by-products from such processes are less toxic, and that their sizes are controlled for specific applications. Though chemical and Physical methods can be used for their synthesis, the biosynthesis option reported to be fast, cheap and environmentally friendly and more recently the use of plant leaf extracts has been preferred because the plant extracts through their inherent biomolecules do not only make the nanoparticles, they cap and can stabilize them.

In view of this, this work studied the effect of *Ocimum gratissimum* (Og) and *Vernonia amygdalina* (Va) plant leaf extracts on the synthesis of silver and zinc oxide (ZnO) nanoparticles. The resulting nanostructures were characterized using optical spectroscopy and electron microscopy.

Boosting food production can make it more affordable especially to the low-income earners in any society therefore this work also investigated the interactive effect of pH of synthesis and concentration of colloidal solution of the ZnO nanoparticles (used as Nano fertilizer) on the growth parameters (seedling characteristics and vegetative growth) of Amaranthus cruentus. *Amaranthus cruentus* is widely eaten in my country Nigeria but is still not within the reach of the average Nigerian. This research therefore used the zinc oxide nanofertilizer to grow this plant (A. cruentus) and determined the plant treatments which give best seedling characteristics or enhance the vegetative growth of the plants. The critical limit for the nanoparticles used were also determined. While the Amaranth studies showed that the ZnO Nano fertilizer enhanced the growth of the plant, it was discovered that beyond 500mg/L concentration, the colloidal solution of the ZnO nanofertilizer became toxic and even resulted in chlorosis in some cases.

Furthermore, from available literature, it is obvious that not much has been done on the electrodeposition of silver on gold in the presence of plant leaf extracts particularly the ones listed for this research. This therefore was also explored using cyclic voltammetry and chronoamperometry techniques and the morphology of the silver thin films from aqueous

silver nitrate in the presence of each of the chosen two leaf extracts was examined using the Atomic Force Microscope (AFM). The electrodeposition experiment gave silver films whose thickness and grains sizes were refined and found to be plant leaf extract dependent.

# Acknowledgements

I thank Almighty God for preserving my life and enabling me to complete this programme despite all the challenges I faced. I am very grateful to my supervisors Dr Andrei Sarua and Dr Simon R. Hall whose guidance and valuable suggestions culminated in the success of this research. I also appreciate Dr Natasa Vasiljevic who supervised the electrochemistry aspect of this research. I thank Professor Ngozi Ifeoma Odiaka of the Federal University of Agriculture Makurdi, Benue State Nigeria who willingly agreed to collaborate with us for the *Amaranthus cruentus* studies and to Dr Felix Ugese of the same University who put me through the statistical methods used for the analysis of the data acquired from the Amaranth studies.

I want to thank the School of Physics University of Bristol and the University of Bristol Alumni (DARO) for their financial assistance when I needed it most. I appreciate the Vice Chancellors of the Federal University Lafia (FULafia) Nasarawa state Nigeria (past and present) Professor Ekanem Ikpi Braide and Professor Mohammed Sanusi Liman for their administrative roles (regarding this sponsorship) as the chief executives of FULafia during the period of my study leave in the UK and the Tertiary Education Trust Fund (TETfund) for three years sponsoring of this PhD programme. I acknowledge the Board of Trustees Hodgkin House 3 Meridian place Bristol UK for the help I received regarding my accommodation in my fourth year of studies. I am grateful to my colleagues in the Micro- and Nano-structural research group who tutored me on the use of some software for my data analysis and most importantly our Physics Graduate Dean, Professor Walther Schwarzacher for having a listening ear and his empathy and prompt attention when it was most needed. This whole PhD programme would have been an effort in futility but for my dear mother Mrs. Esther Isaac Ibok, and siblings Mrs Emma Okpongete, Dr (Mrs) Rosemary Nkang, Mrs Sarah Ekpo, and Dr Andrew Ibok who prayed earnestly for me and were not tired of calling to encourage me not to give up especially when I almost threw in the towel. I appreciate my children Messrs Wilson Mfon, Cicero Mfon, Emmanuel Mfon and my only daughter Mrs. Annie Titiloye and their spouses for their support too.

Finally, I remember my late father Chief Isaac Ibok who unfortunately is not alive to witness his dream for my career come through. I want to say a big Thank you to you all!

# Author's Declaration

I declare that the work in this dissertation was carried out in accordance with the requirements of the University of Bristol's regulations and code of practice for Research Degree programmes and that this dissertation has not been submitted for any other academic award to any other University either in the United Kingdom or Overseas except the University of Bristol. Except where indicated by specific reference in the text, the work is the author's own work. Work done in collaboration with or assistance of, others, is indicated as such. Any views expressed in the dissertation are those of the author.

Rebecca Emmanuel Mfon

21st September 2018

**UNIVERSITY OF BRISTOL THESIS DEPOSIT AGREEMENT**

**Name: Rebecca Emmanuel Mfon**

**Title of Dissertation (the "Thesis"): "Characterization of silver and zinc oxide nanoparticles biosynthesized using Ocimum gratissimum and Vernonia amygdalina plant leaf extracts"**

**Supervisor: Dr Andrei Sarua**

**Department: School of Physics**

**I AGREE AS FOLLOWS**

**1. Library Access**

a. I agree that the Thesis may be made available for consultation in the University of Bristol library and for inter-library lending for use in another library and may be copied in full or in part for any bona fide library or research worker, on the understanding that users shall be made aware of their obligations to me under copyright, i.e. that no quotations or significant extracts may be copied or used without sufficient acknowledgement.

**2. Electronic Access**

*(You may delete these paragraphs if you wish to forego the advantages which this option conveys)*

a. I agree that the Thesis may be made available for consultation in full without charge on the Internet via the University of Bristol's online digital repository of dissertations and with the British Library to be made available via the EThOS system. Rights granted to the University of Bristol and the British Library through this Agreement are non-exclusive. I remain free to publish the Thesis elsewhere in its present version or future versions.

b. I agree that the administrators of the University of Bristol Thesis Repository Service may, without changing content, digitise and migrate the Thesis to any medium or format for the purpose of future preservation and accessibility.

c. I warrant that the Thesis is original and that I am the author and owner of the copyright in the Thesis. I grant the University of Bristol and (where appropriate) the British Library a licence to make available the Thesis in digitised format through the University of Bristol repository and through the British Library via the EThOS system for the purposes of non-commercial research, private study, criticism, review and news reporting, illustration for teaching, and/or other educational purposes in electronic or print form.

d. I warrant that if the Thesis does include any substantial subsidiary material owned by third-party copyright holders, I have sought and obtained permission to include it in any version of my Thesis available in digital format via a stand-alone device or a communications network and that this permission encompasses the rights that I grant to the University of Bristol and to the British Library.

e. I understand and agree that neither the University of Bristol nor (where appropriate) the British Library have any obligation to take legal action on my behalf, or other rights holders, in the event of infringement of intellectual property rights, breach of contract or any other right in the Thesis.

Signed: …… [redacted] …… Dated: 12th February, 2019

# Table of contents

# List of Figures

# List of Tables

# Chapter 1

# Research background, motivation and aim

## 1.1 Introduction

The production of nanoparticles and the creation of thin films for the purpose of producing materials and providing services which can improve man's living condition has taken the centre space in the discourse of scientists. Not only are researchers interested in producing these materials, they are much more concerned about making them using methods whose by-products are not detrimental to man, his health and environment.

Nanoparticles have been produced by physical and chemical methods but the need to adopt a more environmentally benign method has made many researchers opt for the biosynthesis of nanoparticles specifically using plant leaf extracts which is an aspect of this research.

## 1.2 Motivation

In this research, *Ocimum gratissimum* (Og) and *Vernonia amygdalina (Va)* plant leaf extracts were used. Among the plants or herbs used in traditional medicine, these two plants are top of the list and are widely used in Nigeria as food particularly by the natives of the south-eastern region of Nigeria where I come from. There are also a good number of publications which attest to the efficacy of these plant leaf extracts for the treatment of different diseases.

## 1.3 Aim of this research

Beyond the use of these listed two plant leaf extracts for culinary and medicinal purposes, this work hopes to find out what kind of nanostructures these Og and Va plant leaf extracts produce when used for the biosynthesis of silver and zinc oxide nanoparticles and also how the optical properties of these nanoparticles will change with concentration and type of leaf extract used. The electrodeposition of silver thin films on a gold substrate in the presence of leaf extracts has not received much attention. Thus, the electrodeposition of silver on a gold substrate, with and without each of the plant leaf extracts in turn was done and electrodeposition techniques like cyclic voltammetry, chronoamperometry and linear sweep voltammetry was employed. The produced silver and zinc oxide nanostructures were characterised to see the role of the chosen leaf extracts in the created nanostructures.

Sabir et al [1] report that nanoparticles can be used as fertilizers for growing crops In this work, this assertion was explored as the biosynthesized zinc oxide nanoparticles was used as Nano-fertilizer for planting *Amaranthus cruentus* (A. cruentus). The seeding characteristics and vegetative growth, of A. cruentus were studied and the concentration of the ZnO Nano fertilizer which enhanced the growth of this plant was determined. Furthermore, the critical point of the ZnO nanofertilizer (concentration of zinc oxide Nano fertilizer beyond which 50 % of the plants died) was also determined. The outcome of this research hopefully will add to knowledge and probably chart a new course for the two plants *Ocimum gratissimum* and *Vernonia amygdalina*.

## 1.4 Summary of chapters

Because most nanoparticle characterisation apparatus use light, Chapter 2 gives the theoretical background of the research. It discusses earlier atomic models which could not adequately explain the behaviour of light when shone on a material. The explanation goes on to the quantum mechanical model as the one that best describes the behaviour of electrons in a material when light interacts with it. Furthermore, the existence of energy bands in solids as well as the formation of energy band gaps are explained. The role of energy band gaps in the broad classification of materials as conductors,

insulators and semiconductors are also presented. Light absorption by different materials and media and the role played by the dielectric constant and refractive indices of material are also discussed. Plasmon resonance as it applies to bulk materials as well as nanoparticles is explained and the optical properties of light such as reflection, transmission, as well as photoluminescence and the production of infrared (IR) spectra, X-ray diffraction patterns and peaks are also discussed.

A brief theory of electrochemical deposition techniques (cyclic voltammetry, chronoamperometry and linear sweep voltammetry) is also given and a description of the three-electrode electrochemical cell used as well as the reason for the chosen working, reference and counter electrodes are given.

Chapter 3 discusses the apparatus and experimental techniques used for the characterisation of the biosynthesized silver and zinc oxide nanoparticles. It explains how each of the apparatus used functions to enable data collection and shows the method of data acquisition and analysis employed for each sample.

Chapter 4 gives an analysis of the two plants (*Ocimum gratissimum* and *Vernonia amygdalina*) whose leaf extracts were used for this work. It lists their uses in folklore medicine for treating certain ailments and relates their abilities to do so with the results of other researches which studied the phytochemical constituents of the aqueous and ethanolic extracts of these two leaves. It also lists some of their medicinal and health benefits from available literature and expresses the hope that this present research which involves the biosynthesis of silver and zinc oxide nanoparticles using leaf extracts of our chosen plants, will chart a new course for the plant extracts and add to their already known food and medicinal values.

Chapter 5 discusses the biosynthesis of the silver and zinc oxide nanoparticles showing the precursor materials, the preparation of the needed solutions, as well as the imposed experimental conditions and results achieved in each case. It gives data on the two nanoparticles from optical spectroscopy and electron microscopy analysis and discusses the observed features, while Chapter 6 deals with the leaf-based electrodeposition of silver thin films and shows how the response of the analytes used (in a three-electrode

cell) for the Cyclic Voltammetry, Chronoamperometry and Linear Sweep Voltammetry techniques is leaf extract dependent. Chapter 7 illustrates the use of the biosynthesized zinc oxide nanoparticles as nanofertilizer for growing *Amaranthus cruentus* from the seedling stage. It explains the effect of the pH of synthesis of the ZnO nanoparticles and the concentration of colloidal solutions of the ZnO nanoparticles used, on the seedling characteristics and vegetative growth of the studied *Amaranthus cruentus.* It also shows that though this zinc oxide nanofertilizer enhanced the growth parameters of the plant, beyond a certain concentration, the zinc oxide nanofertilizer becomes toxic as is evident by some yellow coloration of some of its leaves. The writeup therefore states this critical level for each type of the applied Nano fertilizer. Finally, chapter 8 gives the summary of the whole work, its main outcomes and makes suggestions for further work.

# Chapter 2

# Theory Background of Research

## 2.1 Introduction

Some models have been used for explaining how solids behave. The Drude model which is a classical model [2] assumes that a metal consists of atoms represented by fixed positive ion cores in the midst of a sea of delocalised electrons (conduction electrons) donated by the constituent atoms (Figure 2.1). An application of an electric field to this system can make the electrons experience a force F = e E and hence an acceleration a and elastic collisions between the electrons and the positive ion cores can occur. This model assumes that the valence electrons of the atoms which make up a crystal can freely move about within the crystal as conduction electrons.

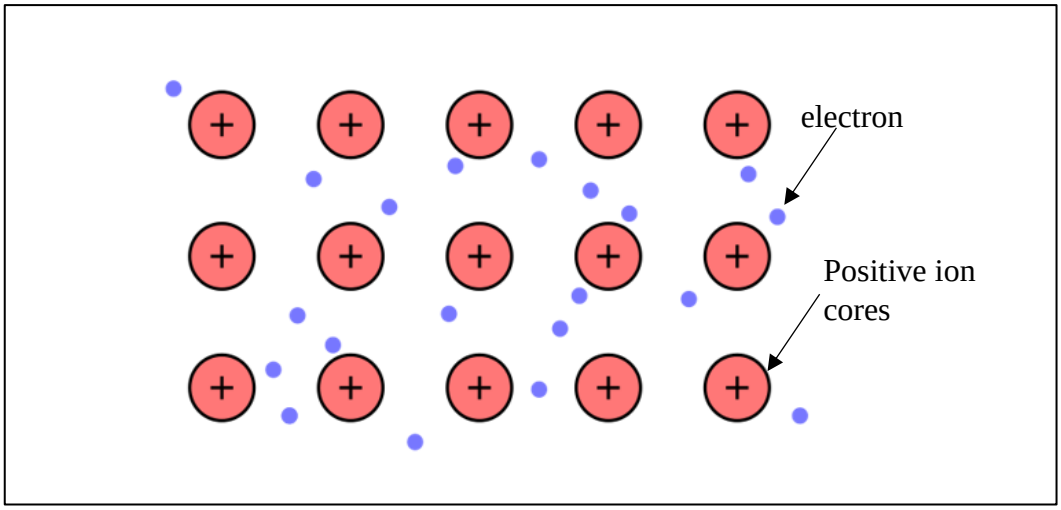


**Figure 2.1**: Illustration of Drude model

Though the Drude model enabled properties of metals such as electrical and heat conductivity as well as reflection to be explained, it could not however account for the Zeeman and Stark effects. This led to an extension which is the Drude - Sommerfeld model. This model agreed with Drude's ideas but considered the energies of electrons to be discrete and used Fermi-Dirac statistics to describe electron behaviour.

The Quantum mechanical concept of conduction by metals assumes that metals contain free electrons which are localised and restricted to a three dimensional well and have quantised energies.

The Hamiltonian which excludes the electrostatic attraction but includes the kinetic term is:

$$\langle H|\psi_n(x)\rangle = -\frac{\hbar^2}{2m}\frac{d^2}{dx^2}\psi_n(x) = E_n\psi_n(x) \qquad (2.1)$$

In one dimension, the solution for Equation 2.1 is of the form:

$\psi_n(x) = A\,Sin\left(\frac{\pi n}{L}\right)x$ and will result in Eigen energy values $E_n$ given as

$$E_n = \frac{\hbar^2}{2m}\left(\frac{\pi n}{L}\right)^2 \qquad \text{(n = 1, 2, 3….)} \qquad (2.2)$$

Equation 2.2 gives the possible levels that electrons can stay in and represents a standing wave with nodes inside a potential well. Thus, for n =1, 2, 3 etc the corresponding L values are $\frac{\lambda}{2}$, $\lambda$, and $\frac{3\lambda}{2}$.

Therefore, electrons in a 3D well will have energy:

$$E(n_x, n_y, n_z) = \frac{\pi^2\hbar^2}{2mL^2}\ \ ({n_x}^2 + {n_y}^2 + {n_z}^2) \qquad (2.3)$$

Thus $\left({n_x}^2 + {n_y}^2 + {n_z}^2\right) = \frac{2mL^2}{\pi^2\hbar^2}\ \ E(n_x, n_y, n_z)$ (2.4)

This gives a large number of energy levels and forms a continuum.

According to Pauli's exclusion principle, no two fermions can have the same set of all four quantum numbers: Thus, it is possible for any two electrons to be in the same energy level, but with different spin components.

The highest energy level where electrons can be found is known as the fermi energy level $E_f$ and defined as the highest possible energy quantum state in which an electron can exist when the metal is at absolute zero temperature. Thus, when energy is given to

a material, the electrons in it get excited but cannot jump to the energy levels directly above them as these are already filled. The only electrons which can jump to the upper levels and contribute to the conduction current are those which are closest to the fermi level. Consequently, solid materials are classified according to the varied abilities of their constituent electrons to do so.

The classification of solid materials as conductors (metals), insulators or semiconductors depend on the relationship between their filled bands and their empty bands. Solid materials are made up of atoms separated a distance r from one another and their energy bands are a function of this separation.

## 2.2 Energy bands in solid materials

Energy bands are formed when the separation between neighbouring atoms in a material decreases and there is some coupling between the atoms and the atomic orbitals in which electrons are arranged such that there is an overlap of their corresponding wave functions. This results in a combined energy, which is less than the sum of the energies of the separate atoms and the system becomes more stable.

Considering any two atoms in a solid separated a distance r from one another; If their separation r decreases, the energy levels of their shells can split into many other energy levels: Any two, levels represented by $E_1$ and $E_2$ can split into many energy levels and overlap as shown in Figure 2.2 creating two regions: one of allowed energy levels and the other of energy levels which are not allowed. The CB region represents the conduction band while the VB region is the valence band.

The gap between these two ( $E_c - E_v$) is the energy band gap $E_g$ which is the difference between the lowest energy of the conduction $E_c$ and highest energy of the valence band $E_v$. The presence of the energy band gap $E_g$ for materials helps in their classification as insulators or semiconductors.

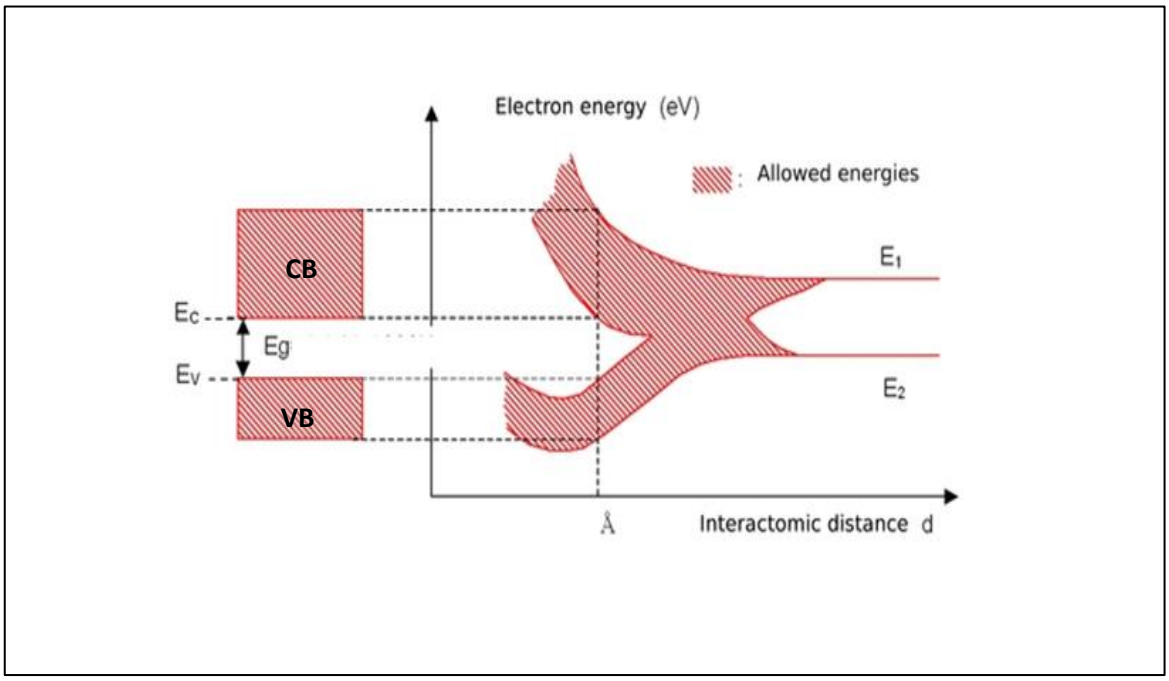


**Figure 2.2** Overlapping of split energy levels of atoms in a silicon crystal to form energy bands [3].

Materials which have large energy gaps are called insulators. Examples of insulators include diamond, plastic, rubber and, glass. Insulators do not conduct electricity but can be made to conduct by the application of very large energies which make them breakdown and begin to conduct.

Conductors have a partially filled band or an overlap of the valence band with the conduction band thus have no energy band gap. These materials are highly conducting and are the metals. Some examples include gold and silver which this research worked with.

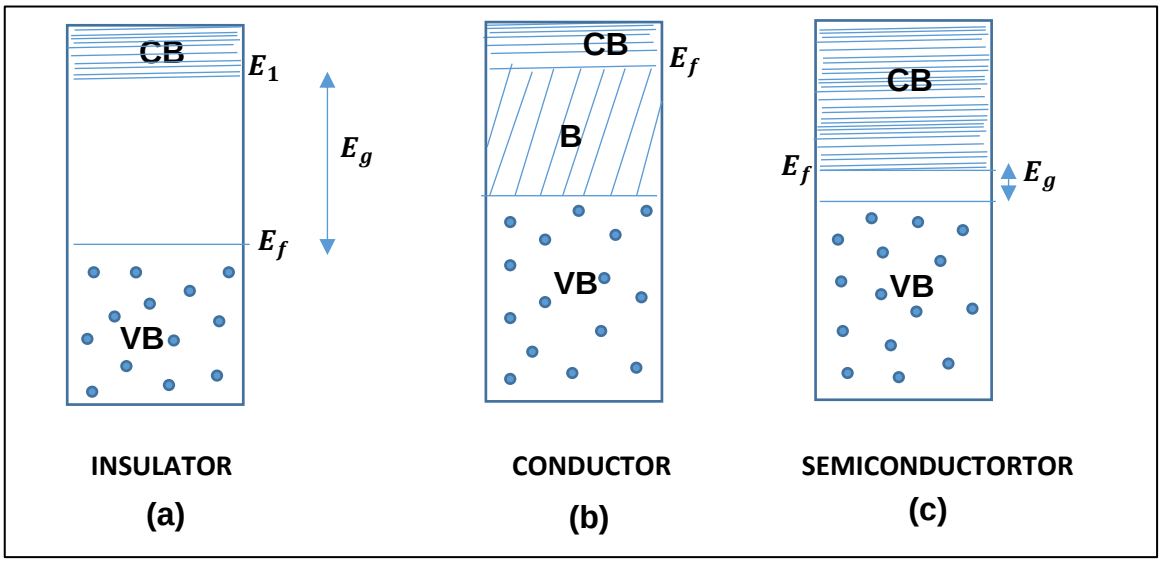


**Figure 2.3** Diagram showing the conduction band (CB), Valence band (VB) and Fermi energy $E_f$ for (a) insulator (b) conductor (c) semiconductor

The semiconductors on the other hand are those materials with small energy gap ($E_g$) between their filled valence band and their conducting band. They have conductivities between those of conductors and insulators. Semiconductors can however be made to conduct by the application of heat or addition of impurities. Examples of semiconductors are silicon, germanium, zinc sulphide (ZnS) and zinc oxide (ZnO) used in this research. Furthermore, semiconductors can be classified as direct or indirect band gap semiconductors.

***Direct and indirect energy band gap semiconductors***.

When light falls on a material such as a semiconductor, it does so in the form of photons of energy $E_p$ and momentum p respectively given by

$$E_p = h\nu \tag{2.5}$$

$$p = \frac{h}{\lambda} \tag{2.6}$$

The direction in which the photon travels is given by the wave vector. The wave number k is defined as

$$k = |\boldsymbol{K}| = \frac{2\pi}{\lambda} \quad \text{(wave number equals the magnitude of the wave vector)}$$

(where **K** the wave vector and λ is the photon wavelength)

Thus, the photon momentum is given by:

$$p = \frac{hk}{2\pi} \quad \text{or } p = \hbar k \quad (\text{where } \hbar = \frac{h}{2\pi}) \qquad (2.7)$$

and the photon momentum is proportional to the wave number k

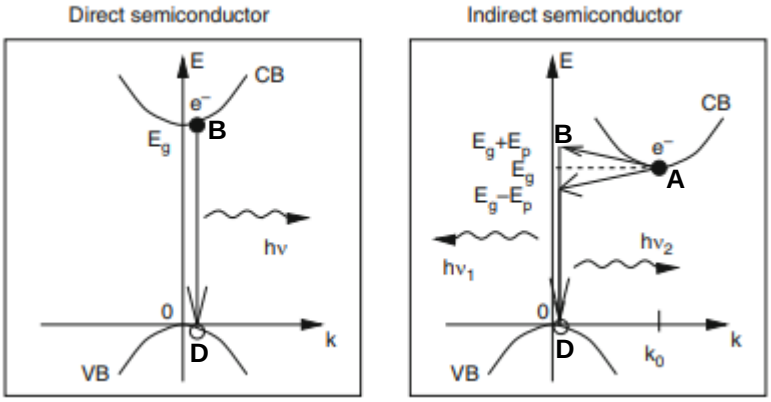


**Figure 2.4** Energy transitions in Direct and indirect band gap material [4]

When a photon of energy $E_p$ is shone on a semiconductor material and gets absorbed, the electrons in the semiconductor material get translated from the valence band (VB) to the conduction band (CB). If for this transition, the wave number at the maximum of the valence band coincides with the wave number at the minimum of the conduction band (Figure 2.4), we refer to that material as a direct band gap semiconductor.

Some examples of direct band gap materials are gallium arsenide (GaAs), gallium antimonide (GaSb) and Gallium nitride (GaN) [5] and they are used for making light emitting diodes (LEDS) and Lasers. Conversely, if this transition occurs, such that the k value at the maximum of the valence band does not coincide with the k value at the minimum of the conduction band, that material is said to be an indirect semiconductor. Some examples include silicon (Si), aluminium antimonide (Al As) and germanium (Ge). For both direct and indirect band gap semiconductors, transitions to and from the conduction band requires that both energy and momentum of the system should be conserved.

After electrons are moved to a higher energy level $E_2$ , they are unstable and need to return to the ground state with lower energy level $E_1$ to be stable, so they give out whatever energy they had received as they recombine with the holes in the valence band. This recombination is radiative and does not need extra momentum because the returning electrons fall back directly and release photons whose energy $E_p = E_2 - E_1$. For indirect band gap materials however, this is not the case because as earlier explained, the k values at the maximum of the valence band is not the same as that at the minimum of the conduction band. Thus, when the translated electrons want to return to their ground state, they have to first move from state A to state B (Figure 2.4) before they can return to the valence band for the recombination process [6]. That deflection from A to B results in the electrons losing energy and momentum in the crystal lattice. The electrons achieve this feat by interacting with a phonon or lattice vibrations, in order to recombine with the holes in the valence band. This recombination process unlike the first type, is non-radiative and phonon driven. Thus, for indirect band gap semiconductors photons as well as phonons are given off. If, however $E_p > E_2 - E_1$, photons may not be absorbed but scattered.

Absorption spectroscopy technique can be used for the determination of the absorption coefficient $\alpha$ of a material. This property shows the light absorbance ability of a material and its reciprocal $\frac{1}{\alpha}$ gives the average distance light can travel in the material before it gets absorbed.

The relationship between absorption coefficient $\alpha$ and light intensity $I$ is given by:

$I(x) = I_0 e^{-\alpha x}$

where $I_0$ is the incoming light intensity, x is the thickness of the sample.

Figure 2.5 shows the light absorbance abilities of direct and indirect band gap materials.

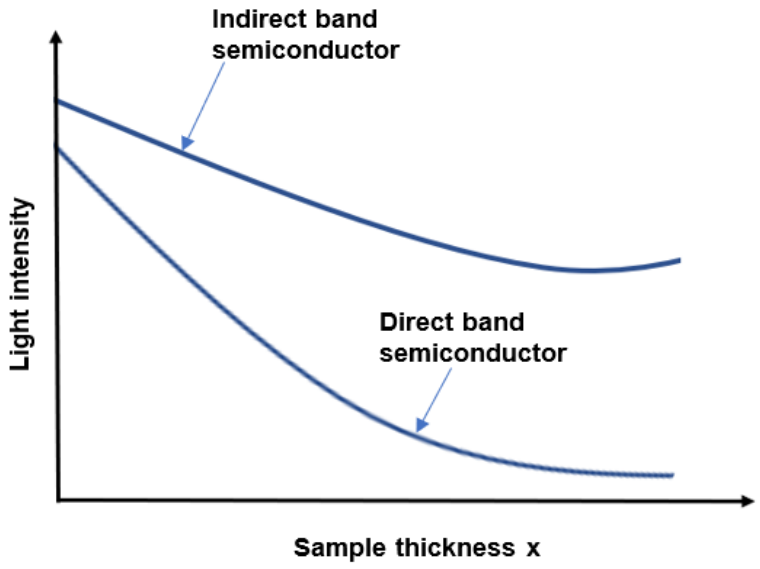


**Figure 2.5** Light absorbance by direct and indirect band gap materials.

From Figure 2.5, it implies that for an indirect band gap semiconductor to absorb light, it needs to be very thick. Indirect band gap semiconductors are used for making photovoltaic and thin film solar cells [7].

The variation of absorption coefficient with energy for direct and indirect band gap materials are also illustrated in Figure 2.6.

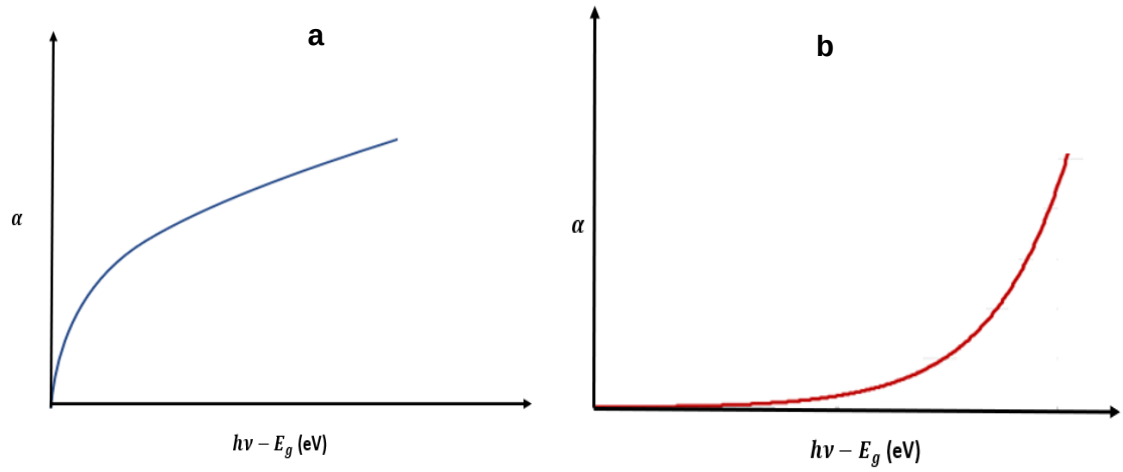


**Figure 2.6** Variation of absorption coefficient with energy for (a) direct band gap and (b) indirect band gap materials.

## 2.3 Electron band structures, absorption and emission spectra

Bohr in his studies of electrons inferred that electrons can behave like standing waves do in a string and that each energy level of an electron corresponds to a mode with each mode having a fixed number of wavelengths with no wavelength values in-between. According to him, wavelengths are like energy levels. Thus, electrons can behave like circular standing waves (Figure 2.7) and have an infinite number of modes with each mode corresponding to a particular wavelength and while the allowed orbits give a constructive interference when $2\pi r = n\lambda$, the forbidden ones give a destructive interference for $2\pi r \neq n\lambda$ (where n is an integer).

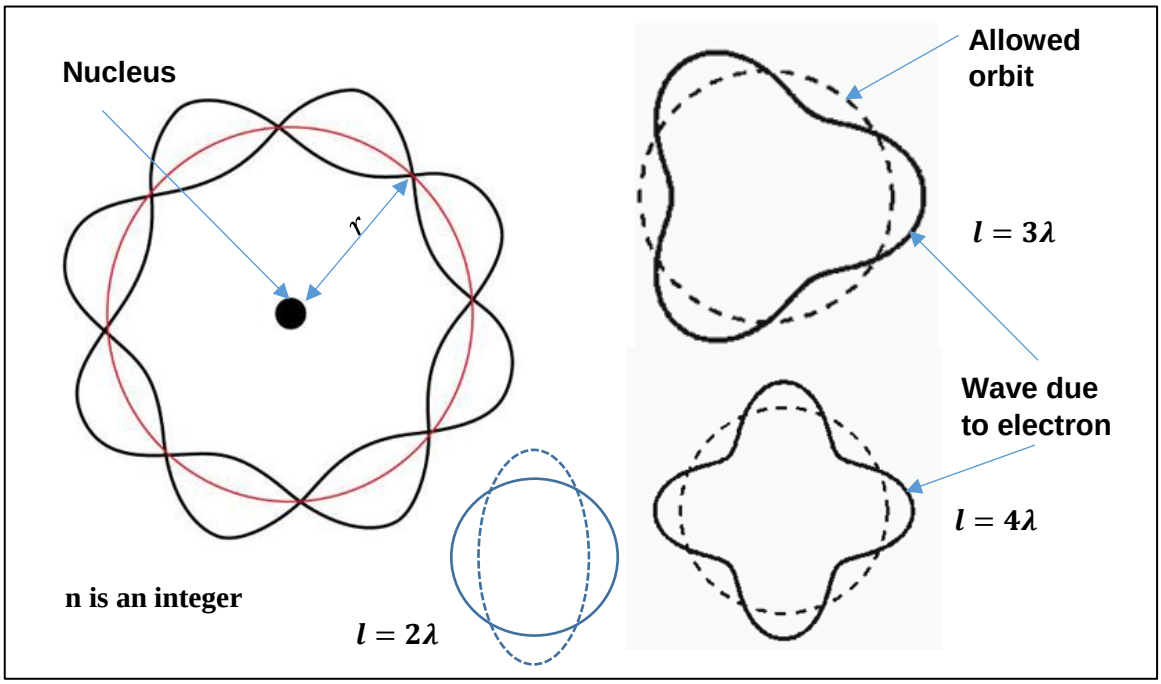


**Figure 2.7** Electrons as circular standing waves with modes which are the wavelengths.

When electrons acquire some energy, they can be excited and can move from L1 to L2 or from L1 to L3 (Figure 2.8) and return along the path shown. The amount of energy they receive from the photons shone on them determines how far they can jump and hence to which levels they transit. Electrons do not absorb all the photons but only accept those (photons) whose energies correspond to their allowed energies. Conversely, electrons give up energies which will take them to discrete levels L1 and L2 for instance. Thus, as illustrated in Figure 2.8, electrons can move from L2 to L1 or from L3 to L2 then finally to L1 and emit photons whose frequencies are a measure of the energy they absorbed while transiting to higher energy levels to give absorption or emission spectra.

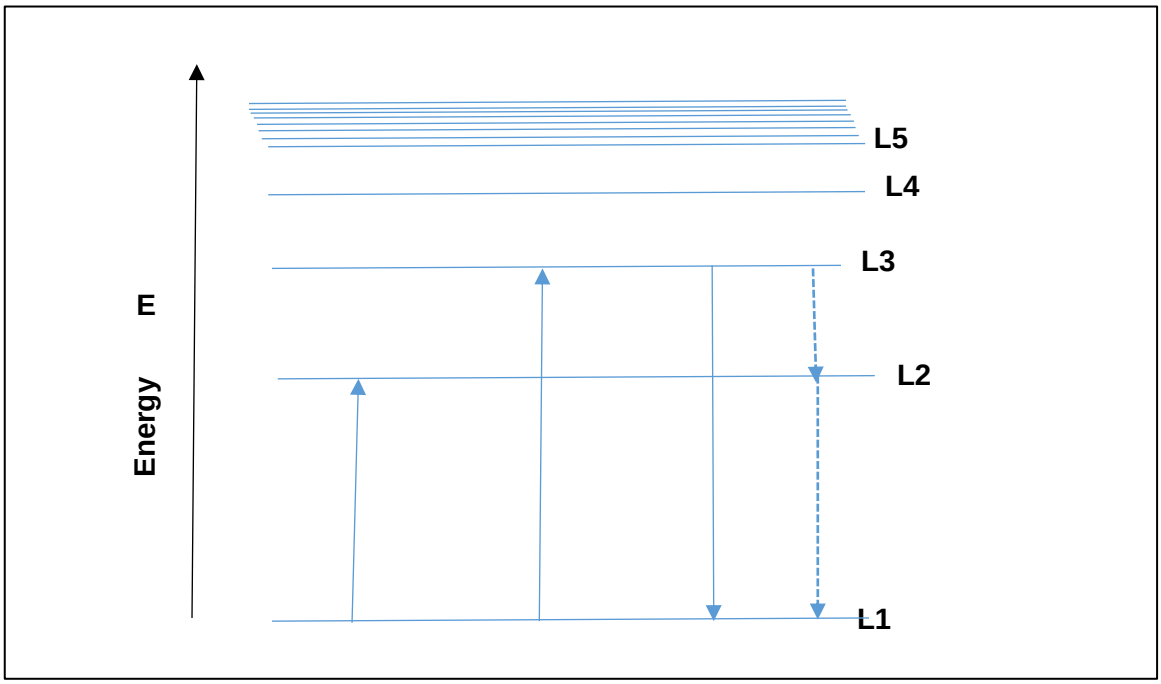


**Figure 2.8** Electron transitions from one level to another (Absorption and Emission)

## 2.4 Electromagnetic waves (EM waves)

In the characterisation of the nanoparticles synthesized for this work, instruments which work with electromagnetic waves (Light) were used and besides that, the particles studied and the materials used in their background are also made to interact with light; hence the need to give some background of EM radiations, and the results of their interaction with different dielectric materials or particles. Light is an electromagnetic wave and has electric and magnetic field components (Figure 2.9) though most times electromagnetic waves are represented by electric fields. Light can be reflected, refracted, transmitted or even polarised. Light gets linearly polarised if its electric and magnetic field components maintain their respective planes with non-rotation of the resultant E-field or it can be circularly polarised if two linearly polarised light waves of same amplitude are superimposed on each other with a rotation of the E-field. Elliptical polarisation occurs when light waves of unequal amplitudes add up with the E-field of the resultant waves rotating elliptically.

A plane wave propagating through a medium has a general form:

$$E(x,t) = E_0 e^{i(kx-wt)} \quad (2.8)$$

Where *x* and k are the position and propagation vectors respectively, and t is the time.

In travelling from one medium to another, EM wave could do so at normal incidence or obliquely.

Considering a wave travelling in the z-direction, there are no $E_y$ and $E_z$ components thus:

$E_x = E_0 \cos(wt - kz)$ and its associated B-field is (2.9)

$$B_y = \frac{E_0}{c}\cos(wt - kz)$$

Both the electric and magnetic fields are in phase though the B-field is $\frac{1}{c}$ weaker.

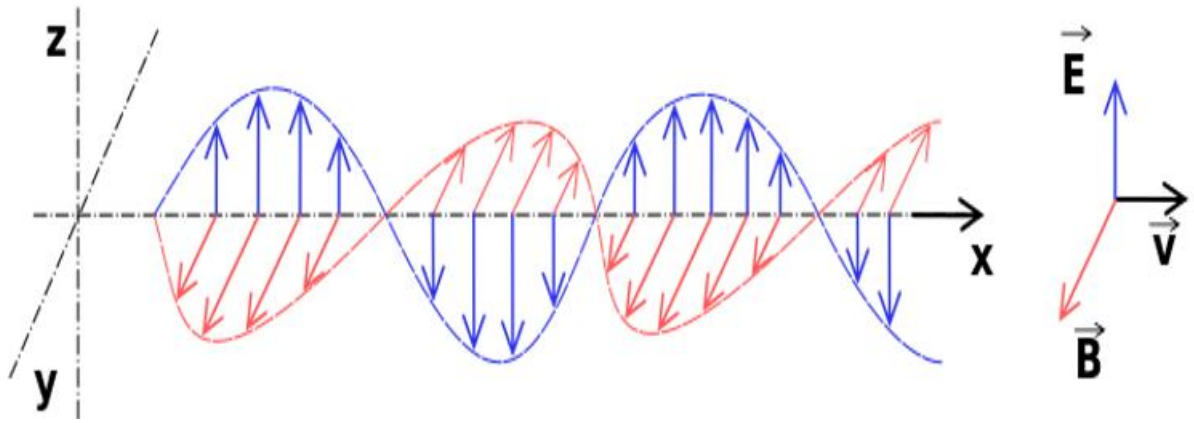


**Figure 2.9** Electromagnetic wave illustrated.

$$\vec{E} = \underline{E_{0x}}\,\mathrm{Cos}(\mathrm{wt} - \mathrm{kz}) + \underline{E_{0y}}\mathrm{Cos}(\mathrm{wt} - \mathrm{kz}) + \delta) \quad (2.10)$$

Where $\delta$ is the phase difference between $E_x$ and $E_y$. Thus when $\delta$=0, and $E_0 x = E_0 y$ we have a linearly polarised light with same amplitudes. When $\delta = \pm\frac{\pi}{2}$ an elliptically

polarised light is produced and for $E_0x = E_0y$ and $\delta = -\frac{\pi}{2}$ we have a circularly polarised light.

### 2.4.1 Maxwell's equations and EM wave propagation through a medium

Maxwell's equations can be used for explaining the propagation of electromagnetic waves through a medium or dielectric material. The first two equations are the Gauss' laws, the third is Faraday's law while the fourth is the Ampere-Maxwell's law. The equations show how a changing electric field can produce a magnetic field and vice versa.

For a wave travelling along the z-direction:

Since $\nabla \times B = \mu_0 J + \mu_0 \varepsilon_0 \frac{\partial E}{\partial t}$ (2.11)

And in a non-conducting medium, $J = 0$, it can be shown that $\frac{\partial^2 E_x}{\partial z^2} = \mu_0 \varepsilon_0 \frac{\partial^2 E_x}{\partial t^2}$

Which when compared with the equation for a wave in a string $\frac{\partial^2 y}{\partial x^2} = \frac{1}{v^2}\frac{\partial^2 y}{\partial t^2}$

gives that $v = \sqrt{\frac{1}{\mu_0 \varepsilon_0}}$ which is approximately $c_0 = 2.99 \times 10^8 ms^{-1}$ , the speed of light in a vacuum. (In a vacuum, $\mu_0 = 4\pi \times 10^{-7} Hm^{-1}$ and $\varepsilon_0 = 8.854 \times 10^{-12} s^2 H^{-1} m^{-1}$) Thus the speed of light in a vacuum $c_0 = \sqrt{\frac{1}{\mu_0 \varepsilon_0}}$ and $\frac{c_0}{c} = \sqrt{\varepsilon_r \mu_r}$. This shows that the ability of light to travel through a material depends on the permittivity and permeability values for that medium.

Conversely, in a conducting medium, $J = \sigma E$ and $\frac{\partial B_y}{\partial z} = -\mu(J + \varepsilon \frac{\partial E}{\partial t})$ hence

$\frac{\partial^2 E_x}{\partial z^2} = \mu\sigma \frac{\partial E_x}{\partial t} + \mu\varepsilon \frac{\partial^2 E_x}{\partial t^2}$ (2.12)

By assuming a solution of the form $E = E_0 e^{i(kz-\omega t)}$ and substituting into (2.12) it can be shown that the propagation vector k is given by:

$$\mathrm{k} = \sqrt{\mu\varepsilon\omega^2 + i\omega\mu\sigma} \qquad (2.13)$$

This propagation vector has a real part (*Re*) as well as an imaginary part(*im*). The imaginary part is the reason for the damping of electromagnetic waves as it travels through a medium.

$$\text{Hence } Re(\mathrm{k}) = im[\mathrm{k}] = \sqrt{\frac{\sigma\mu\omega}{2}} \text{ and } \frac{1}{im[\mathrm{k}]} = d = \sqrt{\frac{2}{\sigma\mu\omega}} \qquad (2.14)$$

$d$ called the skin depth is a decay constant for the damping of EM radiation as it makes its way through a material or medium. Thus, a material with a low skin depth may not be able to transmit EM waves at a high frequency. For metals or conductors, two quantities namely conductivity $\sigma$ and displacement current $\epsilon\omega$ are of importance and for good conductors like silver and gold which feature in this work, $\sigma >> \epsilon\omega$. Silver and gold have conductivities of $6.30 \times 10^7 S/m$ and $4.1 \times 10^7 S/m$ respectively at 20 ℃ and white light with a wavelength of 500 nm has a skin depth of roughly 3 nm.

## 2.5 Optical properties of materials

### Introduction

Bulk metals are ductile, have high thermal and electrical conductivities, delocalised electrons, a continuous energy band, high density of states and do undergo plasmon excitation. Nanoparticles on the other hand due to their reduced sizes, have large surface area to volume ratios, high surface energies, low density of states, plasmon excitation and can have quantum confinement (as in the case of ZnO nanoparticles). Nanoparticles can be unstable and may not have well defined structures due to aggregation or because they can continue growing until stopped using ligands, inorganic capping materials or soluble polymers. Metal nanoparticles have sizes which are small compared with the wavelength of visible light. They interact with light and can absorb or scatter it.

Metal oxides in their bulk form have a wide bandgap and less ability to react [8] but when their sizes are reduced, they become more reactive and their ability to conduct can be deduced from their reflectivity and absorbance abilities. Metal oxide nanoparticles have reflectivity which depends on their sizes and so also does their light absorbance which is discrete due to quantum - size confinement. They (metal oxide nanoparticles) show linear and non-linear optical properties because of transitions between electronic levels and their (metal oxide nanoparticles) linear optical properties are also dependent on their sizes.

The Bohr radius of a bulk exciton is given by:

$$R_B = 4\pi\varepsilon_0 \frac{\varepsilon\hbar^2}{\mu e^2}$$

Where $\mu$ is the reduced mass of the exciton and $\varepsilon$ is the semiconductor dielectric constant.

Thus, quantum confinement can either be weak, strong or intermediate depending on the nanoparticle size r with respect to $R_B$. Thus if $r >> R_B$, the quantum confinement will be weak but if the reverse is the case, the quantum confinement will be strong. For $r \approx R_B$ the quantum confinement will be intermediate [9].

### 2.5.1 Reflection of plane EM waves at normal and oblique incidence

When plane EM waves are shone on a material, they travel from one medium to another and its velocity and wavelength can change depending on the refractive index of light for the material. Light incident either at normal incidence (a) or obliquely (b) can get reflected or transmitted as shown in Figure 2.10 and the electric and magnetic fields as functions of time for the incident, reflected and transmitted waves are also as shown in that diagram.

(where $E_0$ is the amplitude of the E-field and $\hat{\jmath}$ , $\hat{k}$ are the unit vectors)

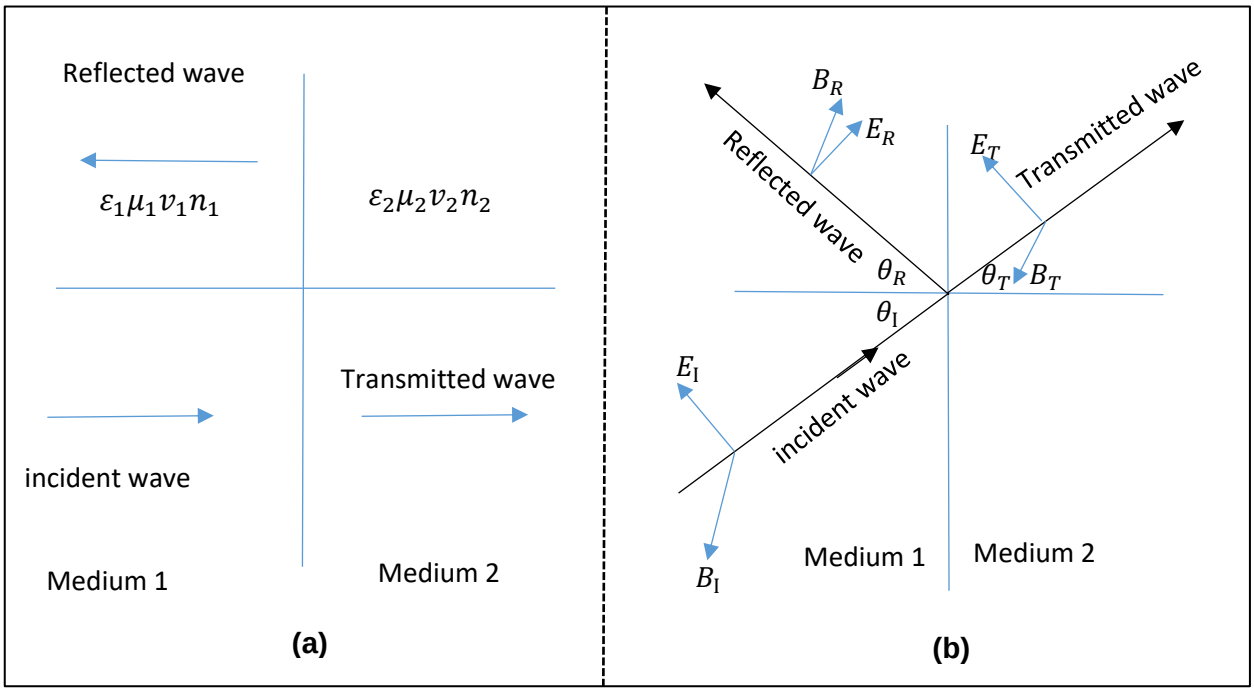


**Figure 2.10** Plane waves (a) at normal or (b) oblique incidence on a surface.

For plane waves at normal incidence [10]:

For the E –field,

$\overrightarrow{E}total = \overrightarrow{E_I} + \overrightarrow{E_R}$ when $x < 0$ and $\overrightarrow{E}total = E_T$ when $x > 0$ and

For the B- field,

$\overrightarrow{B}total = \overrightarrow{B_I} + \overrightarrow{B_R}$ when $x < 0$ and $\overrightarrow{B}total = B_T$ when $x > 0$ and

Furthermore, at right angles to the incident plane, there are no E or B field components. Thus $E_1 = E_2$ and similarly, $\frac{1}{\mu_1}B_1 = \frac{1}{\mu_2}B_2$ .

Hence for the time dependent E terms

$$E_{0I}e^{i(-\omega_I t)} + E_{0R}e^{i(-\omega_R t)} = E_{0T}e^{i(-\omega_R t)} \qquad (2.15)$$

$\omega_I = \omega_R = \omega_T = \omega$ .

Similarly, the wave propagation vectors $k_I = k_R = k_1$, while $k_T = k_2$.

For the B –fields also:

$$\frac{1}{\mu_1 v_1}\left\{E_{0I}e^{-i\omega t} - E_{0R}e^{-i\omega t}\right\} = \frac{1}{\mu_2 v_2}E_{0T}e^{-iwt}$$

which yields :

$$E_{0I} - E_{0R} = \frac{\mu_1 v_1}{\mu_2 v_2}E_{0T} = \beta E_{0T} \qquad (2.16)$$

(where $\beta = \frac{\mu_1 v_1}{\mu_2 v_2}$ )

Hence, $E_{0R} = \frac{1-\beta}{1+\beta}E_{0_I}$ and $E_{0T} = \frac{2}{1+\beta}E_{0I}$

Thus for $\beta < 1$ ,the phase difference between the incident and the reflected ray will be the same ($\delta_I = \delta_R$ ) , but if $\beta > 1$ the phase difference between the incident ray and the reflected ray will be 180°, such that $(\delta_I + 180°) = \delta_R$

In terms of velocities, $E_{0_R} = \left|\frac{v_2 - v_1}{v_2 + v_1}\right| E_{0_I}$

If $v_1 > v_2$, $E_{0_R} = E_{0I}$ and $(\delta_I + 180°) = \delta_R$.

Conversely if $v_1 < v_2$ , $\delta_I = \delta_R$

In terms of refractive indices of the two media [11],

$$E_{0R} = \left|\frac{n_1 - n_2}{n_1 + n_2}\right| E_{0_I} \qquad (2.17)$$

If $n_1 > n_2$ (e.g. from glass to air), $E_R \; and \; E_I$ will be in phase

If $n_1 < n_2$ (e.g. from air to glass), $E_R \; and \; E_I$ will be out of phase by180 ° and

$$E_{0T} = \left|\frac{2n_1}{n_1 + n_2}\right| E_{0_I} \qquad (2.18)$$

From Equation 2.17, the coefficient of reflection R is given by:

$$R = \frac{E_{0R}}{E_{0_I}} = \frac{n_1 - n_2}{n_1 + n_2} \tag{2.19}$$

Similarly, from Equation 2.18, the coefficient of transmission T is given by:

$$T = \frac{E_{0T}}{E_{0_I}} = \frac{2n_1}{n_1 + n_2} \tag{2.20}$$

And it can be shown that $R + T = 1$

For the oblique incidence of light, with defined E and B fields and by the same reasoning as in the normal incidence case.

The incident, reflected and transmitted wave vectors at the plane of incidence are related as shown below:

$$k_1 \, Sin\theta_R = k_2 \, Sin\theta_T = k_1 \, Sin\theta_I \tag{2.21}$$

Because the angle of incidence equals the angle of reflection,

$\theta_R = \theta_I$, and $Sin\theta_R = Sin\theta_I$.

It can be shown from (2.21) that:

$\frac{Sin\theta_T}{Sin\theta_I} = \frac{k_1}{k_2} = \frac{n_1}{n_2}$ (Snell's law)

$$E_{0_I} + E_{0_R} = \frac{Cos\,\theta_T}{Cos\,\theta_I}\,\vec{E}_{0_T} = \alpha\vec{E}_{0_T} \tag{2.21a}$$

Where $\alpha = \frac{\sqrt{1-\left(\frac{n_1}{n_2}Sin\,\theta_I\right)^2}}{Cos\theta_I}$ (2.22)

$$E_{0_T} - E_{0_R} = \frac{\mu_1 v_1}{\mu_2 v_2}\left[E_{0_T}\right] = \beta E_{0_T}$$

$$E_{0_I} - \beta E_{0_T} = \alpha E_{0_T} - E_{0_I} \quad (2.23)$$

Thus, the Transmission coefficient $T = \frac{E_{0_T}}{E_{0_I}} = \frac{2}{\alpha+\beta}$ (2.24)

$$E_{0_R} = E_{0_I} - \beta\left[\frac{2}{\alpha+\beta}\right]E_{0_I} \quad (2.25)$$

Thus the Reflection coefficient $R = \frac{E_{0_R}}{E_{0_I}} = \left[1 - \frac{2\beta}{\alpha+\beta}\right] = \frac{\alpha-\beta}{\alpha+\beta}$ (2.26)

As before, it can be shown that $R + T = 1$

### 2.5.2 Dielectrics and polarisation

Dielectric materials are insulators which can store charges. When an electric field is applied to a dielectric material, the positive and negative charges in it can be moved to opposite sides of the material (polarisation). While the positive charges get moved in the direction of the applied field, the negative charges are moved in the opposite direction. Some examples of dielectrics include water (used in the preparation of the chemical solutions and the leaf extracts used in this work), sodium chloride (NaCl) and Diamond

Properties of dielectrics include polarisation, dispersion, piezoelectricity and absorption of electromagnetic radiation. A dielectric like water is a polar dielectric with a permanent dipole moment. Another like sodium chloride has a dipole moment and shows ionic polarisation. Diamond on the other hand is a covalent solid and shows electronic polarisation. Electric polarisation in water is electronic, ionic and orientational (due to the arrangement of its molecules). While the electronic contribution occurs in the ultraviolet (UV) range, the ionic and orientational polarisation takes place in the infrared (IR) and microwave ranges.

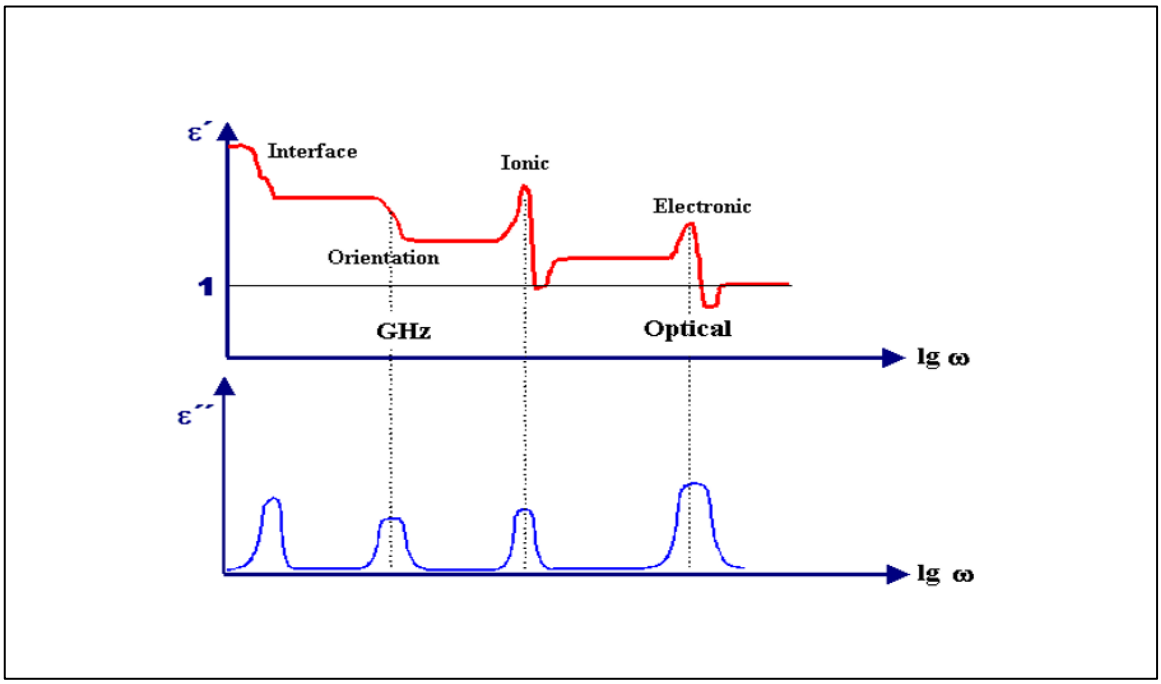


**Figure 2.11** Illustration of dielectric constant as frequency dependent

Dielectric constants of materials ($\epsilon$) just like refractive indices ($n$), are frequency dependent. Hence the dielectric constant is a function of $\omega$ written as $\epsilon(\omega)$ just like $n(\omega)$ and $\epsilon\ \alpha\ n^2$. The value of $n$ for a material determines what the phase velocity of the EM waves through a given dielectric medium will be and therefore gives the extent of the dispersion of the EM waves when it is passed through that dielectric material. Polarization (P) on the other hand in dielectrics is also frequency dependent is given by:

$$\mathrm{P}(\omega) = \epsilon(\omega)\chi_e(\omega)E(\omega) \tag{2.27}$$

Where $\chi_e$ is the susceptibility of a dielectric material and shows the ease with which a material can be polarised.

$\chi_e = \varepsilon_r - 1$ (where $\varepsilon_r$ is the relative permeability of the material).

In gases, $\chi_e = \varepsilon_r - 1 = N\alpha$ (where N is the number of the atomic or molecular dipoles per $m^3$ and $\alpha$ is the polarizability and in a vacuum, $\chi_e = 0$.

In a static electric field and for spherical atoms, polarizability is proportional to the atomic volume thus $\alpha = \frac{4}{3}\pi a^3$ (a is the radius of the atom), but in a dynamic medium, the equation of motion for a bound electron (2.28) is used. Thus:

$$m\frac{d^2X}{dt^2} + b\frac{dX}{dt} + {\omega_0}^2 X = -eE\exp(i\omega t) \tag{2.28}$$

where $\omega_0 = \frac{k}{m}$ and $k$ is the force constant and $m$ is the mass of an atom.

By using a solution of the form $X = X_0 e^{i\omega t}$ and substitution into (2.28) we have :

$$X_0 = \frac{-\frac{eE_0}{m}}{{\omega_0}^2 - \omega^2 + \frac{ib\omega}{m}} = \frac{i^2\frac{eE_0}{m}}{{\omega_0}^2 - \omega^2 + \frac{ib\omega}{m}} \tag{2.29}$$

The complex part of this expression ($\frac{ib\omega}{m}$) represents the wave damping per unit mass.

Furthermore, the induced dipole moment p is given by:

$p = -eX_0$ and the total polarisation $P = \frac{\frac{Ne^2}{m}E_0}{{\omega_0}^2 - \omega^2 + \frac{ib\omega}{m}} = (\epsilon - 1)\epsilon_0 E$ (2.30)

Thus, the dielectric constant also has a real part associated with wave dispersion and an imaginary part associated with wave absorption. The nanoparticles studied in this work were suspended in solutions prepared with water. Water as earlier on stated in this write up is a polar dielectric which on the application of an electric field has a temperature dependent equilibrium polarisation $P_{eq}$ given by [12]:

$$P_{eq} = i\omega P\tau + P \tag{2.31}$$

This equilibrium polarisation also depends on time t thus:

Thus $P(t) = \frac{P_{eq}(1 - i\omega\tau)}{1 + \omega^2\tau^2}$ (2.32)

Therefore, as before, the polarisation has a real part related to dispersion and an imaginary part related with absorption. (Figure 2.11).

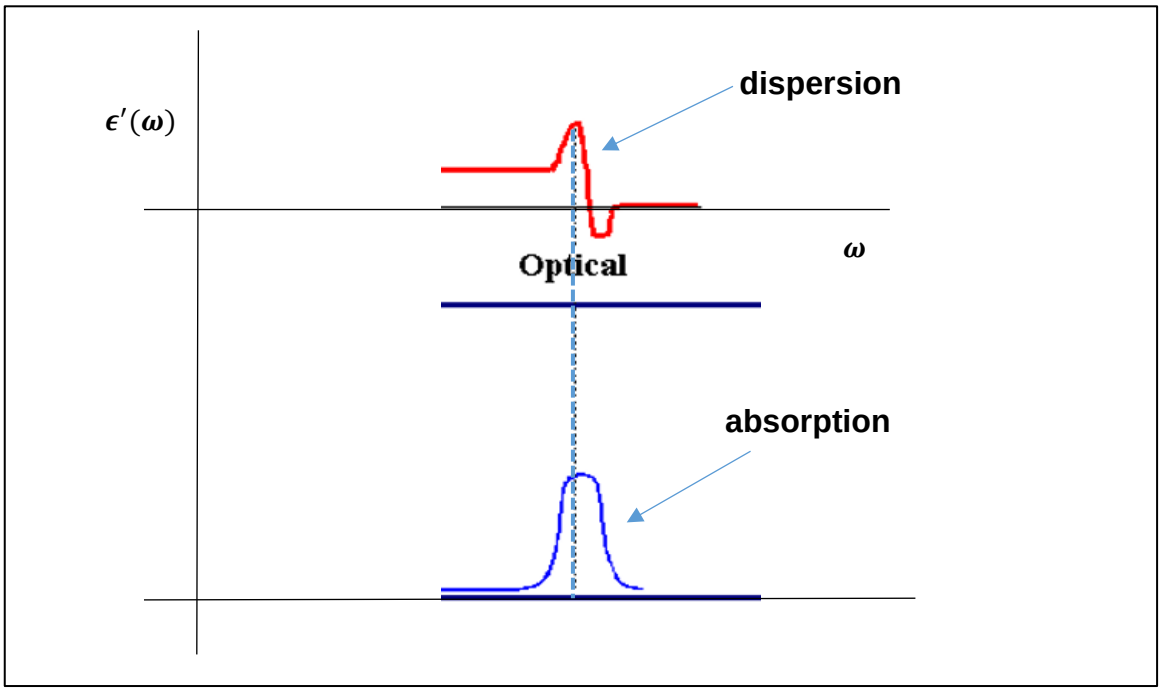


**Figure 2.11 a** Illustrating real and imaginary part of the dielectric constant.

In bulk metals, there are two contributions to the dielectric function: those due to the bound electrons and those due to the free electrons. For the free electrons' contribution, the plasma angular frequency $\omega_p$ is given by [13].

$$\omega_p = \sqrt{\frac{4\pi Ne^2}{m}} \tag{2.33}$$

where N is the free electron density of the metal and m is the effective mass of the free electrons, e is the electronic charge $9.11 \times 10^{-31} kg$), and $\varepsilon$ is the dielectric constant of surrounding medium.

Equation 2.33 shows that for bulk metals, plasma frequency $\omega_p$ does not depend on particle size but depends on the free electron density N.

For metallic nanoparticles, their dielectric function as a function of the incident angular frequency has a real part as well as a complex part [13,14] thus:

$$\varepsilon = \varepsilon_r + i\varepsilon_i = 1 - \frac{\omega_p}{\omega^2 + i\,\gamma_0\omega} \tag{2.34}$$

While the real part is given by:

$$\varepsilon_r = 1 - \frac{{\omega_p}^2}{\omega^2 + {\gamma_0}^2} \tag{2.35}$$

The imaginary part is given by:

$$\varepsilon_m = 1 - \frac{{\omega_p}^2\gamma}{\omega(\omega^2 + {\gamma_0}^2)} \tag{2.36}$$

where $\omega_p$ is the plasma frequency, $\gamma_0$ is the damping constant , $\varepsilon_m$ is the imaginary part of the dielectric constant and $\varepsilon_r$ is the real part of the dielectric constant.

At high frequencies, $\gamma_0 = 0$, thus $\varepsilon_r = 1 - \frac{{\omega_p}^2}{\omega^2}$ and $\varepsilon_m = \frac{{\omega_p}^2\gamma}{\omega^3}$

### 2.5.3 Plasmons and plasmonic resonance

**Introduction**

Materials are composed of atoms and atoms have positive cores which are surrounded by negative electrons. When light (EM waves) is shone on the atoms with its surrounding electrons, the opposite charges are separated from one another and an electric dipole is created. The electrostatic interaction between the negative electrons with the protons acts as a restoring force and produces electronic oscillations. The collective oscillation of the free electron gas in a metal on interaction with electromagnetic radiations, produce plasmons. Plasmons depend on the nature of the dielectric medium surrounding the nanoparticles [15].

Plasmons occur on the surface of bulk metals as well as on nanoparticle surfaces. Plasmons in bulk materials can have continuous wavelengths (Figure 2.15) whereas in nanoparticles, surface plasmons are restricted to a small volume and this affects the

range of wavelengths nanoparticle plasmons can have. Surface Plasmon resonance (SPR) of nanoparticles give an indication of their aspect ratio. While small nanoparticles have large surface areas and high surface energy, the reverse is true of large nanoparticles [16].

Surface plasmons in nanoparticles have discrete wavelengths and give a distinct peak (Figure 2.15). This also explains why the colours of metal nanoparticles differ depending on their sizes or shapes. The energy of surface plasmons is also dependant of the number density of electrons N as well as the dielectric constant of the surrounding medium.

Thus

$$E_{plasmon} = \hbar\sqrt{\frac{Ne^2}{m_e\varepsilon}} \tag{2.37}$$

where ħ is plank constant.

***Plasmonic resonances***

Electrons are charged particles and can vibrate and produce an electric field which interact with incoming EM waves, causing a distortion in the electron cloud to produce surface plasmon. If the electron cloud (Figure 2.12) gets excited in resonance with the incoming EM waves, there will be a strong light absorbance at a particular wavelength and surface plasmon resonance (SPR) occurs. Light absorbance due to surface plasmon resonance depends on the size or geometry (such as cylinder, triangle, sphere etc) of nanoparticles. For silver, plasmon frequency is not easily calculated by considering its electronic structure because of the activities of its d –orbital electrons. Thus, its plasmon frequency is estimated using its dielectric constant. For silver or gold, plasmon oscillations occur close to the visible light range of wavelengths. Thus if gold nanoparticles are irradiated with visible light, green colour will be absorbed, and the gold nanoparticles will appear wine - coloured or red. Silver nanoparticles on the other hand give a plasmon resonance peak[17] at a wavelength of about 400 nm and the blue colour of the visible light gets absorbed making the nanoparticles take on a yellow or

yellowish-grey colour. By the same reasoning, Platinum or palladium nanoparticles look black. [14]. Surface plasmon resonance also differs depending on the type of liquid or dielectric material surrounding the nanoparticles [18] or the size of the nanoparticles [19]. If the nanoparticles are surrounded with a dielectric material with a high dielectric constant, the plasmon resonance frequency will be low (redshifted) but if surrounded with a low dielectric constant material, the plasmon resonance frequency will be high (blue shifted).

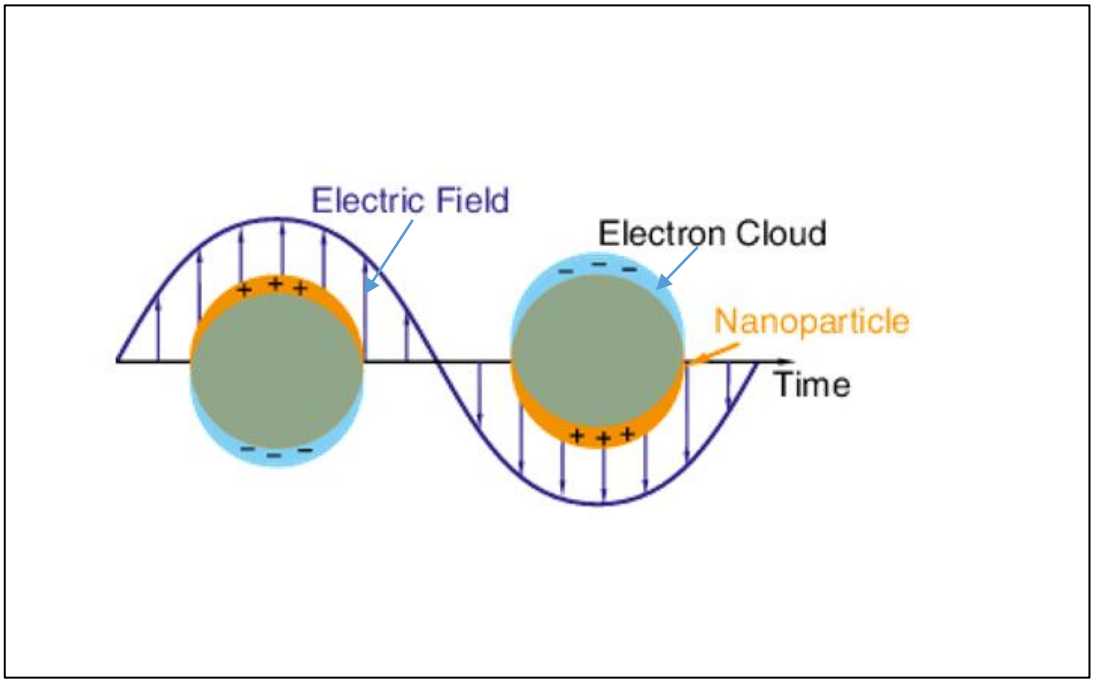


**Figure 2.12** Local surface plasmon resonance phenomenon illustrated.

The plasmon resonance frequency for bulk materials [20] $\omega_p$ depends on electron density, effective electron mass, [21] and is given by equation 2.33. A high electron density produces a high plasmon resonance frequency (blueshift) while a low electron density will give a low plasmon resonance frequency.

For nanoparticles, the plasmon frequency $\omega_s$ is lower being given by:

$$\omega_s = \frac{\omega_p}{\sqrt{2}} = \sqrt{\frac{4\pi N e^2}{2m_e \varepsilon}} \quad (2.38)$$

Equation (2.38) shows that the plasmon frequency for nanoparticles, increases with a high number density of electrons or concentration of nanoparticles in a given solution as well as the nature of the surrounding dielectric medium. That explains why solutions of different concentration of the same nanoparticles have varied colours. For instance, silver nanoparticles can be reddish brown as the one synthesized in this work but those made with other leaf extracts can be yellow, red, pink etc. Equation 2.38 also shows that a high dielectric constant will result in a lower plasmon resonance frequency.

This research dealt with nearly spherical nanoparticles and the equations which govern the behaviour of the nanoparticle in a dielectric medium was discussed. The properties considered were the extinction, absorption and scattering efficiencies. The type of polarizability for small and large nanoparticles was also treated.

Considering metal nanoparticles as dipoles and assuming the nanoparticles have a dielectric constant $\epsilon_1$: If they are situated in a medium whose dielectric constant is $\epsilon_0$ and EM waves of amplitude $E_0$ is shone on them (metal nanoparticles), the electric field around the nanoparticles is a solution of Laplace's equation $\nabla^2\varphi = 0$. The relationship between the electric potential $\varphi$ the nanoparticles experience and the electric field strength around it E is given by $E = -\nabla\varphi$.

If the normal component of the electric displacement D [21] as well as the electric potential at the nanoparticle surface are assumed to be continuous, the Laplace's equation will have angular as well as radial solutions: $r^l$ and $r^{-l+1}$ (where $l$(the angular momentum) 0,1.2…)

For the case $l = 1$ for the electric field in the x-direction and by applying the boundary conditions that:

Within the sphere, $r < a$, $\varphi = ArSin\,\theta Cos\phi$ ( 2.39)

Outside the sphere, $r > a$ $\varphi = -(E_0 r + \frac{B}{r^2})Sin\,\theta Cos\phi$ (2.40)

Where A and B are constants.

Thus for $r > a$ $\quad E = E_0\hat{x} - \alpha E_0\left[\frac{\hat{x}}{r^3} - \frac{3x}{r^5}(x\hat{x} + y\hat{y} + z\hat{z})\right]$ (2.41)

Where $\alpha$ is the spherical polarizability [22] and is given by:

$$\alpha = \left(\frac{\epsilon_1 - \epsilon_0}{\epsilon_1 + 2\epsilon_0}\right)a^3 \quad (2.42)$$

a is the diameter of the spherical nanoparticle, $\hat{x}, \hat{y}, and\ \hat{z}$ are unit vectors and $\alpha E_0$ is the induced dipole moment due to the polarization of the conduction electron density. Equation (2.41) is true for a radiating dipole and includes contributions to extinction and Rayleigh scattering by the spherical nanoparticles. Thus, the extinction efficiency $Q_{ext}$ [22] is given by:

$$Q_{ext} = 4x\ \mathrm{I}_m\left(\frac{\epsilon_1 - \epsilon_0}{\epsilon_1 + 2\epsilon_0}\right) \quad (2.43)$$

and the scattering efficiency $Q_{scatter}$ is also given by [18]

$$Q_{scatter} = \frac{8}{3}x^4\left|\frac{\epsilon_1 - \epsilon_0}{\epsilon_1 + 2\epsilon_0}\right|^2 \quad (2.44)$$

And $x = \frac{2\pi a\sqrt{\epsilon_0}}{\lambda}$

Larger particles display Quadrupole plasmon resonance and this occurs for $l = 2$ . Their quadrupole polarizability $\beta$ is given by:

$$\beta = \left(\frac{\epsilon_1 - \epsilon_0}{\epsilon_1 + \frac{3}{2}\epsilon_0}\right)a^5 \quad (2.45)$$

The quadrupole extinction efficiency is given by [22] :

$$Q_{ext.} = 4x\mathrm{I}_m\left[\frac{\epsilon_1-\epsilon_0}{\epsilon_1+\frac{3}{2}\epsilon_0}+\frac{x^2}{12}\left(\frac{\epsilon_1-\epsilon_0}{\epsilon_1+\frac{3}{2}\epsilon_0}\right)+\frac{x^2}{30}\,(\epsilon_1-1)\right] \tag{2.46}$$

While the Rayleigh scattering efficiency is [18]:

$$Q_{scatter} = \frac{8}{3}x^4\left[\left|\frac{\epsilon_1-\epsilon_0}{\epsilon_1+\frac{3}{2}\epsilon_0}\right|^2+\frac{x^4}{240}\left|\frac{\epsilon_1-\epsilon_0}{\epsilon_1+\frac{3}{2}\epsilon_0}\right|^2+\frac{x^4}{900}\,|\epsilon_1-1|^2\right] \tag{2.47}$$

Localised SPR occurs when the polarizability is a maximum and for metal nanoparticles this can only be true if $\epsilon_1$ is negative. Thus, for the dipole polarizability this occurs when $\epsilon_1 = -2\epsilon_0$ or $\frac{\epsilon_1}{\epsilon_0} = -2$. Similarly, for the quadrupole polarizability the LSPR condition will be that

$$\epsilon_1 = -\frac{3}{2}\epsilon_0 \quad \text{or} \quad \frac{\epsilon_1}{\epsilon_0} = -\frac{3}{2}.$$

The LSPR maxima for metallic nanoparticles depend on the nature of its surrounding media and hence dielectric material. Whatever surrounds the nanoparticles while in solution can get adsorbed on its (nanoparticle) surface and alter the nanoparticles surface charge distribution thereby changing its optical properties. When that happens, the nanoparticles substrate field is no longer homogenous and this invariably influences the dielectric function and electrostatic interaction, producing surface plasmon resonance, at a lower frequency [22,23].

It has also been reported that for spherical nanoparticles, plasmon wavelength $\lambda_p$ is directly proportional to the refractive index of the medium surrounding the nanoparticles [22]. Thus:

$$\lambda_p = \sqrt{3}\,\lambda_{p.b}\left\{1+\frac{1}{3}(n_0-1)\right\}$$

Where $n_0$ is the refractive index of the medium in which the nanoparticle is situated, and $\lambda_{p.b}$ is the bulk plasmon wavelength.

Surface plasmons of nanoparticles have lower energy than bulk plasmons. In nanoparticles, we have surface plasmons and quantum confinement effects. For semiconductor nanoparticles like the zinc oxide (ZnO) nanoparticles, size reduction makes the quantum dot optical emission to shift towards higher energies and so light emission is towards lower wavelengths (blue shifted). This is because reducing the size of metals or semiconductors into nanoparticles makes the Nano material have discrete energy levels and a higher bandgap energy ($E_g$), when compared to its bulk counterpart (Figure 2.13).

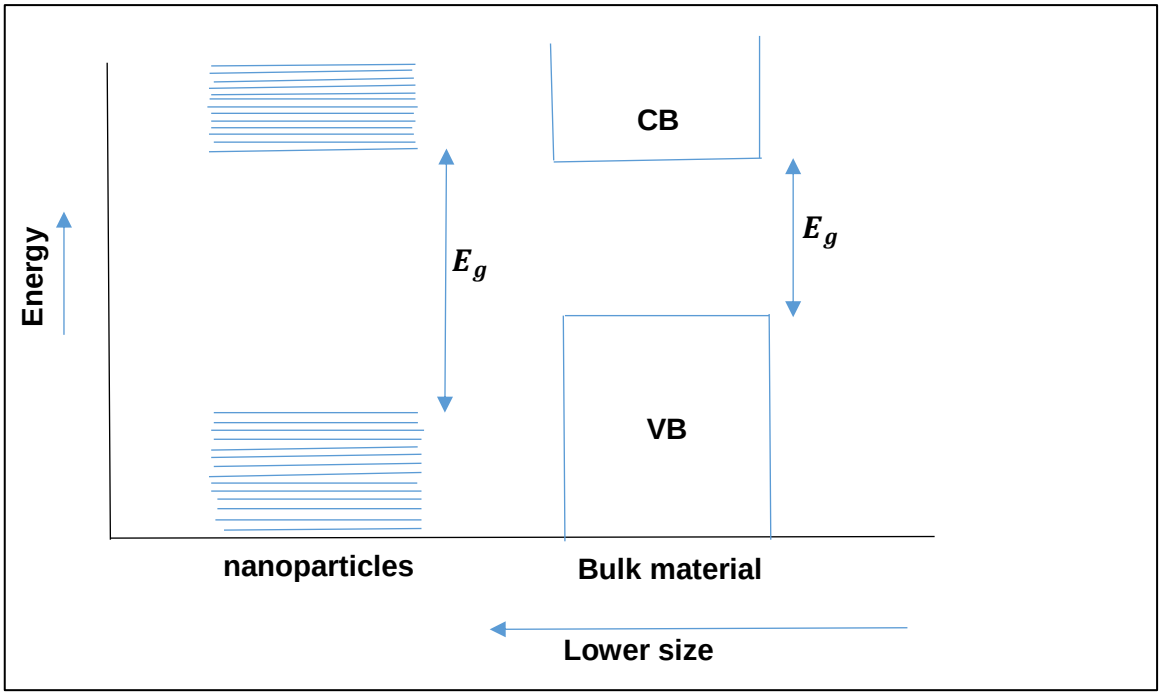


**Figure 2.13** Diagram showing the discrete energy levels in nanoparticles different from the bulk form

Semiconductor nanoparticles have quantised band levels and a higher bandgap energy The effective band gap energy $E_{g_{eff}}(R)$ of a particle of radius r is given by [24]:

$$E_{g_{eff}}(R) = E_g(\infty) + \frac{\hbar^2\pi^2}{2R^2}\left(\frac{1}{m_e^*} + \frac{1}{m_h^*}\right) - \frac{1.8e^2}{\varepsilon R} \tag{2.48}$$

Where $E_g$ is the bulk band gap, $\varepsilon$ is the dielectric constant of its bulk material, $m_e{}^*$ and $m_h{}^*$ are the effective mass of electron and hole respectively, and the last term of this equation represents the coulomb's attraction.

From equation 2.48, $E_{g_{eff}} \propto \frac{\hbar^2\pi^2}{2R^2}$ which means that reducing the size (R) of the particles will result in a higher $E_{g_{eff}}$. Also $E_{g_{eff}} \propto -\frac{1.8e^2}{\varepsilon R}$ which also shows that reducing R will decrease $E_{g_{eff}}$. The effect of these two will produce a higher energy band gap.

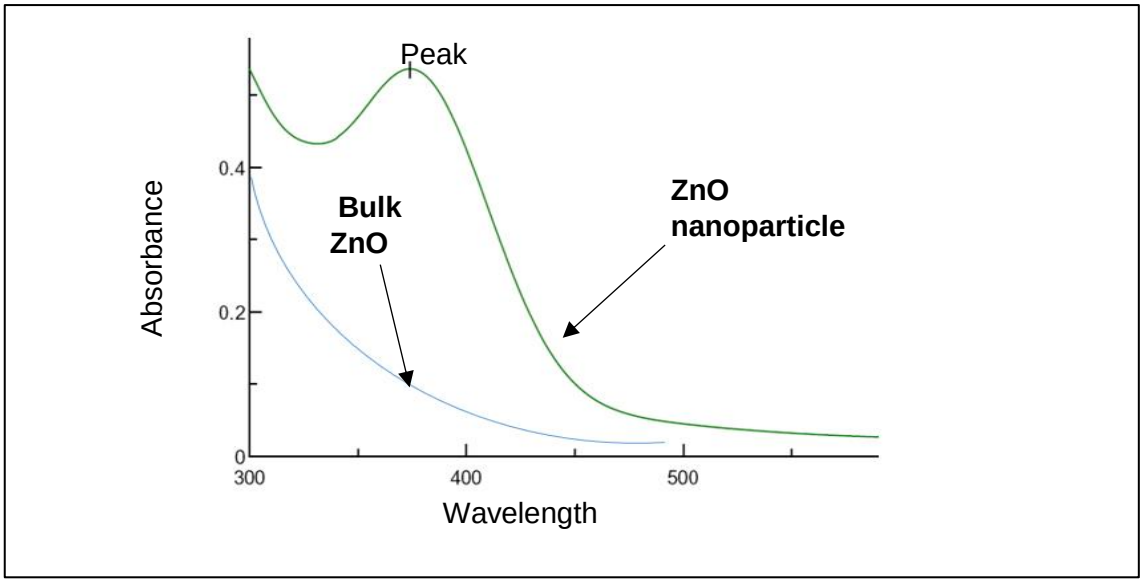


**Figure 2.14** A graph showing absorbance spectrum for bulk zinc oxide and zinc oxide nanoparticle

This graph shows that for the bulk semiconductor the absorbance increases over a range of wavelengths and there is no peak but for semiconductor nanoparticles there is a peak absorbance at a particular wavelength due to SPR.

### 2.5.4 Photoluminescence

Photoluminescence is a technique in which light is shone on a material and its electrons are excited in a process called photoexcitation to higher energy allowed states from their equilibrium states. When the electrons return to their equilibrium states from the excited states, they give up light which they absorbed [25]. Photoluminescence is used for studying the electronic structure of semiconductors and other luminescent materials like phosphors, oxides, etc and can be used for ascertaining both how pure they are and also defects/impurities. In addition to optical absorption, this technique can be used for determining the bandgap of the materials being studied [26].

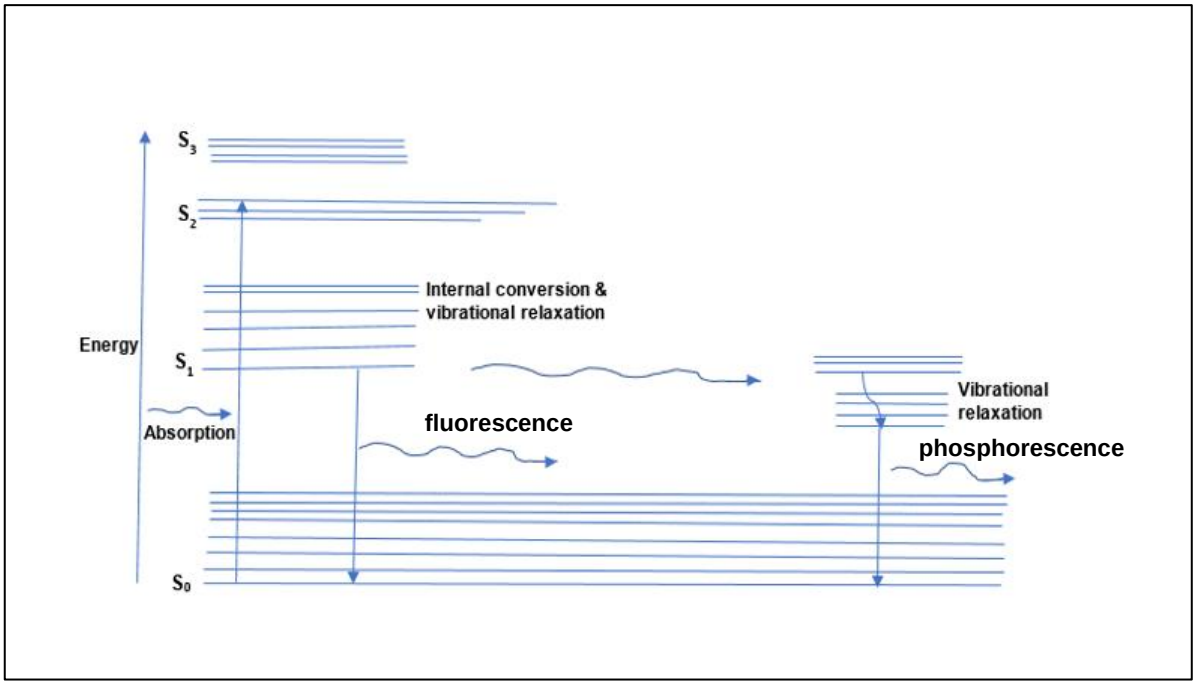


**Figure 2.15** Energy diagram illustrating absorption of light and its emission process as well as phosphorescence and fluorescence PL

Photoluminescence is a non-destructive, contactless technique that can be done even at room temperature. Typically, it uses a coherent light source, such as a laser beam for pumping electrons into the excited state and when the excited electrons return to their former energy levels via recombination with the holes, sharp and distinct peaks for each

excited level are produced and for many such transitions, a spectrum of the material being studied [27] can be produced.

Photoluminescence spectra are unique for a particular material and depend on the wavelength of the laser excitation used. Photoluminescence can be fluorescence or phosphorescence (Figure 2.15). Photoluminescence being an optical technique is only suitable for analysing samples which can emit light when irradiated.

Semiconductors can be investigated using photoluminescence measurements by getting their electrons excited with a beam of EM radiations as already explained. Their relaxation back to the ground state and recombination of the electrons with the holes results in luminescence and is accompanied with photon emission. The emitted photon wavelength is in the visible range.

A change in the size of the nanoparticles changes the emission frequency. With small nanoparticles the frequency of the emitted radiation is blue-shifted and for larger nanoparticles the frequency of the emitted radiation is red-shifted, hence the nanoparticle colour can change accordingly.

Luminescence can also be due to Cathode rays (Cathodoluminescence), from radioactive particles (Radio-luminescence), from electric field (Electro-luminescence) or due to light creating electron-hole pairs (Photoluminescence) which was the one employed in this research. The recombination of electron –hole pairs can be radiative in which case light is given out or non-radiative with no light emission. The radiative domain observed in this work ranges from the ultra-violet to the visible ($\lambda = 300 - 650$ nm).

## 2.6 Fourier transform infrared (FTIR)

### 2.6.1 Phonon and lattice dynamics

Lattice dynamics deals with the vibration of the atoms which make up a crystal. Atoms of a crystal collectively vibrate about their mean positions producing a collective vibration which forms a wave with a given wavelength and amplitude. The vibration modes in a solid are quantised and are referred to as phonons. Thus, Phonon is a quantum of lattice vibration whose wave vector is k and whose energy is $\hbar\omega$. In lattice dynamics, the determination of the normal modes of vibration in crystals has to do with the determination of the phonon energies or frequencies $\omega$ as a function of their wave vector k. Thus, phonon dispersion is the relation between $\omega$ and k and shows the complete crystal symmetry and provided k is restricted to a unit cell of the reciprocal lattice, regarded as the first Brillouin zone whose volume is $\frac{1}{v}$.

### 2.6.2 Normal modes of vibration of a crystal

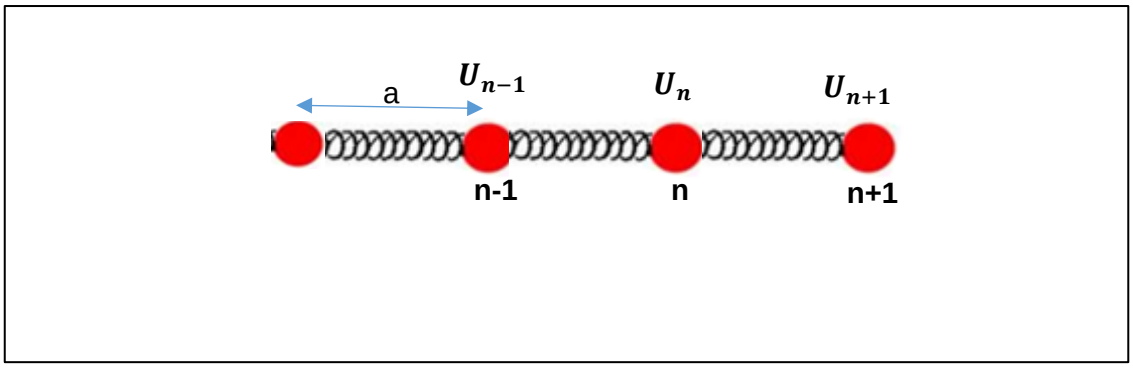


**Figure 2.16** Crystal represented as a system of connected similar particles (atoms)

For a crystal considered to be made up of an array of similar particles and connected with elastic spring as shown (Figure 2.16) :

If all the atoms in the crystal are assumed to be oscillating with the same amplitude A, the frequency of vibration $\omega$ is given by [28]:

$$\omega = \sqrt{\frac{4C}{M}} \left| Sin \frac{k}{2} a \right| \qquad (2.49)$$

Where C is the spring constant, 'a' is the equilibrium lattice spacing between the atoms

Thus for $-\frac{-\pi}{a} \leq k \leq \frac{\pi}{a}$ we have the first Brillouin zone and the maximum frequency $\sqrt{\frac{4C}{M}}$ is symmetrical and at the boundaries of the Brillouin zone, $k = \pm \frac{\pi}{2}$ (Figure 2.17).

Thus, the velocity of the wave packet $V_g$ is given by [28]:

$$V_g = \frac{d\omega}{dk} = \sqrt{\frac{Ca^2}{M}} Cos \ \frac{k}{2} a \qquad (2.50)$$

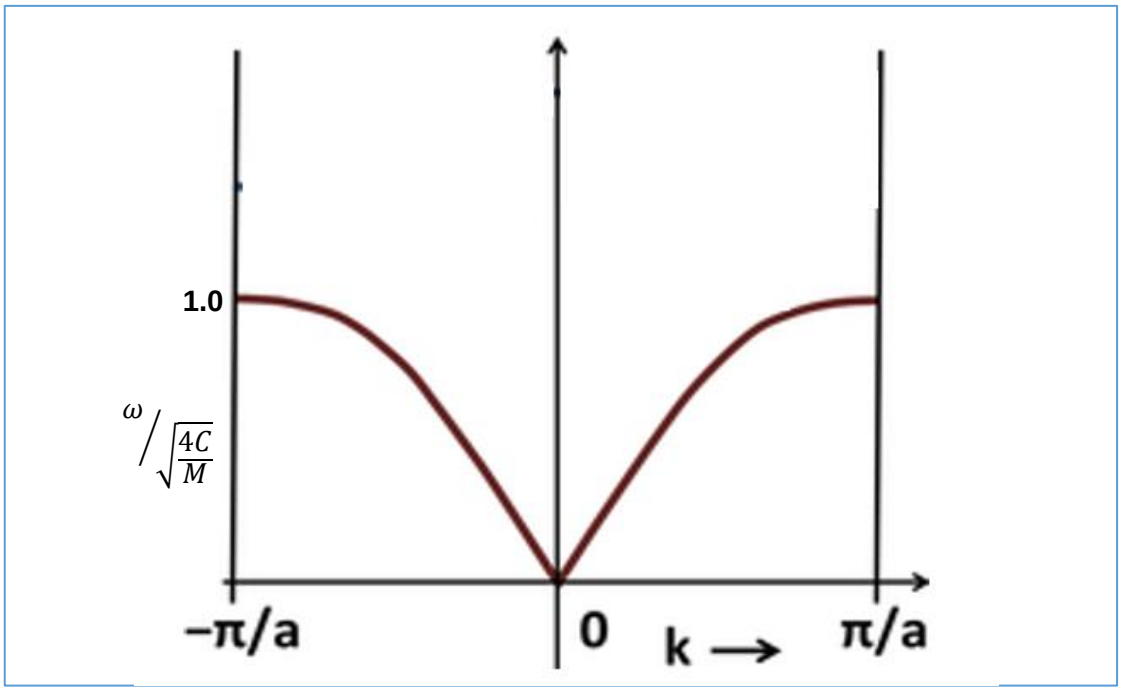


**Figure 2.17** Dispersion relation showing acoustic mode

At the edge of the Brillouin zone, $k = \pm\frac{\pi}{2}$ which makes the transmission veleocity for the wave energy to be equal to zero.

When the wavelength of the light shone on the sample is much much greater than the atomic separation 'a', $ka << 1$, the frequency $\omega$ becomes:

$\omega = \sqrt{\frac{C}{M}}\, ka$ , which means that the frequency $\omega$ becomes proportional to the wave propagation vector k and the phase velocity $V_p$ of the plane wave propagated through the material will be:

$$V_p = \frac{\omega}{k} = \sqrt{\frac{C}{M}}\, a \qquad (2.51)$$

For a diatomic one-dimensional lattice, two different atoms with masses $M_1$ and $M_2$ will be connected as in Figure 2.18.

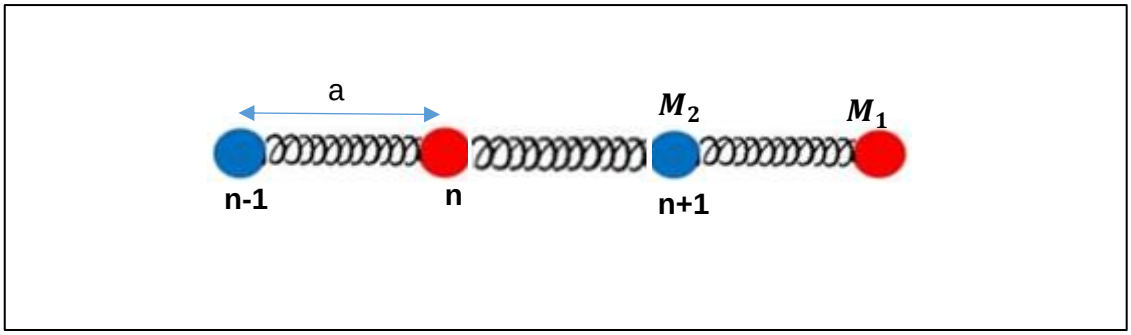


**Figure 2.18** Crystal represented as a system of two different atoms connected with springs

The solution for the travelling mode of these atoms is the result of solving the matrix [28]:

$$\begin{bmatrix} U_n \\ U_{n+1} \end{bmatrix} = \begin{bmatrix} A_1 e^{ikna} \\ A_2 e^{ik(n+1)a} \end{bmatrix} e^{-i\omega t}$$

$$\begin{bmatrix} 2C - M_1\omega^2 & -2C\ Cos\ ka \\ -2C\ Cos\ ka & 2C - M_2\omega^2 \end{bmatrix} \begin{bmatrix} A_1 \\ A_2 \end{bmatrix} = 0$$

Which gives

$$\omega^2 = C\left[\frac{1}{M_1} + \frac{1}{M_2}\right] \pm C\sqrt{\left(\frac{1}{M_1} + \frac{1}{M_2}\right)^2 - \frac{4Sin^2 ka}{M_1 M_2}} \qquad (2.52)$$

Equation 2.52 gives two curves, one for the optical mode and the other the acoustical mode (Figure 2.19).

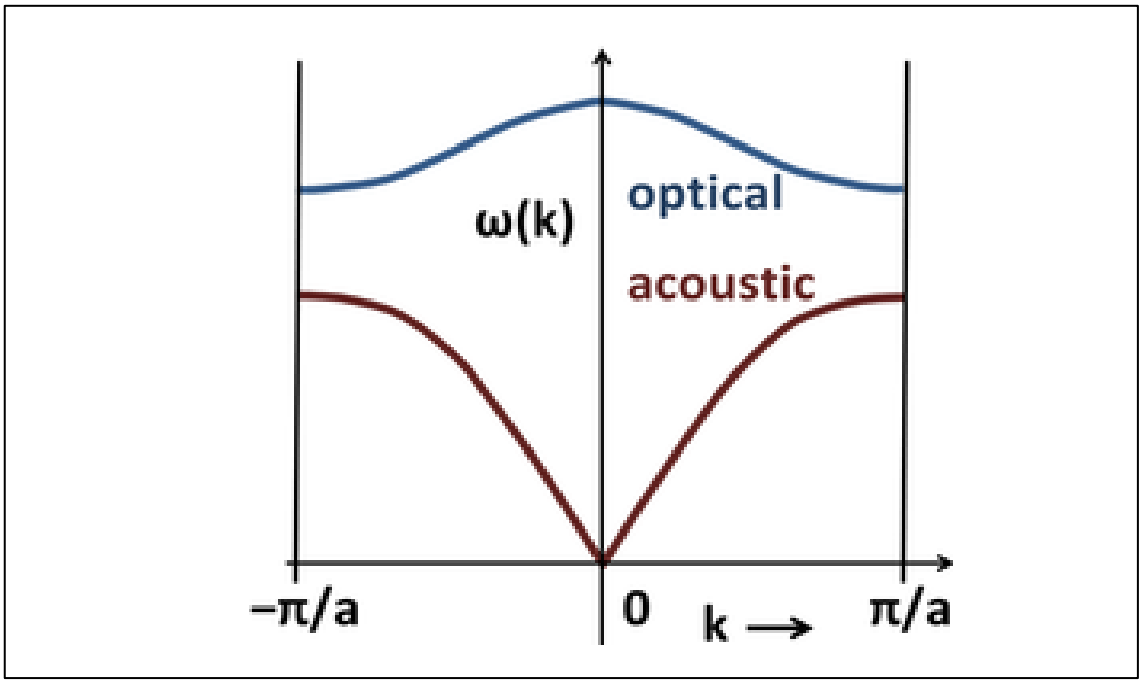


**Figure 2.19** Dispersion relation showing optical and acoustic modes

Thus when $\omega = 0$, the waves have same amplitude $(A_1 = A_2)$ and are in phase and the molecule will vibrate as a rigid body as in a mechanical system.

Increasing the value of the propagation vector k from zero will linearly increase the frequency $\omega$ as shown by the acoustic curve. At $k = 0$, there is a peak frequency $\omega_0$ at the centre of first Brillouin zone given by [28]:

$$\omega_0 = \sqrt{2C\left(\frac{1}{M_1} + \frac{1}{M_2}\right)} \qquad (2.53)$$

For the optical mode, when $k = 0$, $M_1A_1 = -M_2A_2$, thus optical vibrations in a diatomic molecule such as zinc oxide (ZnO) studied in this research occurs with the the centre of mass fixed while the two atoms' movement is out of phase as shown in Figure 2.20.

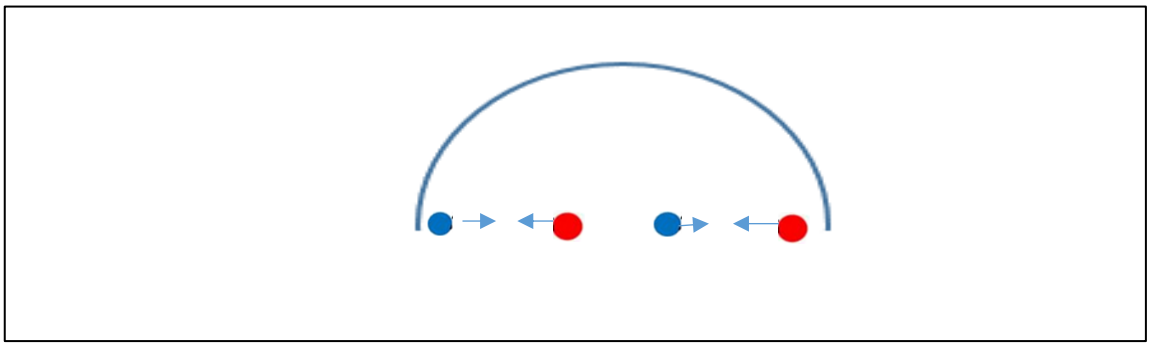

**Figure 2.20** Out of phase movement of atoms in a molecule

## 2.7 Molecular vibration modes and FTIR interpretation

In this research , samples are exposed to EM radiations and their response to these help in their characterisation. Every sample contains functional groups and when light is shone on functional groups, the bonds associated with each functional group can bend, stretch or wag etc. at varied frequencies. The vibration of the molecular bonds can be temperature dependent. A functional group (molecular bond) will absorb light if the

frequency of the light it receives matches its own frequency of stretching, bending or wagging. Thus an infrared spectra gives a pattern which is a combination of the unique response of the functional groups and hence molecule bonds present in a given sample. As illustrated in Figure 2.15, the spectra consists of a set of absorption peaks which may be sharp, broad or narrow and the peak intensity can be sharp or broad and short or sharp and long and these occur at specific wave numbers.

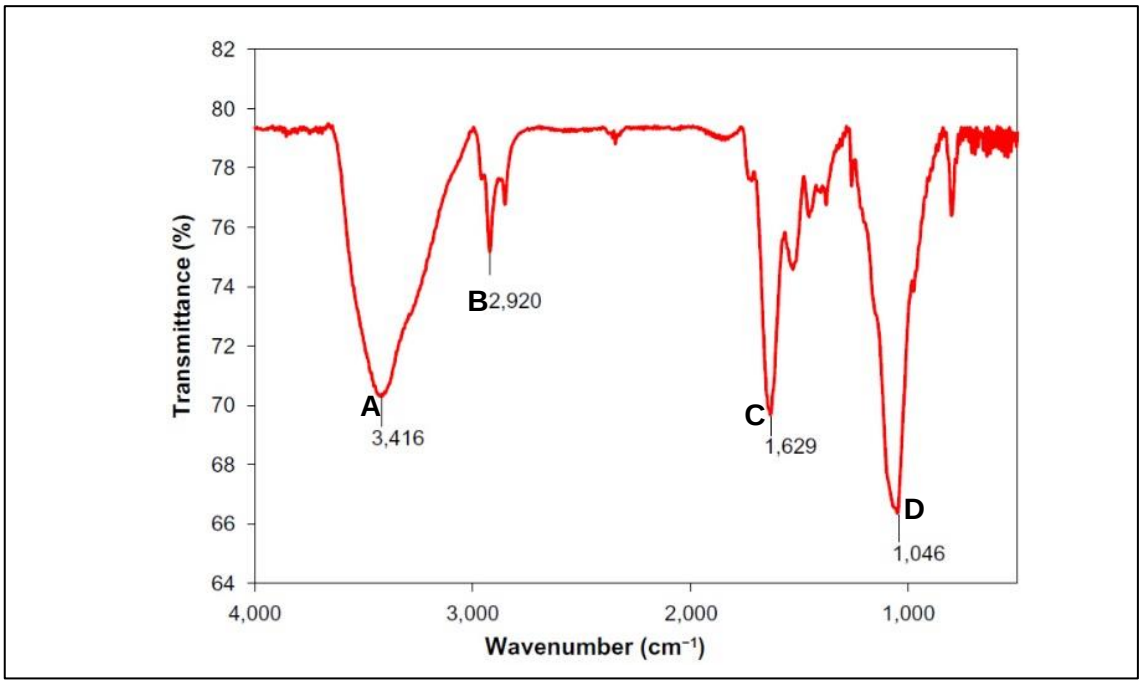


**Figure 2.21** FTIR of purified silver nanoparticles synthesized using panchakavya leaf extract [17]

An IR spectra has two regions namely the functional group region (1800 - 4000 $cm^{-1}$ ) and the fingerprint region ( 0 - 1500 $cm^{-1}$ ). Every organic molecule has its finger print region which is unique to it and this can be ascertained with the help of a chart of functional groups and their corresponding wave numbers as well as intensities.

## 2.8 Molecular vibration modes

Molecular vibration modes are (i) the Stretching vibration modes (Figure 2.22) which can be symmetrical or antisymmetrical, and (ii) the Bending vibration modes (Figure 2.23) which includes the scissoring, rocking, wagging and twisting modes. These are the modes which determine the frequencies at which the molecular bonds can either absorb or transmit light which falls on them.

**s**

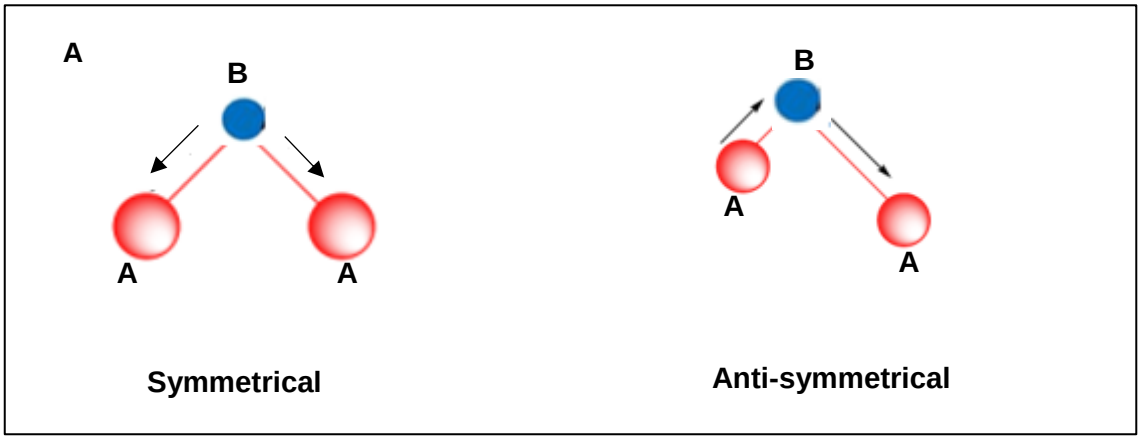


**Figure 2.22** Stretching vibration modes

In the symmetrical mode, the two A atoms stretch from B simultaneously in the same direction as shown with the arrows and the bond lengths are equal while in the antisymmetric mode, while A moves towards B on one side, it moves away from B on the other side and the bond lengths are different.

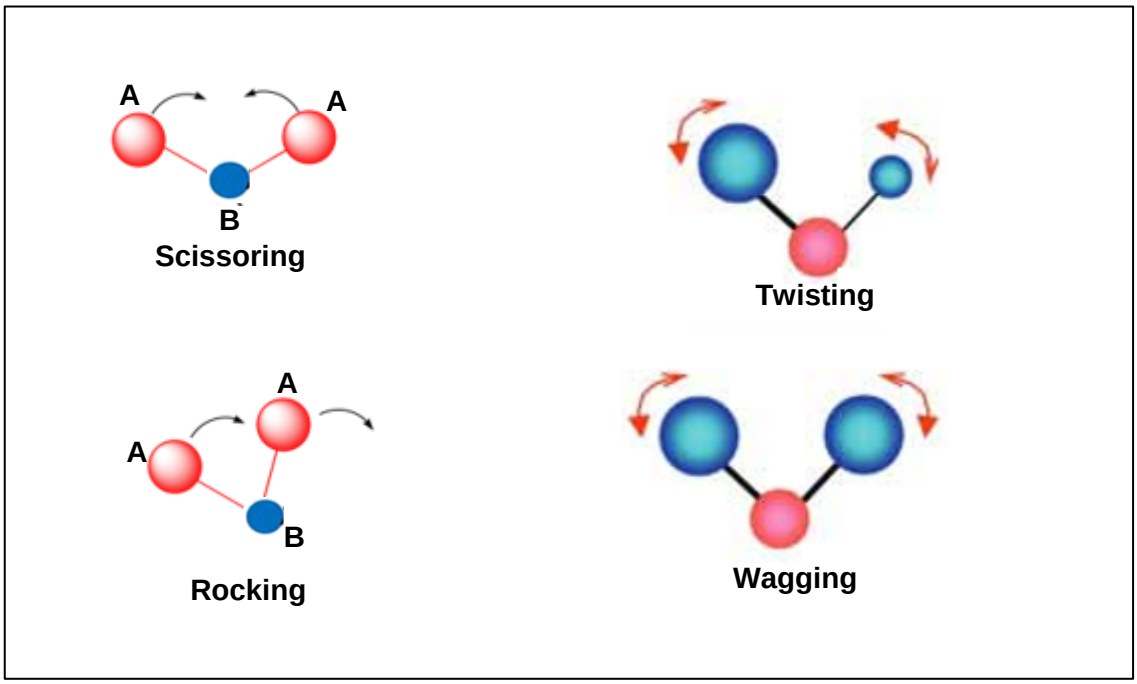


**Figure 2.23** Bending vibration modes

In the scissoring mode (Figure 2.23) similar atoms approach or depart from one another in the plane of vibration. The wagging and twisting vibration modes (Figure 2.23) are out of the plane of vibration as shown with the arrows.

### 2.8.1 Bond types and strength and Infrared (IR) Spectra

Molecular bonds for instance those of carbon atoms can be single bonds like (C-C) , double bonds (C= $C$) or triple bonds (C≡ $C$). While single bonds are longer, flexible and peaks due to them are found in regions with low wave numbers, they are the weakest of the three bonds. Double bonds on the other hand are shorter but stronger than single bonds. The strongest of the three bonds are the triple bonds which are short, can be likened to a stiff spring and are found in the region with high wave numbers. Thus (C≡ $C$) > (C = $C$) > (C − C).

Molecular bonds can be between a lighter atom and a heavier one and this as will be discussed later impacts on the wave number region of the IR where it will be located.

An infrared spectrum is a graph (Figure 2.21) which shows the variation of the percentage of transmitted light (% Transmittance) with wave number k ($cm^{-1}$) . Low points on this graph are points of increased absorption while high points represent low absorbance but more transmittance of light. Each functional group has its vibration frequency and hence characteristic absorption bands. As already mentioned, depending on the functional group a sample contains as well as the vibration mode/modes of its molecular bonds, light shone on it can either get absorbed or transmitted. If the vibration mode of the molecular bond in a certain sample has a frequency $\omega_1$ and light of this frequency is shone on it, that bond will absorb all of this light and none of it will be transmitted: so, zero transmittance % will be measured by the detector. If, however light of frequency less than $\omega_1$ is received by the bond, this frequency not being up to its own will all get transmitted and the detector in the measuring instrument will record a 100% transmittance resulting in a high peak. The third case will be if the light incident on the bond has a frequency greater than $\omega_1$. In this case the bond will absorb the part of light frequency which corresponds to its characteristic frequency, but light which was not absorbed will be allowed to pass through resulting in some percentage of light transmission which the detector will pick up.

Thus, the IR spectra plots show high peaks which are for transmitted light and lower peaks which are for absorbed light. This is how the IR instrument shows which molecules and hence bonds are present in a studied sample.

For a spring, Hooke's law gives a mean frequency as [29]:

$$\bar{\upsilon} = \frac{1}{2\pi c}\left[\frac{f(M_1+M_2)}{M_1M_2}\right]^{1/2} \qquad (2.54)$$

where f is the force constant of the spring or bond strength in our case and $M_1$ and $M_2$ are the masses of the atoms that make up the molecule, c is the speed of light in $\mathrm{cms}^{-1}$. This expression can be used to explain bond vibration in infrared spectroscopy [29] and the vibrational frequency assumed as $\bar{\upsilon}$, represents the wave number in $\mathrm{cms}^{-1}$.

Equation 2.54 shows that the lighter the connected atoms, the higher the frequency of bond vibration and hence wave number and conversely that stronger bonds have higher vibrational frequencies and hence higher wave numbers.

### 2.8.2 Functional groups in a sample and their Identification

Functional groups are represented by peaks in an IR spectra and electron withdrawing or donating as well as electron delocalization and hence resonance can have some effect on the wave number of functional groups. Functional groups can be identified in many ways: It can be done with the help of standard tables which show functional groups, their intensities (sharp, broad, Etc) and associated range of wave numbers and hence regions in an IR spectrum. For instance, while the O-H single bond absorption band are broad due to hydrogen binding, they are strong and are found in the high wave number region of the IR spectra (3650-3200 $cm^{-1}$). C-H bonds are medium and found in the range 3300-2700 $cm^{-1}$ while the carboxylic acid is found at 3000 $cm^{-1}$ . Triple bonds are found in the range 2100-2260 $cm^{-1}$ and the double bonds in the range 1680-1550 $cm^{-1}$. The identification of a specified molecule from a list can be done by relating the observed peaks (in the IR spectrum) and their shapes/ intensities to possible options and figuring out which is the most probable from the list. Some functional groups can have many absorption bands and hence peaks depending on the number of vibration modes (stretching, wagging, rocking etc) they have. In this work phenols and flavonoids suspected to have aided the reduction of the metal into nanoparticles were of interest and they contain the hydroxyl group (OH) meaning that they are likely to be located in the high wave number region.

The peaks in an IR spectrum also depend on the masses of the atoms which form the bonds that vibrate to give the peaks. For instance, carbon can form bonds with different atoms and give different peaks. Thus, carbon bond with hydrogen (C-H), carbon with carbon (C-C), and carbon with chlorine (C-Cl) appear at wave numbers 3000 $cm^{-1}$ , 1200-1000 $cm^{-1}$ , and 800-600 $cm^{-1}$ respectively because the masses of the second atom increases as shown (H $<$C $<$Cl).

## 2.9 Crystal lattice, X-ray Diffraction (XRD) and Bragg's law

When a beam of X-rays is directed on a crystal, there is an elastic scattering from the crystallographic planes [30] of the atoms (Figure 2.25) and X-ray diffraction patterns are formed.

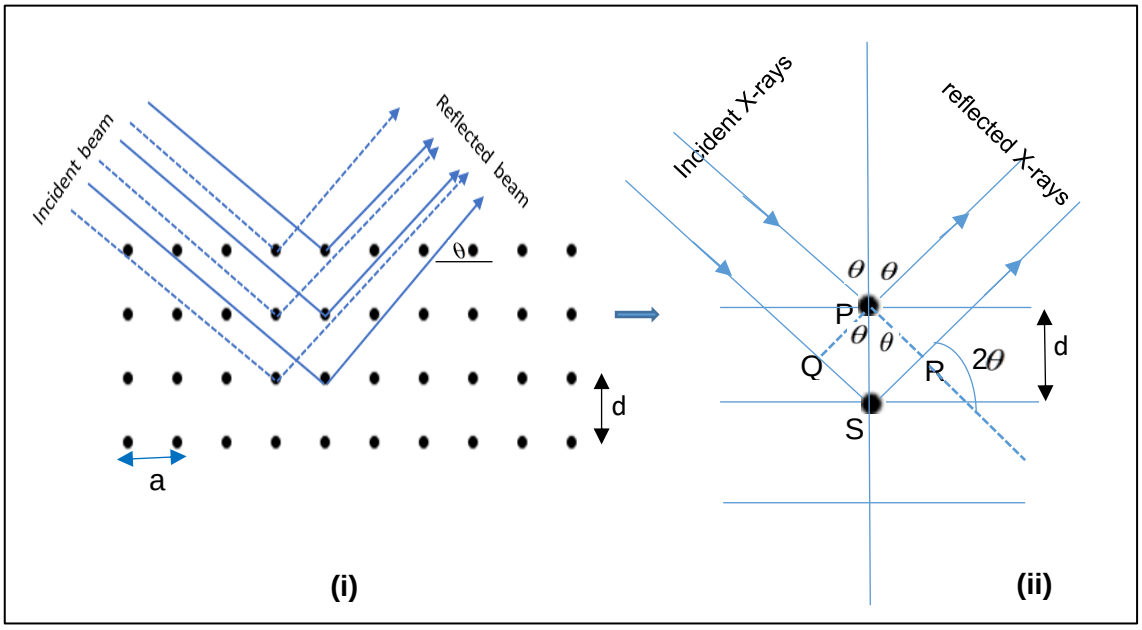


**Figure 2.24 (i) X**-rays diffracted from lattice planes (ii) illustrating path difference between rays from two consecutive planes.

The periodic arrangement of atoms / molecules in a crystal gives an array of planes parallel to one another (Figure 2.24 i) with an interatomic spacing 'a' of the order of 1Å and constitutes a 3D diffraction grating [31]. Each atom receiving the X-rays (which are a form of electromagnetic radiation with an associated electric field) becomes a coherent source of X-ray radiation which when superimposed on one another results in X-ray diffraction patterns. The path difference between rays from consecutive planes (QS+SR) (Figure 2.24 ii) according to Bragg's law Equation (2.55) for a maximum will be an integral multiple of wavelengths.

Thus

$$n\lambda = 2d\ Sin\ \theta \quad (2.55)$$

where n is the order of reflection and n =1,2,3….and the highest order is for n = 1, d is the distance between the planes of the crystal.

If $2\theta$ is known, $\theta$ can be determined and so also can the path difference from two consecutive planes. Varying the value of $\theta$ results in different maxima/peaks which then form the diffraction pattern. Each peak in an XRD pattern corresponds to a value of d which in turn depends on the values of the miller indices $h, k\ and\ l$.

The X-rays used for this work has wavelength λ.= 0.1542 nm and for n = 1 (first order), Equation 2.55 becomes $Sin\ \theta = \frac{\lambda}{2d}$

For silver nanoparticles the peaks are 111, 200, 220, 311 …. etc. while for zinc oxide nanoparticles the strong peaks are 100, 002, 101, 102, …...etc

### 2.9.1 Miller indices

Miller indices represented by h, k, l are numbers which show the intercepts of the planes with the $x, y, and\ z$ axes.:

In Figure 2.25 i, the plane only intersects the x-axis, while in 2.25 ii the planes intersect the y-axis and in 2.25 iii, the planes intersect the x and y-axes but not the z-axis.

For cubic systems, the plane separation d is related to the miller indices as shown in equation 2.56:

$$d_{hkl} = \frac{a}{\sqrt{h^2+k^2+l^2}} \quad (2.56)$$

Thus, any combination of $h, k,$ and $l$ that will make $\sqrt{h^2 + k^2 + l^2}$ = 1, will give a plane separation ‘d’ equal to the interatomic separation ‘a’. For the Simple cubic structure (SC), the planes which satisfy this condition are: 100, 010 or 001.

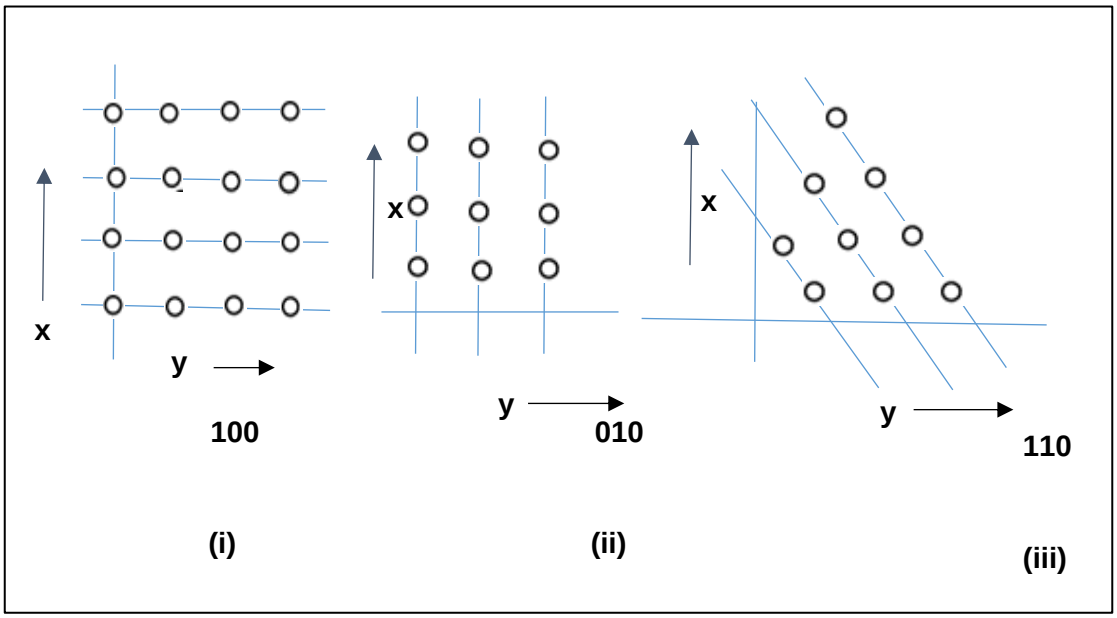


**Figure 2.25** Miller indices $h, k, l$ for three planes illustrated

There is also the cubic rule which predicts where peaks will appear for different crystal structures. Thus, for the Body centred cubic (BCC) structure, peaks will appear where the sum of the miller indices is an even number and the planes which satisfy this condition are: 110, 200, 211, 220, and 222. For the Face centred (FCC) cubic structure, peaks appear where the miller indices are entirely even or entirely odd and the planes which satisfy this are 111, 200, 220. and 222.

The XRD pattern of an analysed sample helps in the identification of its crystal structure and the peaks in an X-ray spectrum can be compared with the standard ones as presented in JCPDS [32] to know the crystal structure of a sample or detect defects in crystals. The peaks in an X-ray spectrum of powder samples can also be used for calculating the lattice constant as well as average crystallite size [33] of any sample of interest. This is done by determining the full width at half maximum (FWHM) value from a peak of an X-ray spectrum of a sample. A low FWHM implies that the grains are large and that the sample has good crystallinity while a high FWHM indicates smaller particles and poor crystallinity. After FWHM values are estimated as indicated in

Figure 2.26 and the average crystallite size can be determined using Scherrer's equation [33,34] Equation (2.57):

$$B(2\theta) = \frac{K\lambda}{L\,Cos\,\theta} \qquad (2.57)$$

For any peak in an X-ray spectrum, $\theta$ can be calculated and hence the value of L can be determined.

Where L is the crystallite size, λ is the wavelength of the X-rays used. K is a constant which for spherical particles is 0.9 and $B$ is the FWHM.

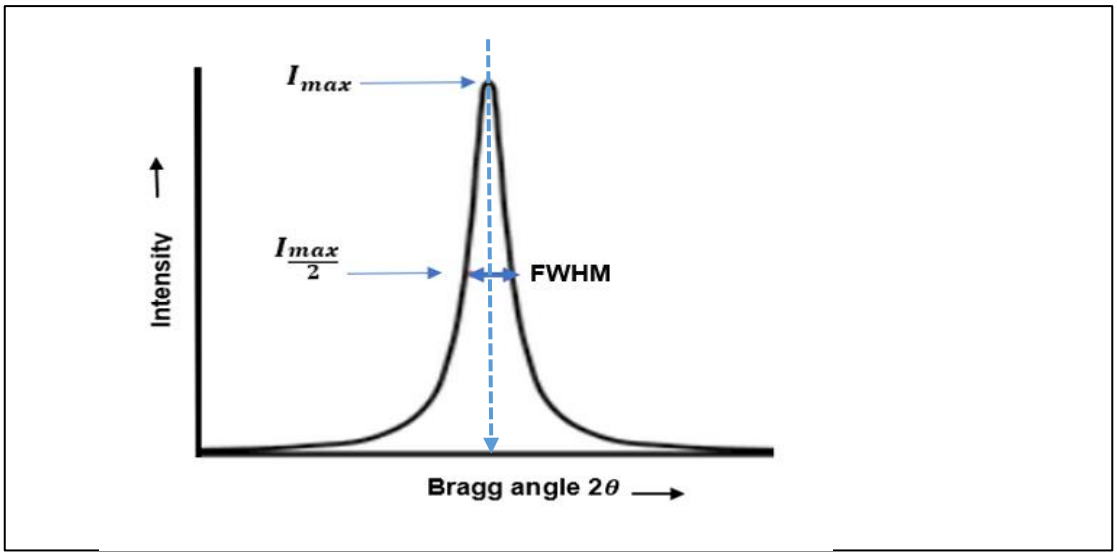


**Figure 2.26** Diagram to show how FWHM can be determined.

# Chapter 3

# Experimental methods

## 3.1 Introduction

This chapter deals with the instruments which were used for the characterisation of the produced nanoparticles. It describes their main features and spells out the functions of their components. It also explains how each instrument works and how experimental data for our samples can be generated from it. It gives some other uses of each instrument and finally what it was used for in this present research.

## 3.2 Electron Microscopy

Electron microscopy uses a beam of accelerated electrons which have high energies of the order of 100 keV and being of low wavelength, they produce high spatial resolution. When the electron beam is made to interact with the sample, via secondary electron production, scattering, diffraction and transmission, the sample morphology is revealed and its shape, size and sometimes arrangement of its atoms can be known. In this research, two electron microscopy techniques namely Transmission Electron Microscope (TEM) and Scanning Electron Microscope were employed in the analysis of the biosynthesized silver and zinc oxide nanoparticles.

### 3.2.1 Transmission Electron Microscope (TEM)

A transmission electron microscope (TEM) analyses thin samples of the order of about 200 nm or less. It typically uses accelerating voltages in the range 60 kV-120 kV,

though voltages as high as 300 kV can also be used**.** Figure 3.1 shows the parts of a TEM instrument and how it works to give the image of a sample.

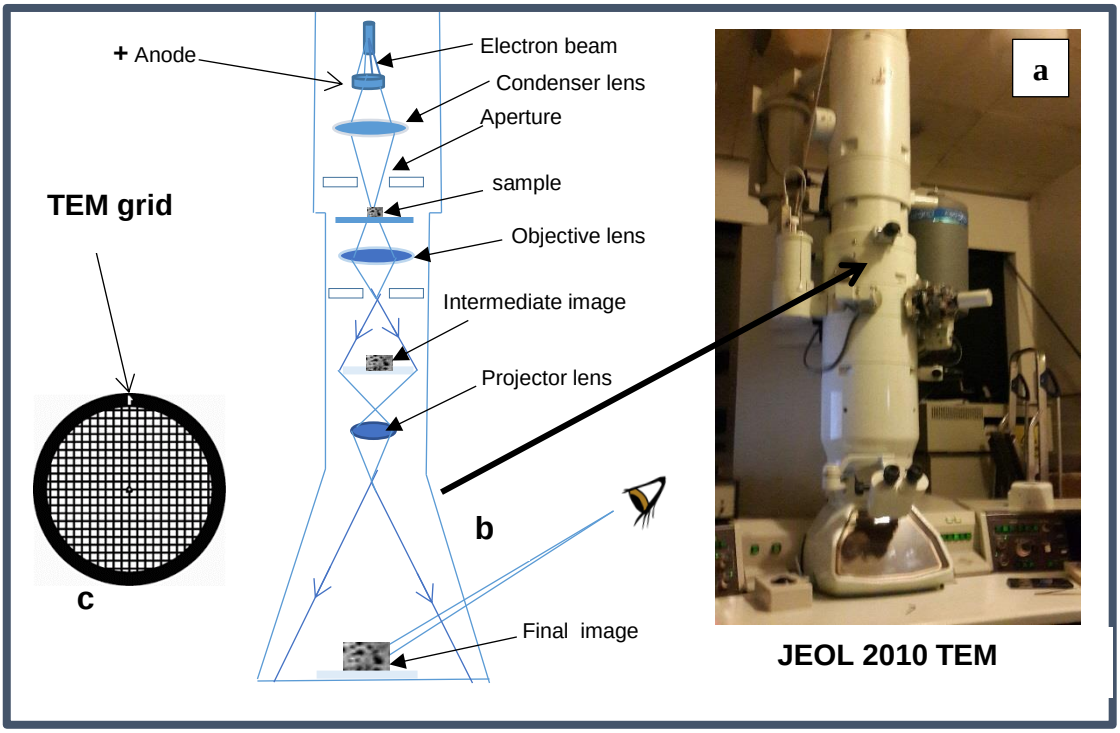


**Figure 3.1** (a) Photograph of **JEOL 2010 TEM** (b) Diagram showing beam direction for image production (image re-drawn as in JOEL 2010 manual) (c) holey carbon grid.

Samples meant for TEM analysis should be electrically conductive, and transparent to the electron beam. They must be stable while in a vacuum with the electron beam impinging on it and should be without artefacts or hydrocarbon contaminants. [35]. TEM sample preparation methods differ depending on the sample's phases, physical or electrical properties [36]. Methods used include ion milling and crushing or grinding [35]. Others are polishing or etching, ultrasonic sonication [36] and focused ion beam (FIB) methods [37]. For metal samples or alloys, electrolytic polishing can be used to

make them transparent. Transmission electron microscopes can be used for studying the sizes, shapes or cross-sections of a sample and sample thickness can be between 30 nm-200 nm so that the electron beam can pass through them. Furthermore, properties such as dislocation densities, defects in materials as well as mechanical alloying effect in materials [38] can be studied using TEM.

TEM grids which can be used include among others copper grids, MO grids, and Holey carbon grids, which were used in this research. Transmission Electron images called micrographs are on a grey scale with lighter regions showing less electron absorption and darker ones indicating more electron absorption. TEM images can be analysed using Image J or Gwydion software. The TEM instrument model used in this research is JEOL 2010 and uses an accelerating voltage of about 10 kV.

The nanoparticle sample preparation was done by an ultrasonic sonication of a grain of the nanoparticle powder sample in 40 $\mu L$ of ethanol for between 15 minutes to 20 minutes to disperse the nanoparticles and with a pipette, 2 $\mu L$ of the suspension was dropped on a Holey carbon grid which was then exposed to a hot yellow filament light bulb to dry. The Holey carbon grid with the deposited sample was then viewed under an optical microscope to confirm that the nanoparticles were fairly distributed on the grid. The sample was then introduced into the TEM machine for imaging.

When a high voltage (range 60 kV-200 kV) is applied to the TEM machine, a beam of electrons is accelerated in a vacuum towards the sample via electromagnetic lenses (Figure 3.1). As the electron beam interact with the sample, they exchange energy with it and depending on how dense the sample under investigation is, some of the electrons can be scattered and some can even be lost. The electron beam which gets to the bottom of the microscope impacts on a fluorescent screen or detector camera to produce a shadow image of the sample under investigation.

### 3.2.2 Scanning Electron Microscope (SEM)

A scanning electron microscope illustrated in Figure 3.2, gives detailed information on the structure and composition of a specimen by scanning its surface line by line [39].

This microscope consists of an electron source, a thermionic gun or field emission, a set of electromagnetic/electrostatic lenses to focus the electron beam on the sample under investigation. The instrument also has a vertical chamber through which the electron beam travels as it makes its way to the sample, a sample stage, an X-ray detector (EDS) and a computer which displays the image of the sample analysed.

s

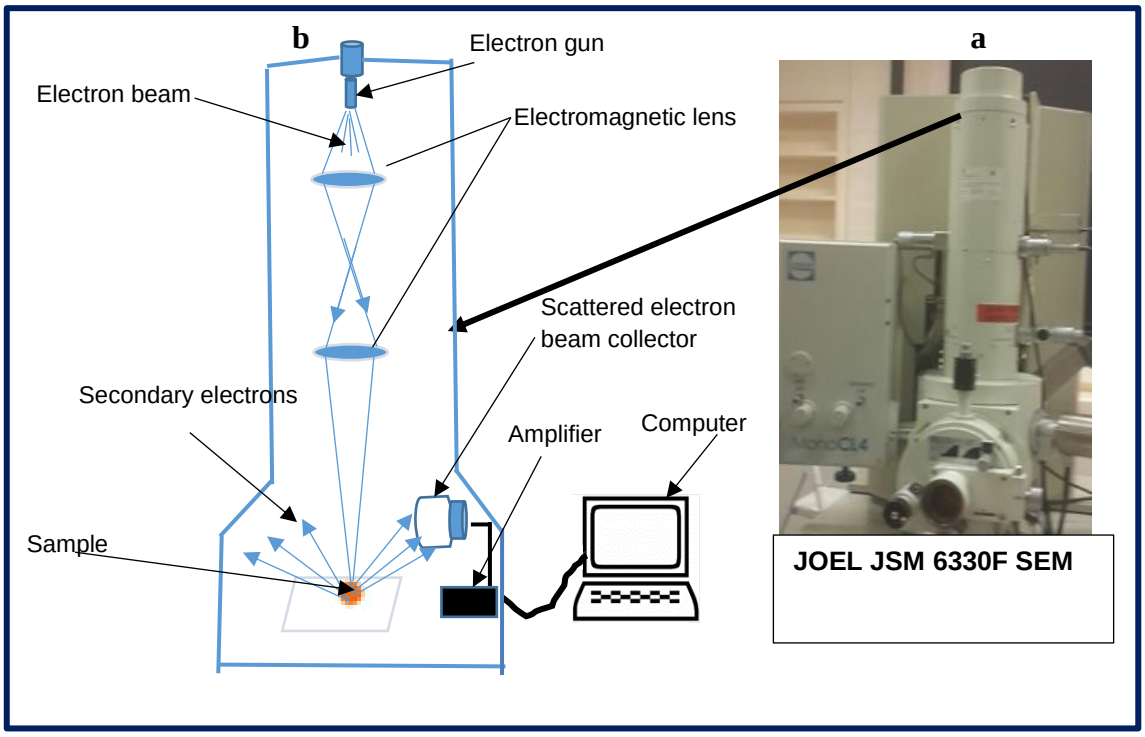


**Figure 3.2** (a) Photograph of JOEL 6330F SEM (b) SEM re-drawn from its manual and showing electron beam directed towards sample and its interaction with sample.

When the electron emitter sends out a beam of energetic electrons, they travel down the vertical chamber to and through the twin electromagnetic lenses which act like optical lenses bringing electron beam to a focus on the sample. Two sets of electrons are produced because of the interaction of the beam with the sample. These are the secondary electrons which are dislodged from the sample surface by the electron beam and the backscattered electrons which come from within the sample. The signal due to

these two sets of electrons is picked up by the positively charged Faraday cage whose voltage is about 300 V and sent to the computer for interpretation and display of the sample image taken.

Scanning Electron Microscopy (SEM) detects the secondary electrons from the sample and uses it to form the required image. Conversely, the backscattered electrons which emanate from within or beneath the sample surface as X-rays get diffracted and give the crystalline structure of the sample. SEM can be used for studying microstructures, faults in crystals, sample surface contamination as well as cracks in materials.

Though SEM is mostly used for analysing solids, it can also be used for analysing organic samples provided they can withstand the vacuum environment within the instrument as well as the electron beam intensity. While the white regions of the image indicate areas which lose a lot of secondary electrons, the black coloured areas show areas which lost few secondary electrons.

For this research, the JOEL JSM 6330F field emission scanning electron microscope which uses accelerating voltage of about10.0 kV and current in the range 2 $\mu A -$ 10.5 $\mu A$ with a working distance (WD) of about 7 mm was used for studying the size distribution and shapes of zinc oxide nanoparticles in powder form. SEM sample preparation was done by placing the sample to be analysed on a conductive adhesive and sticking it on a stub whose size can fit into the sample holder slot. After this is done, the sample was then carefully introduced into the instrument (while ensuring that the vacuum environment through which it passes does not suck in the sample holder). The sample is then placed onto the sample stage before the sample holder is then withdrawn from the vacuum chamber. The instrument is then used for taking images of the nanoparticles which are saved for analysis later. The SEM nanoparticle size analysis was done using GATAN micrographs software. Unlike a Transmission Electron Microscope (TEM), a scanning Electron instrument uses a relatively low voltage of range 1 kV-30 kV.

## 3.3 UV-vis spectrophotometry

Spectroscopy is a study of the interaction of electromagnetic radiation with matter. By analysing the light intensity dependence on the wavelength of light energy which hits a sample, the molecules present in it and hence its chemical structure can be revealed. As already explained in section 2.2 of this thesis, a material absorbs light maximally if it transmits very little light and its light absorbance depends on its coefficient of absorption. Light reflectivity from the material also depends on the refractive index of the material as well as the path through which the light has to travel as it passes through the material (sections 2.5-2.6).

A follow-up to this is Beer- Lambert law which gives light absorbance A by a material as a function of the concentration of the molecules in it as well as the length of the path through which the light travels. Thus:

$$A = \varepsilon c l \qquad (3.1)$$

where $\varepsilon = molar\ absorptivity\ in \frac{L}{mol}.cm$, $l =$ length of the path through which light travels (width of cuvet) and $c =$ concentration of the molecules in the sample)

A UV-Vis spectrophotometer (Figure 3.3) can be used for studying the kinetics of a chemical reaction [40] to determine the rate constant of a reaction. The instrument can also be used for determining the quantity of analyte in a sample [41] and the particular analyte a sample contains [42]. This spectrophotometer measures the optical response of a material from the ultra violet range (10 nm – 400 nm) to the visible range (400 nm – 750 nm). Light shone on a material gets absorbed in fixed amounts called quanta resulting in the excitation of its electrons from a lower energy state $E_1$ to a higher one $E_2$. In these excited states, the electrons are unstable and will need to relax and return to lower energy states. Thus they give up whatever energy they had acquired in the form of electromagnetic radiations.

This transition is between electronic energy levels as explained in chapter two and the change in energy $E = E_2 - E_1$.

where $E = h\mathcal{V}$ (3.2)

and $E = \frac{hc}{\lambda}$ $(\mathcal{V} = \frac{c}{\lambda})$ (3.3)


**Figure 3.3** Photograph of Shimadzu UV-2600 spectrophotometer

A spectrophotometer (Figure 3.4) comprises of a light source L, a monochromator, a beam splitter, a detector and a computer for the display of the resultant spectra of the sample analysed. The monochromator consists of two slits S1 and S2 separated by a prism or diffraction grating. When white light which consists of various wavelengths is sent from the source lamp L, it travels as a parallel beam to the monochromator and then through the first slit S1 unto the prism which refracts it depending on the selected diffracting grating. Only light of one wavelength passes through the second slit S2 and then to the beam splitter.

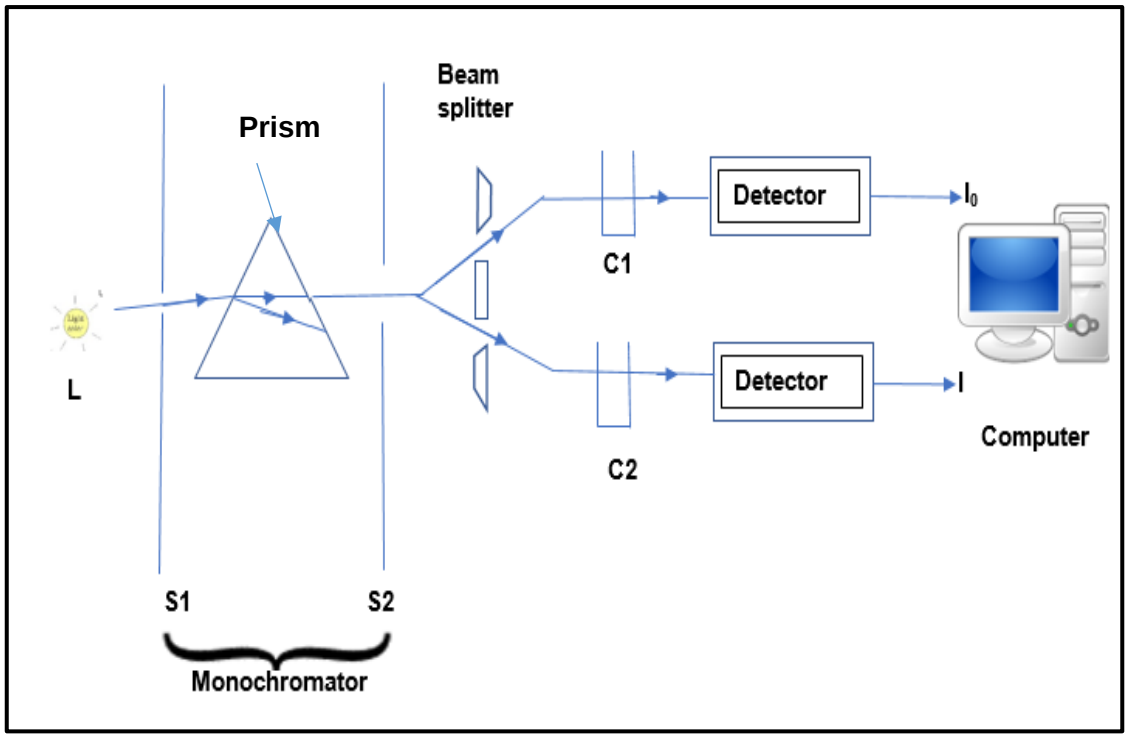


**Figure 3.4** Illustration of the essential components of a Spectrophotometer and how it works to display a spectrum of a sample (Diagram redrawn by Author)

The beam splitter divides the beam of light received into two equal parallel beams such that one with intensity $I_0$ passes through the reference path (cuvette C1) and the other with intensity I through the sample cuvette C2 with a net change in light intensity ($I_0 - I$) which is then measured. Light with transmittance $T = \frac{I}{I_0}$ gets through to the detectors which are photocells. Usually the current generated by these photocells are low and have to be sent to an amplifier which amplifies the sent signals to measurable values which the computer displays. The graph which illustrates the relationship of percent transmittance %T and light absorbance A with concentration of species in solution is shown in Figure 3.5.

For this research, the model of spectrophotometer used is Shimadzu UV-2600 (Figure 3.3) which is equipped with an ISR-2600 integrating sphere attachment in the range 220 - 1400 nm. This instrument can be used for running absorbance spectra for both liquid and solid samples. It has one compartment for liquid samples and another for solid samples. Thus, unlike conventional UV-Vis instruments, one cuvette is used for liquid sample analysis.

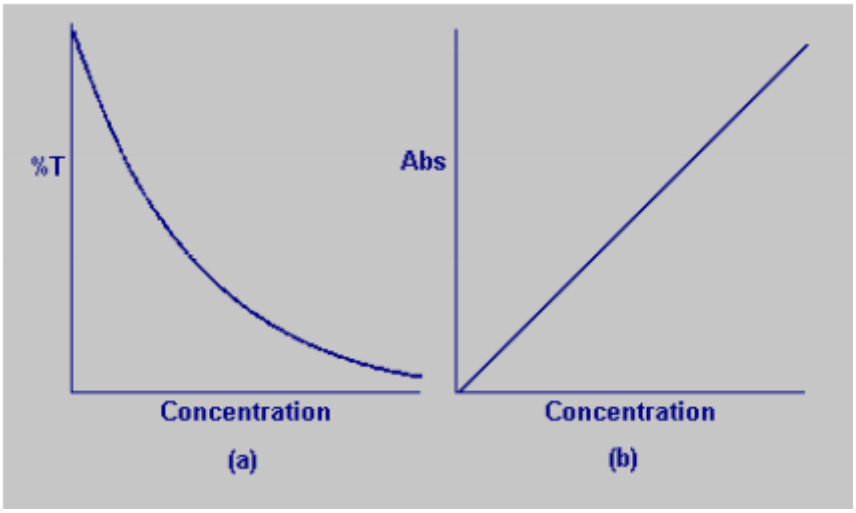


**Figure 3.5** Graph of percent transmittance and light absorbance by sample with concentration.

To run the absorbance spectrum of the silver nanoparticles, the instrument was first turned on for one hour to warm up then the range for the desired spectra was set at 220 nm-1400 nm. The property to be measured (absorbance spectrum, reflectance spectrum etc) was also selected. The sample cuvette of volume about 2.5 millilitres was first filled with water and placed in the sample compartment and with the computer, the baseline or auto zero command was given. This allows the light from the instrument to pass straight through to the detector for the light intensity $I_0$ to be derived. After this, the cuvette is emptied, dried and the diluted silver nanoparticles (one part to three parts of

milli Q water) was introduced and scanned and the light intensity now will be I. Light absorbance by the sample A will therefore be given by $A = \log_{10} \frac{I_0}{I} = \varepsilon c l$.

The intensity of the radiation which emerges when the cuvette contains water is usually greater than that when the sample cuvette contains the nanoparticle sample ( $I_0 > I$).

(where $I_0$ is the incident light intensity, I is the transmitted light intensity, $l$ is the path length through the sample, c is the concentration of the absorbing species and ε is the molar absorptivity).

In contrast, the zinc oxide nanoparticles were in powder form and so to run the UV-Vis of this ZnO powder, the powder sample holder was first filled with Barium sulphate powder levelled and covered and the baseline or Auto zero command as before was given. With this done, the sample container was emptied, wiped clean with ethanol and filled up with the zinc oxide Nano powder and scanned. For this sample, the absorbance spectra as well as the diffuse reflectance spectra were run. While the absorbance spectra gave the sample peak absorbance at a particular wavelength, its diffuse reflectance spectra gave the reflectance value R % which was used for determining the value R that was then substituted into the Kubelka - Munk function (Equation 3.4) and using the Tauc relation (Equation 3.5) the Tauc plot , a graph of $(F(R)E)^2$ against energy $(eV)$ was plotted and from it, the energy band gap $E_g$ of the zinc oxide nanoparticles was determined.

$$F(R) = \frac{(1-R)^2}{2R} \qquad (3.4)$$

$$(h\upsilon\alpha)^{\frac{1}{n}} = A\left(h\upsilon - E_g\right) \qquad (3.5)$$

where $h$ is a Planck constant, $\upsilon$ is the frequency of the light shone on the sample, α = F(R) and $n = \frac{1}{2}$ for zinc oxide [3]

## 3.4 Photoluminescence (PL)

Photoluminescence (PL) is an absorption and emission process in which a source of laser light shone on a sample excites and moves the electrons in it from the ground state to the excited state. In this excited state the electrons are unstable and will get reverted to the ground state resulting in the emission of radiations and giving out the characteristic spectra of the sample under investigation. The details of the theory of this technique are given in section 2.5.4 of this writeup. Photoluminescence spectra are unique for different materials and depends on the wavelength of the laser excitation used. The diagram of the PL instrument used for this work is as illustrated in Figure 3.6.

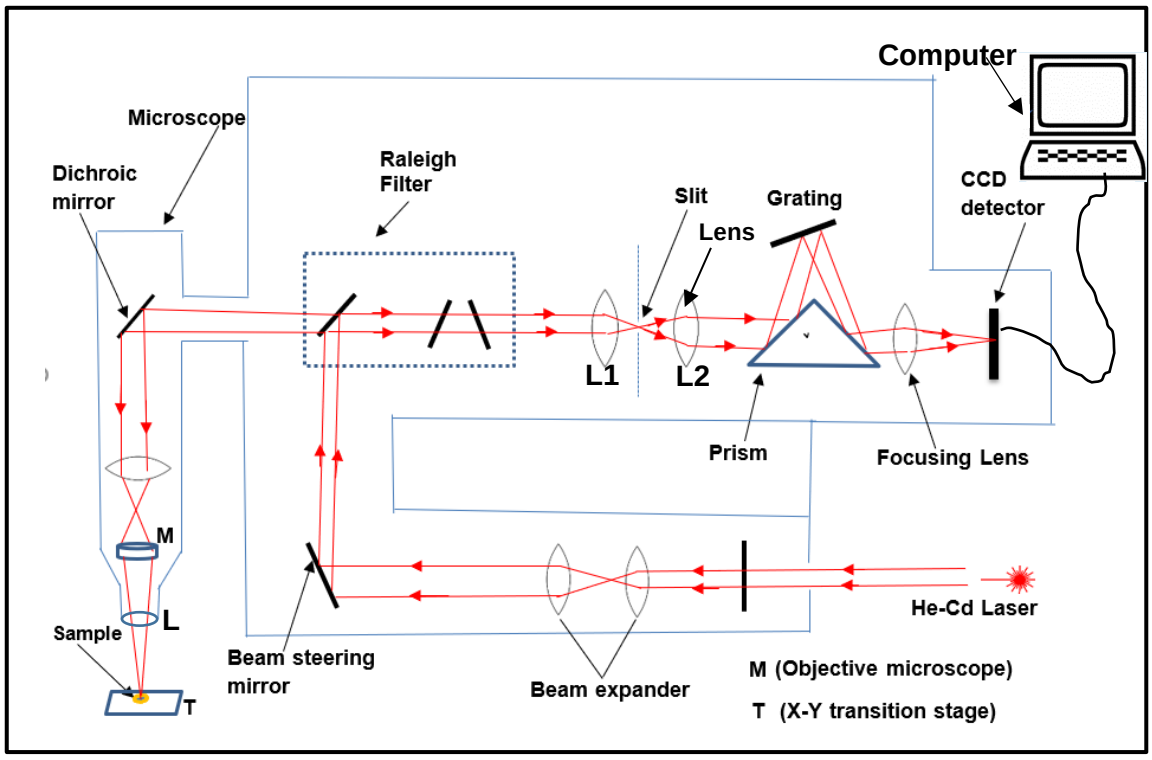


**Figure 3.6** Diagram showing the main parts of a PL instrument and the laser beam path to the sample (re-drawn from manual)

The laser source provides a coherent beam of light of high intensity which passes through the beam expander which not only increases the laser light beam that gets to it,

but also controls any divergence of it. The resulting collimated parallel beam produced, gets reflected by the beam steering mirror on to the Rayleigh filter which selects the appropriate light wavelength to be sent to the sample for photoexcitation of the molecules/electrons in the sample. The combination of the objective microscope M with the image lens L directly below constitute a telescope to produce the desired magnified image. While the slit in between the two lenses L1 and L2 control the quantity of light allowed to get to the detector, the grating along with the prism efficiently disperse light and select the range of light wavelength needed for the sample analysis [43]. The prism is incorporated because it is best for radiations in the far Ultra violet region and the CCD is the imaging device which converts light signals to electrical signals. The CCD which measures light intensity as a function of wavelength is connected to the computer which then displays the resulting output.

When a sample is exposed to the laser radiation, it interacts with the laser photons and the electrons in the sample are photo excited resulting in the creation of electrons in the conduction band and holes in the valence band with momenta k. When the energy and momentum relax close to the bandgap minimum, the carriers radiatively recombine producing a photon which is then emitted.

The PL instrument used for this research uses the 325 nm line of the Helium-cadmium (He-Cd) laser with a Renishaw RM-2000 spectrometer. The instrument has a Peltier cooled Charge Couple Device (CCD) array for measuring the luminescence spectra of samples and in this case zinc oxide nanoparticles biosynthesized using plant leaf extract.

When the instrument is switched on, it is allowed to warm up and stabilize for about 20 minutes before being used for taking measurements. The internal grating and filter wheel motors were referenced before each measurement session and the spectral wavelength response of the instrument was then calibrated using a reference micro-crystalline diamond sample which produces a clear Raman peak at 1332 $cm^{-1}$ . The laser power on the sample surface can be attenuated using neutral density filters to set positions of 100 %, 50 %, 25 % etc. Special care was taken to avoid any significant local heating due to absorption of the laser beam by the samples. The objective lens

chosen was OFR × 40NUV quartz lens with NA = 0.4 and with a working distance of 2 mm, it was used to produce a spot size of about 1-2 $\mu$m on the sample surface. A 3600 nm grating was used because it is suitable for ultra violet light and is appropriate for light scattered from the sample whose wavelength is low as a result of photo interaction with atomic vibrations within the analysed sample. The sample was placed on a glass slide positioned on an X-Y scanning stage which is adjustable with 1$\mu$m step resolution. The PL technique can be used for studying samples at room temperature as was the case in this research, or at low temperatures for displaying spectral peaks due to impurities in samples. Photoluminescence techniques have also been used in crime laboratories for forensic investigations [41], for the characterization of semiconductors and for determining the electronic band gaps of semiconductors [42]. PL technique can also be used for studying crystal defects like atomic vacancies and substitutions [44] and can also be used for evaluating minority carrier lifetime [45].

## 3.5 Fourier Transform Infrared (FTIR)

A Fourier Transform Infrared instrument comprises an infrared source, an interferometer which consists of a movable mirror and a fixed mirror, a beam splitter, and a detector which is connected to a computer (Figure 3.7). Other components include a square-shaped sample slot S , a pressure gauge knob K which is used to firmly hold down the sample in the slot S. Commands for the working of the instrument are given via the computer and the instrument is controlled by software which uses the fast Fourier Transform to analyse the output of infrared radiation which has passed through or has been reflected from a sample. When light from the infrared source is sent through the interferometer to a sample [46], the sample receives this light which comprises of varied wavelengths or frequencies and absorbs some while others are transmitted through it. The transmitted/reflected radiations get through to the detector which with the help of the Fourier Transform interprets it and the output is displayed on the computer screen as a spectrum which is the variation of the percentage transmittance/reflectance with received radiation frequency and hence wave number. Details of the theory background of this technique are given in sections 2.7-2.8.2 of this

thesis. FTIR technique can be used to study the vibrational infrared absorption [47] or emission spectra of liquids, gases, organic or inorganic solids but in this research, it was used for identifying the functional groups present in the analysed nanoparticles. The FTIR technique is based on the ability of the molecules of a material to absorb light in the infrared region of the electromagnetic spectrum and revealed absorptions usually tally with the molecular bonds present in the sample being analysed. These molecular/chemical bonds as explained in Chapter 2 of this thesis have vibrational and rotational energies and hence characteristic frequencies at which they absorb infrared radiations.

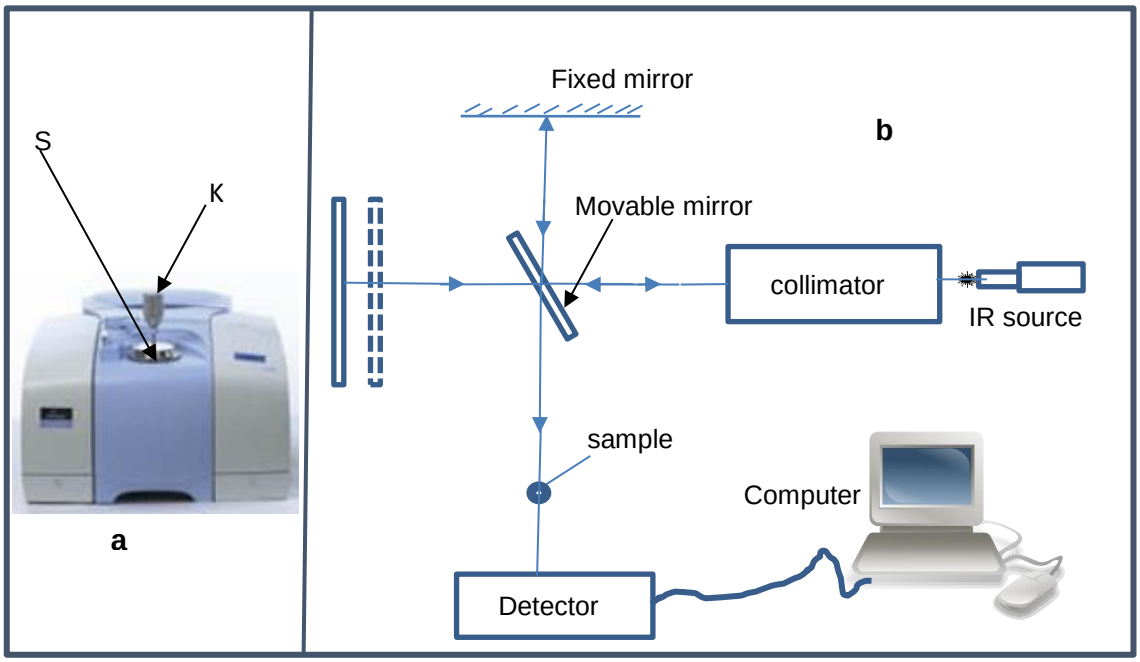


**Figure 3.7** (a) Photograph of Perkin Elmer 100 FTIR Spectrometer from manual (b) Block diagram of spectrometer re-drawn [48].

The produced spectra are then displayed in the monitor connected to the FTIR instrument and by giving commands using the computer mouse, available peaks can be labelled. Fourier Transform Infrared spectroscopy is used by scientists and food industries as well as pharmaceutical companies for analysing their products.

The samples analysed in this work were powdered samples of silver and zinc oxide nanoparticles which were scanned in the wave number range 600 $cm^{-1}$ to 4000 $cm^{-1}$ to display their spectra. The Perkin Elmer Spectrum 100 FTIR spectrometer (Figure 3.7 a) has an attenuated total reflectance (ATR) module and can be used for analysing both solids and liquids.

To analyse a sample, the FTIR machine as well as the computer connected to it were turned on. The sample slot was wiped clean with wipes containing ethanol thereafter a little quantity of the sample was loaded in the sample slot. The range of scan required was selected using the computer and the gauge knob K was gently screwed downwards into the sample to establish good contact between the sample and the diamond crystal (and hence the instrument). While this was being done, the amount of force applied gets displayed on the computer and gauge values between 80 to 100 are deemed appropriate. The command to scan the sample was then given using the computer and the spectrum of the scanned sample was displayed on the computer screen. The command to label the peaks was then given and the peaks which represent those of the functional groups present in the sample were labelled. The labelled peaks were later interpreted using Standard FTIR tables [49,50].

## 3.6 Dynamic Light Scattering (DLS)Technique

A dynamic light scattering (DLS) instrument shown in Figure 3.8 a, is one which can be used for measuring light scattering by particles suspended in a liquid on a microsecond time scale [51]. This instrument can measure sizes of particles within the range 0.3 nm to 10 $\mu$m. The DLS technique relies on the principle that particles which are suspended in a liquid undergo Brownian motion and can disperse or scatter the laser light incident on them to various extends depending on their sizes.

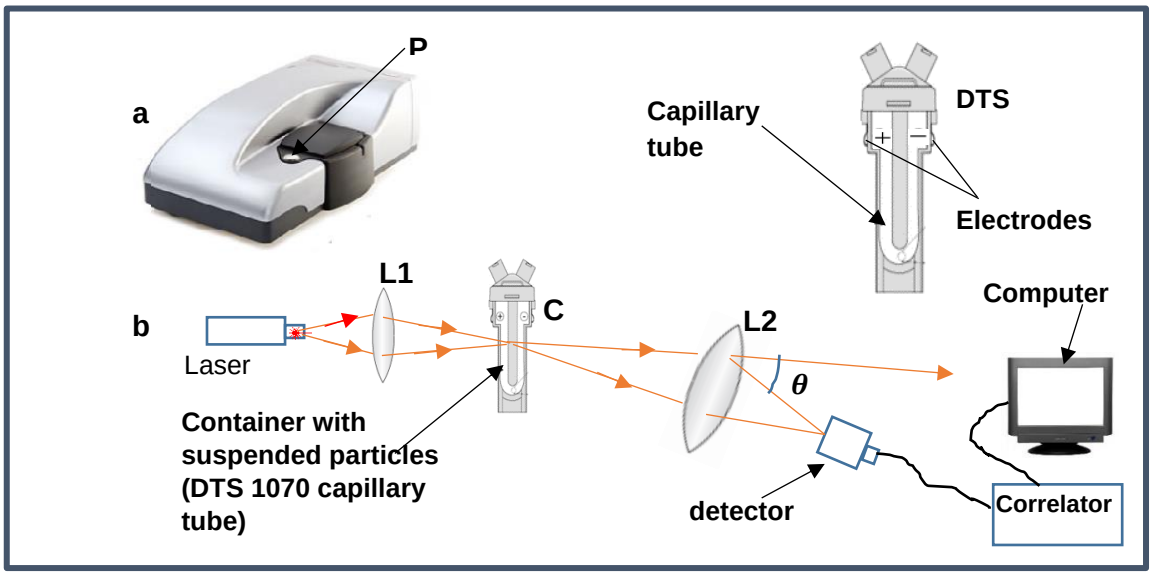


**Figure 3.8** (a) Photograph of Malvern-zetasizer from manual (b) path of light in a DLS instrument as light passes through sample redrawn [52]

Thus, smaller particles undergo faster Brownian motion while larger ones execute slower Brownian motion. Brownian motion of particles in a liquid also depends on the temperature as well as the viscosity of the liquid in which the particles are suspended. The hydrodynamic diameter of a particle suspended in the solution which this instrument measures is given by (Equation 3.6) Stokes-Einstein equation [53] while the translational diffusion coefficient D [54] is given by equation 3.7.

$$d_H = \frac{kT}{3\pi\eta D}, \qquad (3.6)$$

$$D = \frac{kT}{6\pi\eta r} \qquad (3.7)$$

where $d_H$ - hydrodynamic diameter of a sphere assumed to have the same geometry as the particle being analyzed, $k$ - Boltzmann's constant, $T$ - absolute temperature, η -

viscosity and $D$ - diffusion coefficient and r is the hydrodynamic radius of the spherical particle being analysed.

The hydrodynamic radius is the radius of a sphere whose rate of diffusion through the liquid is same as that of our particle of interest. It depends on the surface structure, size, geometry as well as concentration of the ions in the medium containing the particles.

When laser light is shone on a diluted solution containing particles (Figure 3.8 b), most of the incident light get through the sample but some of the light get scattered. Because the dispersed particles in the solution are constantly undergoing Brownian motion, the intensity of light scattered by them changes with time. While smaller particles scatter less light, larger ones scatter more light. The scattered light intensity from all the particles in the solution (or medium) which varies with time will then be sent to the detector and then to the correlator for comparison and the final output gets displayed on the computer screen.

The correlation function [55] G ($\tau$) is given by:

$$G(\tau) = B + A\sum e^{-2q^2D\tau} \qquad (3.8)$$

where $B$ – baseline at infinite time, $A$ - amplitude or intercept, $q$- scattering vector is given by

$q = \frac{4\pi n}{\lambda_0} sin\frac{\theta}{2}$, $n$ - refractive index of dispersant liquid, $\lambda_0$ - laser wavelength, and $\tau$ - correlator delay time.

The correlation function and the form of equation 3.8 will vary depending on the type of particles (large, small or polydisperse) which scatter the laser light that fall on it. The correlation functions and the different onset of decay of the scattered light intensity for small and large particles (T2 and T1) are as shown in Figure 3.9. The graphs show that for small particles, the correlation of the signal decays faster than for larger particles.

The gradient or slope of these exponential decays gives the diffusion coefficient D which can then be used in Equation 3.6 to calculate the hydrodynamic diameter of our particle of interest. Conversely, the function G is proportional to the particle mobility, gives an indication of the diffusion coefficient D in the Stokes-Einstein equation and can be used to determine the hydrodynamic diameter of the particle of interest.

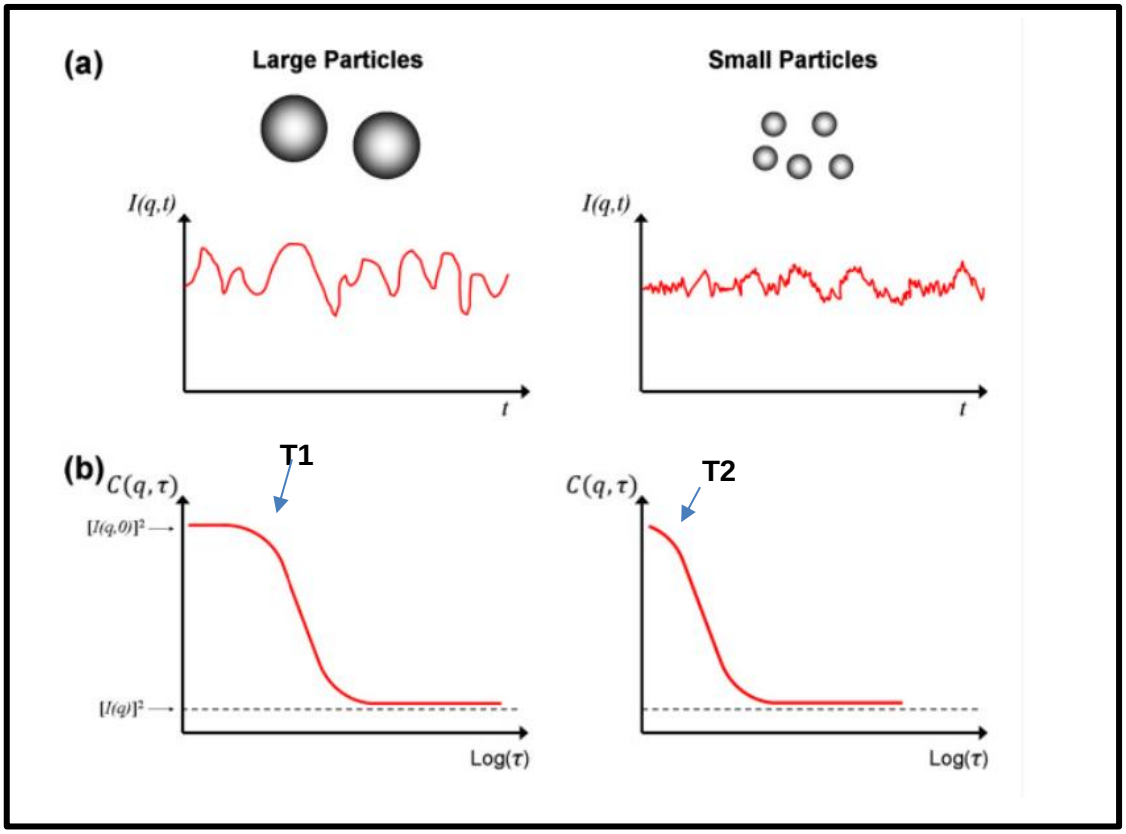


**Figure 3.9** Illustration of scattered light intensity with time as well as the correlation function plots with decay times for large and small particles [56].

This work used the Malvern DLS zetasizer instrument shown in Figure 3.8(a) for analysing silver nanoparticles suspended in aqueous silver nitrate solution. The instrument allows measurements to be done at room temperature and requires only a small volume of sample solution to be introduced into a folded capillary tube (DTS 1070) for analysis. The DLS Malvern zetasizer treats particles as spherically shaped

entities which are homogeneously distributed in the liquid. It gives reliable measurements and allows measurements to be repeated at short time intervals. The DLS technique can be used for determining the molecular weight of materials, the zeta potentials of solutions as well as the size, volume or number distributions of particles suspended in solutions [57].

To start measurements, the instrument had to be switched on and allowed to warm up for about 30 minutes. Thereafter the nanoparticles sample was diluted. About 200 $\mu$l of the silver nanoparticles solution was mixed with 800 $\mu$l of deionized water and a little quantity of this diluted sample was with the help of a syringe introduced into the disposable folded capillary cuvette (DTS 1070) carefully ensuring that no air bubbles were trapped in the cuvette. Thereafter the cuvette was covered with a cap and its body was wiped dry and by pushing the knob P, the sample compartment was opened, and the cuvette was placed in the sample compartment and closed.

With the help of the zetasizer software the type of dispersant used (water) for the sample as well as the refractive index of the material in the sample (Silver) were specified. The temperature at which the measurement was to be done (25 ℃) as well as the equilibration time of 20 seconds were selected. The type of measurement to be done (size distribution) and the number of measurements required per sample (3 replicates) were also specified and thereafter the command to scan the sample was given. The sample got scanned and the results were displayed on the computer screen. The mean and standard deviations of each set of readings were then determined.

## 3.7 X-ray Diffraction (XRD)

X-ray diffraction (XRD) is a non-destructive analytical technique used for phase identification of a crystalline material. An X-ray diffractometer consists of an X-ray source, the sample holder and an X-ray detector [58]. When the filament of the X-ray source is heated, fast moving electrons are produced and these are accelerated towards a target and are energetic enough to dislodge the inner shell electrons of the target material, creating gaps which get filled up by the outer shell electrons resulting in a loss

of energy and a corresponding emission of X-rays and some Bremsstrahlung radiation as well [59]. X-rays can be of the K$\alpha$, and K$\beta$ types depending on what the target material is. Though X-rays can be used for treating tumours and exploring the Cosmos, they can also be used for detecting faults in bones or cracks in metals. In this work, X-rays diffraction was used for studying powdered samples of silver and zinc oxide nanoparticles. The X-ray diffraction (XRD) scans were done on the samples in turn to ascertain their crystal structure. The theory behind this technique has been discussed in section 2.9 of this thesis.

In this work, Cu K$\alpha$ X-rays were used because copper is the target material to which the fast-moving electrons from the filament go. Thus, the BRUKER D8 Advance powder diffractometer with a $Cu\ K\ \alpha$ source and $\lambda = 1.5418$ Å was used. With the slit set at 2 mm for a large beam and a sample rotation speed of 20 rpm, $2\theta$ scans were performed between 25 and 75 degrees and for a 0.02-degree step-size the total scan time was 15hrs. The resulting X-ray patterns show how the intensity of X-rays scattered by the sample varies with the angle $\theta$ and the diffraction peaks indicate the phases in the sample [60]. The peaks produced by each of the samples were compared with a Matching software in the computer which is connected to the X-ray diffraction machine and the peaks and lattice planes were labelled using standard charts as compiled by the Joint committee on Powder Diffraction standards. For the zinc oxide nanoparticles, the JCPDS 06-0644 chart was used and for the silver nanoparticles JCPDS No 04-0783 was used.

## 3.8 Electrodeposition and electrochemical characterization of silver films

### 3.8.1 Electrochemical cell

A three-electrode cell (Figure 3.10) was used because it ensures the control of the environment as well as the potential of the working electrode. In this experiment, the chosen working electrode (WE) was gold thin films evaporated on glass and thermally treated by flame annealing to create the (111) dominant surface orientation [61]. A gold substrate was chosen because of its inert property and because it is known to strongly

interact with silver nanoparticles [62] i.e. have good adhesion. The reference electrode (RE) for silver deposition was silver wire (so-called pseudo reference electrode in equilibrium with $Ag^+$ ions) because Ag /$Ag^+$ has a stable equilibrium potential and is non-polarizable. Platinum wire was chosen as the counter electrode (CE) because it is stable under different conditions and does not interfere with coupled redox systems [63,64].

The silver deposition on the gold substrate was done with de-aeration to minimize the background current from oxygen reduction reaction and minimize any interference with the deposition kinetics. Finally, the electrodeposition was carried out in a Faraday cage to protect the silver solution from light because silver solution is very sensitive to light and $Ag^+$ ions can be reduced by light. The methods used to explore electrodeposition and Ag films included Cyclic Voltammetry (CV), Chronoamperometry (CA) and Linear Sweep Voltammetry (LSV).

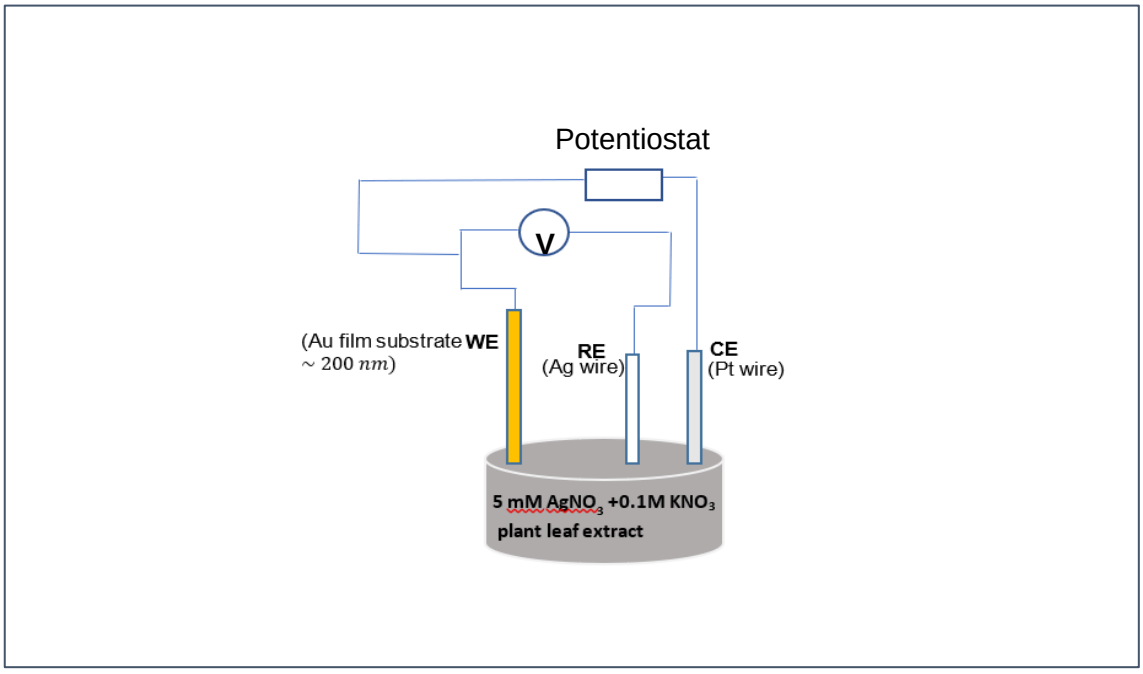


**Figure 3.10** The three-electrode cell used for this research

### 3.8.2 Cyclic Voltammetry (CV)

Cyclic voltammetry is a useful technique for studying the kinetics of an electrochemical reaction which takes place at the electrode surface that is in contact with the electrolyte [65,66]

In this work, cyclic voltammetry (CV) was used to explore the dynamics of silver deposition on Au and to determine any differences in the presence of leaf extracts. Cyclic voltammetry is an electrochemical method often used for studying the kinetics of the electrochemical reactions which occur at the surface of a working electrode. CV technique is generally used for studying ion adsorption, diffusion of ions in the solution, as well as the electrode reactions, such as in this present study. It also enables one to tell if the electrochemical reactions which occur at the electrodes are reversible, or not based on the scan rate dependent changes of the voltammetric (oxidation/reduction) peak [67,68]. The CV technique involves sweeping an electrode potential between two limits $V_1$ and $V_2$ at a constant scan rate. The potential is applied using a potentiostat and as the potential gets to and from the potential $E_{eq}^{0}$, the current which reduces/oxidizes species in the solution is recorded. The potential waveform derivable from this process is as illustrated in Figure 3.11.

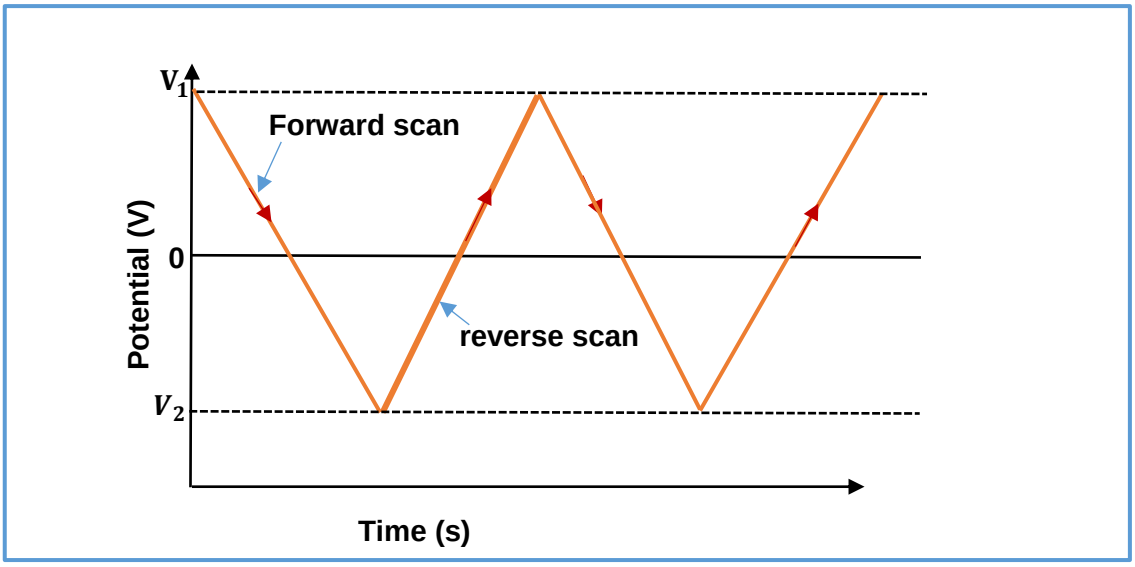


**Figure 3.11** Cyclic voltammetry potential waveform

For the negative potential scan (cathodic scan) which represents the reduction stage (deposition of silver), the potential is swept from a value $V_1$ through $E_{eq}^0$ to a negative value $V_2$. During the reversed scan the potential is increased from that negative value through $E_{eq}^0$ to the starting potential $V_1$. During the reduction process when the potential is cycled negatively, the metal ions in solution (silver in this case) gain electrons from the surface and are deposited on the working electrode (gold) as solid silver $Ag_s^0$. For the oxidation (or dissolution) process, the potential is cycled positively, and the silver gives out an electron (Equation 6.1), gets oxidized and is dissolved from the gold substrate. An anodic current wave is recorded until all Ag is dissolved. The current wave correlated with the thickness of Ag film deposited during negative potential scan is observed. The measured current values versus potential recorded during CV scans are normalized to the surface area of the working electrode and expressed as current density values ($mA/cm^2$). The technique was used to compare the CVs of Ag deposition in the same solution with and without leaf extracts and to determine how they affect the process in terms of current value and the potential at which the processes occur.

### 3.8.3 Chronoamperometry (CA)

During CA, the working electrode (WE) potential is stepped and the current due to the Faradaic processes at the WE as a function of time is obtained. The deposition of Ag films was done at the constant potential using chronoamperometry (CA). CA involved stepping to a constant potential negative from the $E_{eq}^0$ and measuring the current with time. For the process of reduction or oxidation using CA method, ion transport is often controlled by diffusion of ions and the rate of their reduction/oxidation. When a potential is applied, the current value in the diffusion-controlled process decays in accordance with Cottrell equation (Equation 6.2) illustrated in Figure 3.12:

$$i = \frac{nFAc\sqrt{D}}{\sqrt{\pi t}} \qquad (3.9)$$

Where $i$ is current in amperes, n is the number of electrons needed for the reduction/oxidation of the analyte, F is faraday constant $(9.64\times 10^4 \mathrm{C/mole})$, A is the working area of the substrate, c is the analyte concentration, D is the diffusion coefficient in $cm^2s^{-1}$ and t is the time in seconds.

In this work, a double potential step protocol was employed and the deposition at a constant potential was done in the following way. First the electrode was kept at $E_{level\,1} > E^0_{eq} = 0\,V$ (no Ag deposition) for a time $t_1$, then the potential was stepped at $E_{level\,2} < E^{\,0}_{eq}$ for time $t_2$ to get the required deposition.

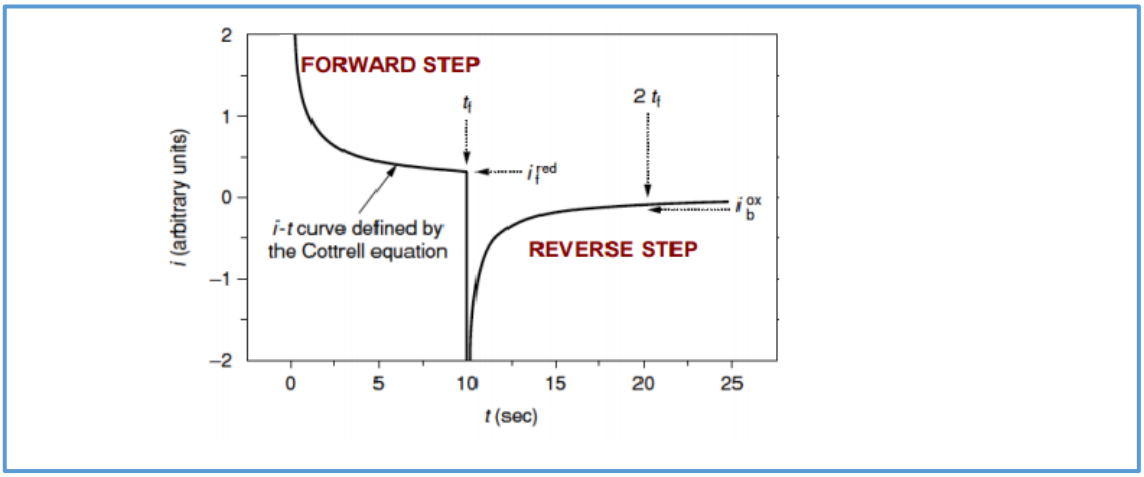


**Figure 3.12** General illustration of current transients for a diffusion-controlled reduction process.

The CA for this work was done from a solution of 5 mM $AgNO_3$ + 0.1 M $KNO_3$ with and without the plant leaf extracts. This was achieved by setting the potential initially at $E_{level\,1} = 0.3$ V for $t_1$= 20 s then stepping to the deposition potential $E_{level\,2}$ for 600 s. The effect of the deposition potential was explored by stepping to the potentials of -0.15 V and – 0.3 V for the same length of time. The charge of deposition, $Q_{dep}$, was then obtained for each potential by integrating the area under the current-time transients. This value was later used for comparison with the charge of dissolved Ag to determine

the efficiency of electrodeposition. Often during deposition process some side reactions can take place and the total current measured during transients cannot be attributed only to the Ag. Therefore, after deposition of silver film, the working electrode (gold substrate) was taken out of the deposition solution, rinsed with ultra-pure water and dried with nitrogen. The deposited Ag films were examined for their structure with AFM or moved to a separate solution (Figure 3.13) for silver dissolution using linear sweep voltammetry.

### 3.8.4 Linear sweep voltammetry (LSV)

A linear sweep voltammogram is a linear potential scan (as in CV, but only in one direction) applied between two potential limits at a constant scan rate to a working electrode. This technique can be used for determining the concentration of a solution or for identifying an unknown species in an electrolyte [69]. In this work however, LSV was used to dissolve silver to be able to estimate the amount of silver which was deposited on the gold substrate. In our work, the LSV dissolution of Ag was done in the separate set up (shown in Figure 6.3) and perchlorate-based solution (1 mM $AgClO_4$ + 0.1 M $HClO_4$) free of any ions that can adsorb on the surface, so the amount of deposited silver could be determined most accurately.

As the voltage is scanned from a value $V_1 = -0.005\,V$ that is very close to the equilibrium of Ag to a more positive potential $V_2 = 0.75\,V > E_{eq}^0$ at the scan rate of 10 mV/s silver dissolution occurred.

## 3.9 Atomic Force Microscope

Atomic Force Microscopy (AFM) is typically used to reveal the surface morphologies of thin films deposited on substrates. It provides information about the nature of the deposited grains and gives an estimate of the surface roughness. Atomic force microscopy can be carried out in different imaging modes namely: the static force mode, the lateral force mode, the dynamic force mode and the phase imaging mode. These different modes have different parameters acting as the setpoint. For instance, in the static force mode, the cantilever deflection is the setpoint, whereas in the dynamic force mode, the cantilever oscillation amplitude provides the feedback parameter.

The most important part of an AFM instrument is the cantilever tip. It is the cantilever tip that interacts with the sample and scans its surface. Atomic Force Microscope imaging can be done using the contact mode, non-contact mode, as well as the tapping and intermittent tapping modes [58]. In the contact mode, the distance between the probe and the sample is less than 0.5 nm. This method is fast, takes care of any forces of friction and is good for rough samples though the application of excessive force might damage the sample. The contact mode consists of the constant height mode and the static force mode. The constant height mode is good for studying atomic scale images due to surface changes at high speed in real time, while in the static force mode mostly preferred, the force on the sample as well as the cantilever deflection are constant. In the non-contact mode, the cantilever tip does not touch the scanned surface, but only oscillates above it exerting small forces on it. The main disadvantage of this method is that it is of lower resolution and the tip oscillations can be affected by surface contamination. In the tapping or dynamic force mode, the cantilever tip touches the sample surface at constant time intervals and because frictional forces do not come in to play, the sample surface is not destroyed. In the intermittent tapping mode, the contact time is a small fraction of the probe's oscillation period and works better for soft surfaces like those of polymers.

AFM images can be analysed to give an estimate of the surface roughness of a thin film. Surface roughness gives a measure of the coarseness of a surface and plays a role in the adhesion [70] of samples to surfaces.

In this research, the Nanosurf Easyscan 2 AFM shown in Figure 3.13 was used for viewing the images of thin films of silver electrochemically deposited on a gold substrate in the presence of plant leaf extracts.

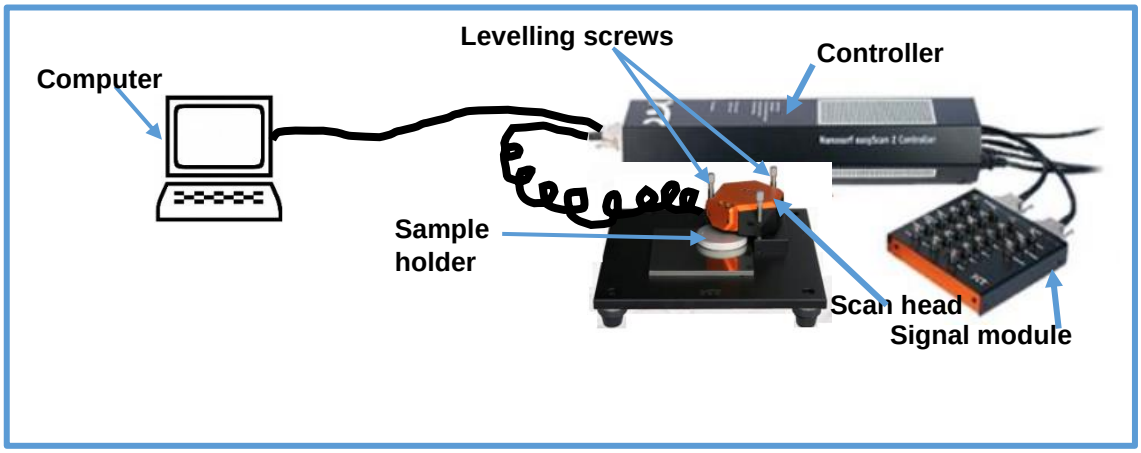


**Figure 3.13** Nanosurf Easyscan 2 AFM (parts assembled from manual) [71]

The sample to be viewed is placed on top of the circular sample holder such that the probe tip (or cantilever) located underneath the scan head was directly above it. The three levelling screws were used in addition to a 'spirit level' to adjust the height of the probe tip. The levelling screws were also used to adjust the height of the cantilever tip from the sample surface till the tip was very close to the sample surface. With the help of the Nanosurf Easyscan software in the computer connected to the device, the mode in which the sample scan will be performed was controlled. For this sample, the dynamic force mode (for which the cantilever or probe tip oscillates at a high frequency close to resonance) was selected. The type of probe tip (NCLR), unit of size measurement ($\mu$m), set point, time per line and points per line were also specified. Furthermore, the current gain and power gain were also selected. The probe tip voltage was set at 1 V and the free vibration amplitude used was 200 mV. With all these parameters chosen, the tip

“Approach” was executed and thereafter the sample surface was scanned either upwards or downwards to display the thin film image on the computer. If the image produced is of good quality, it is saved and analysed later. If, however the image produced is of poor quality, the current gain and power gain values can be adjusted until a good quality image is produced. Sometimes, the sample images produced may contain artefacts such as dragging lines or jumps etc. and if this happens, either a new probe tip will be fixed, or the listed parameters will be adjusted before the imaging process is repeated.

To analyse the images produced from the sample scan, the Gwyddion software was used to determine the surface roughness values as well as the sample grain sizes.

# Chapter 4

# Og and Va plants and finger prints of their leaf extracts

## 4.1 Introduction

The plant leaves chosen for this research were those of *Ocimum gratissimum* (Og) and *Vernonia amygdalina* (Va). Both plants grow well in the tropics and are used for medicinal and culinary purposes [72-74].

### 4.1.1 Ocimum gratissimum (Og)

*Ocimum gratissimum* also known as African basil or clove basil is called Ntoong, Nchanwu or Efirin in Nigeria and belongs to the plant family Lamiaceae. This shrub is common in West Africa and is also popular in India as well as in the Caribbean. Grown mostly to extract oil, Indonesians use its leaves as tea [75]. The plant, an aromatic perennial herb, has been used in folklore medicine for treating headaches, cough, high fever and convulsion, as well as for keeping wound surfaces sterile [72].

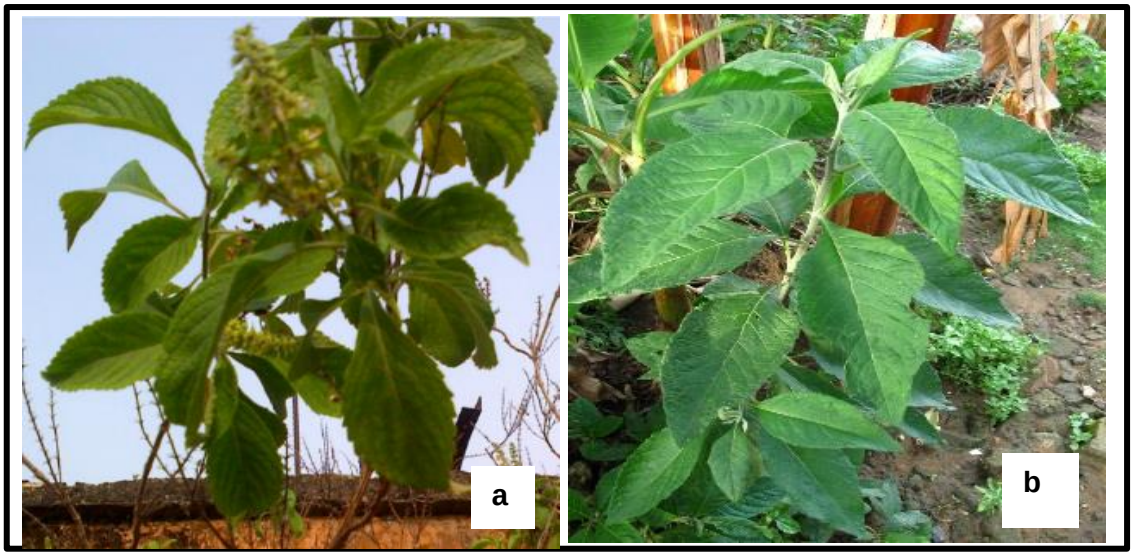


**Figure 4.1** (a) *Ocimum gratissimum* and (b) *Vernonia amygdalina* plants

Some traditional medicine practitioners claim that the oil from its leaves and seeds are very effective in curing upper respiratory tract infection, pneumonia and conjunctivitis [76]. Furthermore, Og flowers and leaves are reported to be rich in oils and can be used for preparing tea, and infusion which traditionalists claim treat stomach upset [72] and its leaves are used as spices in food preparations. Og leaf extract also plays a role in food preservation [77], curtails haemorrhoids and inflammation [76] and can be an antidote to fungal infection and epilepsy [78]. The antibacterial properties of *Ocimum gratissimum* is reported to have been utilised in enhancing the efficacy of antibiotics which could not effectively combat infection because of resistant bacteria [79] and Og leaf extract when mixed with honey is said to have improved antibacterial effect [80].

### 4.1.2 Vernonia amygdalina (Va)

*Vernonia amygdalina* plant on the other hand is a perennial shrub which belongs to the family of plants called Asteraceae. Also known as bitter leaf by most people in Nigeria because of its bitter taste, and as Etidot by the natives of the South-Eastern region of Nigeria, *Vernonia amygdalina* is very popular in Nigeria and is widely eaten and used by the natives in treating many diseases. This plant leaf extract is reported to be effective as an antimalarial and is said to stop hiccups and tackle kidney problems [81,82]. It is also considered an effective laxative [83] and is used for treating bacterial infections [84]. Leaves of *Vernonia amygdalina* serve as fodder for animals and goats are reported to eat it for stomach upsets and amoebic dysentery [83]. It is also reported to be effective in the control of high sugar levels of diabetics [74, 85]. Furthermore, *Vernonia amygdalina* has anti-inflammatory properties [86,87].

While both *Ocimum gratissimum* and *Vernonia amygdalina* leaves are said to be antioxidants [72,88,89], *Vernonia amygdalina* varied uses with good therapeutic abilities offers great promise in alternative medicine for reducing toxicity levels in orthodox medication [90].

Perhaps the vast use of these plants leaf extracts and oils for traditional medicines prompted researchers into carrying out investigations to ascertain their phytochemical constituents for possible scientifically based applications. The outcome of such

investigations formed the starting point for experiments on the uses of plant leaf extracts for the biosynthesis of nanoparticles, which is part of what this present research dealt with.

Aqueous and ethanolic extracts of *Ocimum gratissimum* leaf extract are reported to contain phenols, anthraquinone, alkaloids, tannins, steroids, terpenoids, flavonoids and cardiac glycosides [72], but more than these, ethanolic extract of *Ocimum gratissimum* contains amino acids as well as saponin, and oxalate.

Leaf extract of *Vernonia amygdalina* contains Alkaloids, saponin, terpenes, lignans, flavonoids, phenolic acid, steroids and anthraquinone [91]. Other phytochemical analysis reports show that the Va leaf extract has a high content of steroids, flavonoids, glycosides but a low resin content. Furthermore, it is said to contain some carbohydrate, fatty acids, protein, fibre as well as ash [82]. Aqueous and ethanolic extracts of *Vernonia amygdalina* analysed by the Trease and Evans method show that its aqueous extract contains more flavonoids than its ethanolic extract and it was this information that informed the use of aqueous extracts of the two leaves for this present research. Other phytochemicals found in Va leaf extract are saponin, tannins, alkaloids, steroids and cardiac glycosides [92] however both the ethanolic and aqueous extract contain equal amounts of anthraquinone. Atangwho et al (2009) also report that *Vernonia amygdalina* leaves contain polyphenols, flavonoids and tannins [93].

Erastos et al [89], studied the fatty acid content of Va leaves and reported a high percentage of 74 % which in their opinion was the reason for Va leaf extract effectiveness in the control of diabetes in patients. According to them the fatty acids improve insulin secretion in diabetics [89]. *Ocimum gratissimum* and *Vernonia amygdalina* are said to be antioxidants and this has been confirmed by studies which say that the flavonoids in them thwart the action of free radicals [94,95]. The presence of flavonoids in them also gives them their light screening abilities, antimicrobial, and antibacterial [96] as well as antiviral properties [97,98] and therefore explains their potency in tackling all earlier listed ailments such as diarrhoea, common cold,

pneumonia etc. whose vectors or causative organisms are either bacteria, microbials or viruses.

Plants leaf extracts have also in many available literatures been reported as containing biomolecules said to have reductive abilities. This has severally been ascribed to the presence of flavonoids (in their leaf extract) said to aid the reduction of metallic ions into nanoparticles [99,100].

Classes of flavonoids in plants include Alkaloids, terpenoids and phenolics [101] and in leaves and fruit peels they present themselves as glucosides [102]. These biomolecules are described as water soluble plant metabolites [103] which possess reducing and stabilizing abilities and are therefore effective in nanoparticles biosynthesis [104,105]. The flavonoids and their associated counterparts have the hydroxyl group.

In this present research, silver and zinc oxide nanoparticles were synthesized using the plant leaf extracts of *Ocimum gratissimum* and *Vernonia amygdalina*. These two nanoparticles were characterised using UV-Vis spectrometer, Transmission electron microscope (TEM), Scanning electron microscope (SEM), Dynamic light scattering (DLS) instrument, X-ray diffraction (XRD), Fourier Transform Infrared (FTIR) and in addition Photoluminescence was used for characterising the zinc oxide nanoparticles. The IR spectra of the samples were examined to see if the functional groups associated with these reductive biomolecules are present and as many as was found present were identified and considered as having aided the reduction of the silver ions or zinc oxide into nanoparticles. In this research, these two different plant leaf extracts were used for the biosynthesis of silver and zinc oxide nanoparticles and hopefully the outcome of this work should provide results which will chart a new course for these two plants leaves already known for their food and medicinal usage.

# Chapter 5

# Biosynthesis of nanoparticles

## 5.1 Introduction

Many years of poor environmental and production choices have threatened our planet (Earth) leading to increased calls for efforts aimed at not only addressing the needs of technological progress of mankind but also preserving our ecology. Nanoparticle production has a potential to improve and revolutionise our quality of life and healthcare [106], however, some of their methods of production are not environmentally friendly and these concerns have led researchers into exploring the biosynthesis method and more specifically biosynthesis using plant leaf extracts, which is also a motivation and the subject matter of this present research. Nanoparticles are particles whose sizes are of the order of $10^{-9}$m and are said to show novel properties which differ significantly from those exhibited by their bulk material counterparts. Their extremely small sizes give them high surface to volume ratios that enable them to confine electron movements within boundaries with attendant improved optical properties. This has made them very useful in different fields such as medicine and drug delivery and in electronics. Nanoparticles as sensors have been used for tracing the presence of mercury in domestic water supplies [107,108], and they have even been used in agriculture. It has also been discovered that paints which contain nanoparticles do not lose their colour as fast as conventional paints do [109]. Nanoparticles have been around for many decades because it is now known that natural occurrences such as erosion, volcanic eruptions and forest fires actually generated nanoparticles [110]. Though nanoparticles can be produced through natural means, they can also be produced by chemical methods like vacuum deposition, and vaporisation, gas condensation, chemical precipitation, sol-gel techniques as well as physical methods like mechanical attrition, and more recently using electrodeposition techniques [111]. The production of nanoparticles by physical and chemical methods give many nanoparticles of numerous sizes and shapes which most of the time are unstable and may need stabilizing agents [112]. Nanoparticle

industrial scale production can be expensive, and their usefulness is limited. Furthermore, chemical methods of nanoparticle synthesis produce by-products which are toxic to the environment. The chemical methods are concentration and pH dependent and there is always concern about possible agglomeration hence the need for stabilizers as well as capping agents. In contrast, the biosynthesis of nanoparticles which is now preferred [113] is fast, eco-friendly, cost effective, most of the time a single-step process and gives nanoparticles of diverse sizes and shapes. Biosynthesis of nanoparticles can be done using microorganisms [114] such as algae, yeast, bacteria, plants and parts of plants such as its stem, fruits, root, and leaves and even flowers [115,116]. While these can give nanoparticles of varied shapes and sizes, there are still some shortcomings. For instance, the use of microorganisms for nanoparticle synthesis is slow and presents some constraints such as requiring many hours, instability of nanoparticles and sometimes toxicity [114-118] and in some cases, the process is not a one-step process. If bacteria for example is to be used for nanoparticle synthesis, it must be cultured for many hours before use and because the bacteria grows during the process, its morphology changes and the bacteria can disintegrate before use [114] hence the need for improvement. Recent researches have shifted to the use of plants and specifically their leaf extracts for nanoparticle synthesis. Apart from being fast, this method has the added advantage of minimized toxicity [119,120]. The plant leaf extracts have inherent biomolecules which reduce the metallic ions to nanoparticles, stabilise the nanoparticles and can also cap them discouraging their agglomeration [121]. The biomolecules in plant leaf extracts can by their functional groups modify the surface of the synthesized nanoparticles [122].

The properties of nanoparticles are size and shape dependent, hence the main task for researchers has been to control these. By changing the physical conditions under which the nanoparticles are synthesized or varying the concentration of the precursor materials, nanoparticles of varied sizes and shapes can be produced for diverse application [123]. Most recent approaches for nanoparticle synthesis include wet chemistry techniques and electrodeposition methods like electroless deposition. The targeted use of nanoparticles determines their method of synthesis [124]. While wet

chemistry methods have been used for metal nanoparticle synthesis [124,125], electrochemical deposition techniques have been used for creating nanoparticles of various morphology [126] and for controlling their sizes [127]. Electroless deposition method which deals with deposition and reduction of metallic ions from a solution is also being explored because it can be done even for an electrochemically non-conducting substrate such as textile fibres [128]. Though electroless plating can be an expensive film deposition method and can be unstable depending on the type of electrolyte used or its pH as well as the deposition temperature, it is easy and ensures good hydrogen permeability, as well as thicker and uniform surface coverage [129] of a substrate. This method has also been employed for the deposition of nickel, gold and palladium. It is in view of these recent developments in nanoparticle synthesis techniques that this present research dealt with the biochemical synthesis of silver and zinc oxide nanoparticles and also the electrochemical deposition of silver on gold in the presence of two chosen plant leaf extracts.

Biosynthesized nanoparticles have been used as sensors for studying plasmons of metallic nanoparticles such as silver nanoparticles [107]. Some examples include biosensors enabled to measure the quantity of an intermediate material required for industrial purposes [130] or electrochemical glucose sensor which is proposed could be used for determining glucose levels in diabetics [131]. More applications of biosynthesized nanoparticles include their use for transporting drugs to target cells of the body to perform certain functions like the destruction of cancerous cells and tumour. Biosynthesized nanoparticles have also been used in cosmetics, for catalysis and magnetic resonance imaging (MRI) [132-133] and can be combined with antibiotics to improve their efficacy [133].

In this work, plant leaf extracts were used for the synthesis of two chosen nanoparticles namely silver and zinc oxide nanoparticles. The choice of plants stems from the fact that with plant leaf extracts, reactions can be as fast as five minutes [134]. Plants can act as chemical factories that give stable nanoparticles [119,135] and with plants, bio-reduction can even occur at room temperatures [120]. Furthermore, plant leaf extracts

contain biomolecules like flavonoids, polysaccharides (sugars), terpenoids, polyphenols, alkaloids, and proteins which not only reduce metallic ions to nanoparticles, they protect them (capping) from interaction with their immediate environment thereby reducing toxicity and stabilising the nanoparticles [136]. Many explanations have been put forward to explain how nanoparticles are formed. One of such [136] asserts that flavonoids with their OH group gets changed from the enol-form to the keto-form, giving out a reactive hydrogen atom which reduces the metallic ion into nanoparticles.

Zinc oxide and silver nanoparticles were chosen for this work as stated in the earlier part of this chapter because of their usefulness in the fields of medicine and electronics. They have optical, catalytic, antibacterial, antimicrobial and electrical properties hence their wide range of applications [137].

Silver nanoparticles (AgNPs) are attractive because of their size and shape dependent properties which informs their use in catalysis. They also have good electrical and thermal conductivity so might be beneficial in Nano-circuitry and non-linear optics. They are also useful as antimicrobials [138]. Silver nanoparticles are good light absorbers and dispersers and their surface Plasmon resonance peaks can be tuned. Furthermore, AgNPs have good catalytic, antibacterial and anti-inflammatory properties, are used as healing agents for wounds and in fabrics to control odour [138]. They are also used for bio-imaging.

Zinc oxide (ZnO) nanoparticles on the other hand have antifungal properties and are now being considered for food preservation even by food packaging industries [139]. They (ZnO nanoparticles) have been used for treating skin irritations and other related diseases [137]. They have anti-corrosive properties so are used for surface coatings and are also being incorporated into concrete production. Due to their good optical absorption properties, zinc oxide nanoparticles are used in solar cells, can filter ultra violet radiations and are therefore used in sun screen creams for protecting the human skin. They also serve as filters in rubber and cigarettes [137] [140-142] and more recently are being explored for use as nanofertilizer.

## 5.2 Literature review

Available literature shows that silver nanoparticles synthesized by a titration method at 27 ℃ using fresh leaves extract of Ocimum gratissimum as the titrant in 1 mM $AgNO_3$ solution produced nanoparticles which were reported to be polydisperse and flake-surfaced with diameter 35.9 nm and SPR wavelength 333.2 nm. The produced silver nanoparticles antimicrobial efficacy was tested via a well diffusion method on two bacteria namely Klebsiella and staphylococcus and were reported to be effective [143]. In a related research which dealt with the growth kinetics of Nano silver [144], leaf extract of sundried Ocimum gratissimum leaves was used for the synthesis of Nano silver at 70 ℃ and the resulting Nano silver of size 19 nm was said to have a peak wavelength SPR of 420 nm.

Not much however has been reported on the synthesis of zinc oxide nanoparticles using Ocimum gratissimum. In one synthesis done at 90 ℃ , sun dried Ocimum gratissimum leaf extract was used with $ZnCl_2$ and NaOH as precursor materials and zinc oxide Nano rods and Nano flowers of hexagonal crystal structure with sizes 348 nm and 960 nm respectively and with diameters 54 nm and 87 nm respectively were produced [145,146].

In this present research, the two chosen nanoparticles: silver nanoparticles and zinc oxide (ZnO) nanoparticles were synthesized using two plant leaf extracts namely *Ocimum gratissimum* (Og) and *Vernonia amygdalina* (Va) leaf extracts. The Og/Va leaf extracts were prepared using shade-dried leaves. The silver nanoparticles were biochemically synthesized using aqueous silver nitrate of concentrations 2 mM – 5 mM. In chapter 6 of this dissertation, a description of the making of thin films of silver in the presence of each of the chosen plant leaf extracts is given and the surface coverage abilities of the 5 mM aqueous silver nitrate (used as the electrolyte) with each of the plant leaf extracts was explored. In chapter 7 of this write up, zinc oxide nanoparticles were synthesized at pH 8, 10 and 12 using each of these two leaf extracts with precursor materials zinc acetate dihydrate ($Zn(CH_3COO)_2.2H_2O$) and sodium hydroxide pellets

(NaOH). The produced ZnO nanoparticles were characterized using optical spectroscopy and electron microscopy and their (zinc oxide nanoparticles) efficacy as a possible Nano fertilizer was also explored.

The following were the objectives of this research:

i. Prepare shade dried leaves of the two plants chosen and prepare their leaf extracts.
ii. Synthesize the silver and zinc oxide nanoparticles using the prepared leaf extracts at specified temperatures.
iii. Characterise them using UV-vis, TEM, SEM, XRD, FTIR, DLS
iv. Identify their shapes and sizes
v. Explore some possible applications of the synthesized Nano particles.

It is hoped that this research will chart a new course for the two plants rather than their present use for food and medicine. This work will also add to already existing knowledge on biosynthesized metallic/metal oxide nanoparticles.

## 5.3 Experiments

### 5.3.1 Chemicals and materials

All the chemicals were purchased from Sigma Aldrich and are of analytical grade and milli-Q water was used for preparing all the solutions.

Zinc acetate dihydrate ($Zn(CH_3COO)_2.2H_2O$) of Molecular weight 219.50, and Purity $>$ 99 and Silver Nitrate ($AgNO_3$) of Molecular weight 169.88 and Purity $>$ 99 % as well were used.

Sodium hydroxide pellets (NaOH) of Molecular weight 40g were also used.

*Ocimum gratissimum* (Og) and *Vernonia amygdalina* (Va) shade - dried leaves (leaves dried in a shade away from direct sunlight) were used for preparing the needed leaf extracts.

### 5.3.2 Preparation of Chemicals

Zinc acetate solution (0.2 M) was prepared using 43.9 g of the salt in 1000 $cm^3$ of milli-Q water.

Aqueous solution of $AgNO_3$ (5 mM) was also prepared by dissolving 0.849 g of the salt in 1000$cm^3$ of milli-Q water and by serial dilution other concentrations of the silver nitrate solution were derived. Thus for 100 ml of each of 4 mM, 3 mM, 2 mM concentrations, 80ml, 60 ml and 40 ml respectively of the 5 mM $AgNO_3$ was used and the solution in each case was made up to the required 100 ml.

Two solutions of sodium hydroxide were also prepared:

The 2 M of NaOH solution was done by dissolving 40 g of the pellets in 500 $cm^3$ of water while the 0.2 M of NaOH solution was prepared by dissolving 8 g of the pellets in 1000 $cm^3$ of water.

### 5.3.3 Preparation of plant leaf extracts

To prepare 100 ml of Og or Va leaf extract, 130 ml of water was added to 15 grams of each of the ground shade dried Ocimum gratissimum or Vernonia amygdalina leaves (Figure 1) and the mixture was boiled for one hour. Thereafter the leaf extract was filtered and stored in a refrigerator for use.

**Figure 5.1** Ground shade - dried Og leaves

## 5.4 Synthesis of nanoparticles

### 5.4.1 Zinc oxide nanoparticles synthesis

Zinc oxide nanoparticles were synthesized at three different pH values. By mixing equal volumes of 0.2 M zinc acetate dihydrate solution and 0.2 M sodium hydroxide with 30 ml of the Og or Va leaf extracts and while stirring the mixture, 2 M NaOH solution was added dropwise to adjust the pH of the mixture (monitored using a pH meter) to pH 8, 10 or 12 as required. This mixture was stirred continuously for 2hrs resulting in a cloudy precipitate of zinc hydroxide ($Zn(OH)_2$) which was then centrifuged at 5000 rpm for 60 minutes and dried in an oven set to 70 ℃. The equations (5.1-5.3) of the reactions which take place [147,148] are as follows:

Aqueous zinc acetate reacts with the NaOH to give the zinc hydroxide $Zn(OH)_2$ :

$$Zn\ (CH_3COO)_2.2H_2O + 2NaOH \rightarrow Zn(OH)_2 + CH_3COONa + 2H_2O \quad (5.1)$$

The zinc hydroxide $Zn(OH)_2$ reacts with water to give the growth unit $Zn(OH)_4^{2-}$ and hydrogen ions:

$$Zn(OH)_2 + 2H_2O \rightarrow Zn(OH)_4^{2-} + 2H^+ \quad (5.2)$$

When centrifuged, $Zn(OH)_4^{2-}$ changes to ZnO:

$$Zn(OH)_4^{2-} \rightarrow ZnO + H_2O + 2OH^- \quad (5.3)$$

The Block diagram for the synthesis of the ZnO nanoparticles and the resulting powder is as shown in Figure 5.2.

The ZnO nanoparticles were characterised using UV-vis to get their absorbance as well as the diffuse reflectance spectra in order to determine their Energy band gap ($E_g$).

The optical energy band gap $E_g$ of the nanoparticles can be determined using the diffuse reflectance values *R* from the Kubelka-Munk function given as [39]:

$$F(R) = \frac{(1-R)^2}{2R} \qquad (5.4)$$

and the Tauc relation given as

$$(h\upsilon\alpha)^{\frac{1}{n}} = A\left(h\upsilon - E_g\right) \qquad (5.5)$$

where $E = \frac{1240}{\lambda}$ in electron volts, λ is in nm, h is a Planck constant, $\upsilon$ is the frequency of the light (Hz) shone on the sample, α = $F(R)$ and $n = \frac{1}{2}$ for zinc oxide [39] which is a direct band gap semiconductor.

The Tauc plot which is a graph of $(F(R)E)^2$ against energy $(eV)$ was done and a linear fit made to the region of maximum change will give the energy band gap of the ZnO nanoparticles.

While an XRD scan was done to determine the crystal structure of the nanoparticles, a FTIR scan was done to identify the functional groups in the plant leaf extracts which aided the reduction that produced the ZnO nanoparticles. SEM images were taken to see the shapes and sizes of the synthesized nanoparticles as well as note how the structures of the ZnO nanoparticles changed with its pH of synthesis.

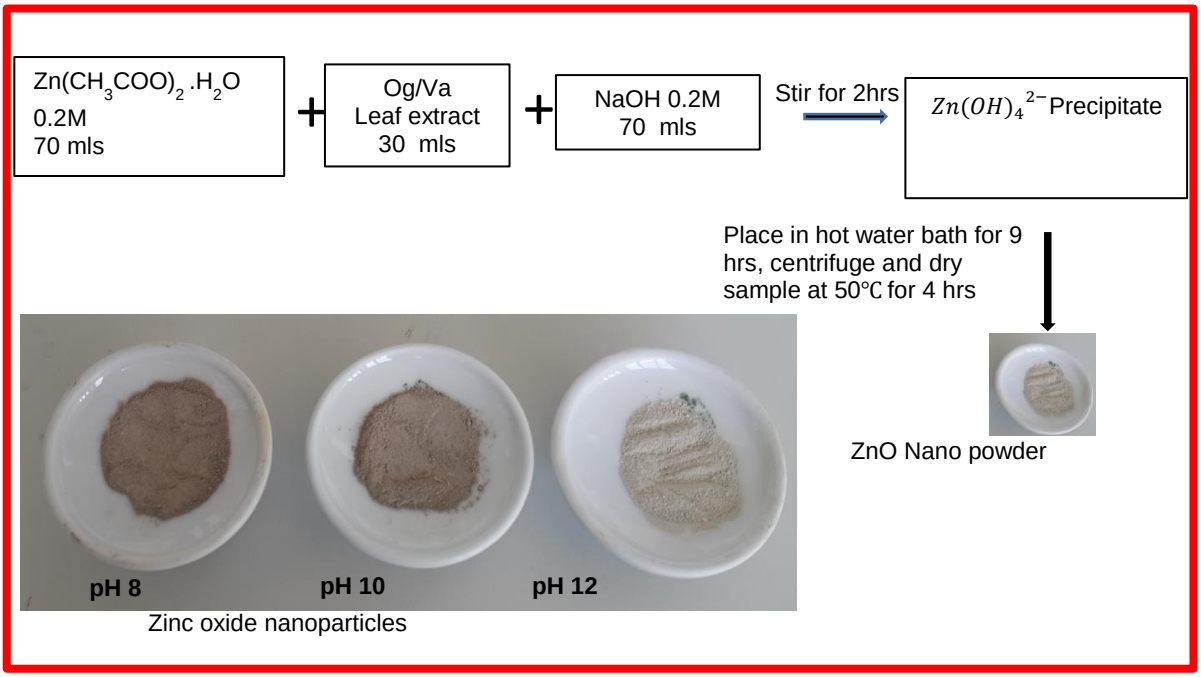


**Figure 5.2** Schematic illustration of zinc oxide synthesis pathway.

### 5.4.2 Silver nanoparticles synthesis

Aqueous silver nitrate solution of concentration 2 mM to 5 mM was used for the synthesis. 90 ml of each concentration of the silver nitrate was mixed with 10 ml of each leaf extract and the mixture was placed in a water bath set to 30 ℃ for some hours. From available literature, the silver nanoparticles are formed when the phenolic compounds or flavonoids (contained in plant leaf extracts) which have antioxidant properties donate electrons to the silver metallic ions [149,150] and reduce them into nanoparticles. Aqueous silver nitrate dissociates as shown in Equation 5.6.

$$AgNO_3 \rightleftarrows Ag^+ + NO_3^- \qquad (5.6)$$

These antioxidants have the hydroxyl group (OH) which combine with the cation $Ag^+$to form hydroxyl complexes that get supersaturated resulting in crystallite growth and

therefore the production of nanoparticles. A change in the colour of the solution (aqueous $AgNO_3$ + plant leaf extract) to a reddish-brown colour indicates the formation of the silver nanoparticles. Figure 5.3 illustrates the biosynthesis process. The optical absorbance spectrum of the nanoparticles was run after 6 hrs, 12 hrs, 24 hrs and 48 hrs. The silver nanoparticles were also characterised with the Fourier Transform infrared (FTIR), Transmission electron microscope (TEM), X-ray diffraction (XRD), and the Dynamic Light Scattering (DLS) techniques.

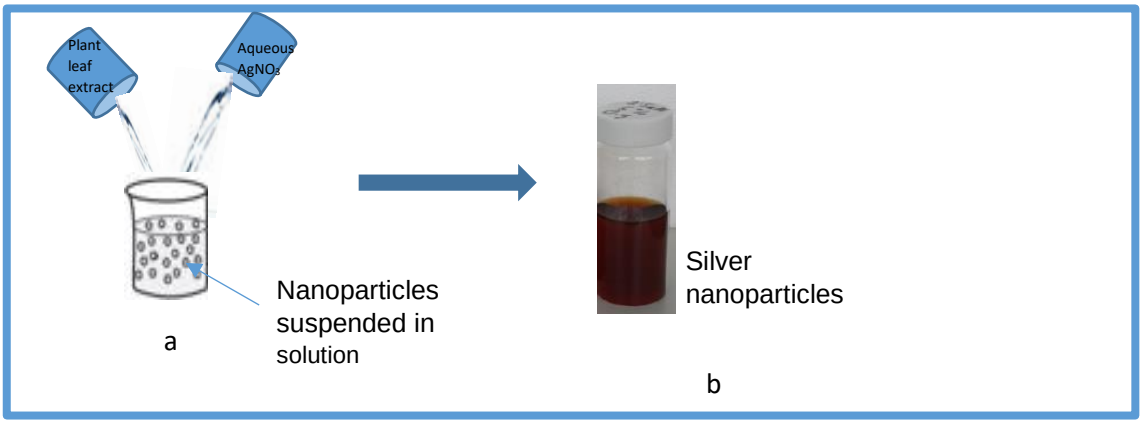


**Figure 5.3** (a) Silver nanoparticles synthesis (b) sample of prepared AgNPs

## 5.5 Results and Discussion

The zinc oxide Nano powder absorbance spectrum (Figure 5.4) shows that the Og ZnO nanoparticles have a higher peak absorbance at wavelength 355 nm than the Va ZnO nanoparticles peak absorbance which was at wavelength 360 nm. These observed values are less than that of bulk zinc oxide given as 380 nm [151] and show a blue shift in excitonic absorption which indicates a small quantum confinement effect [152]. The intensity of the absorbance for the Og zinc oxide nanoparticles increased with pH levels but decreased with increased pH for the Va zinc oxide nanoparticles.

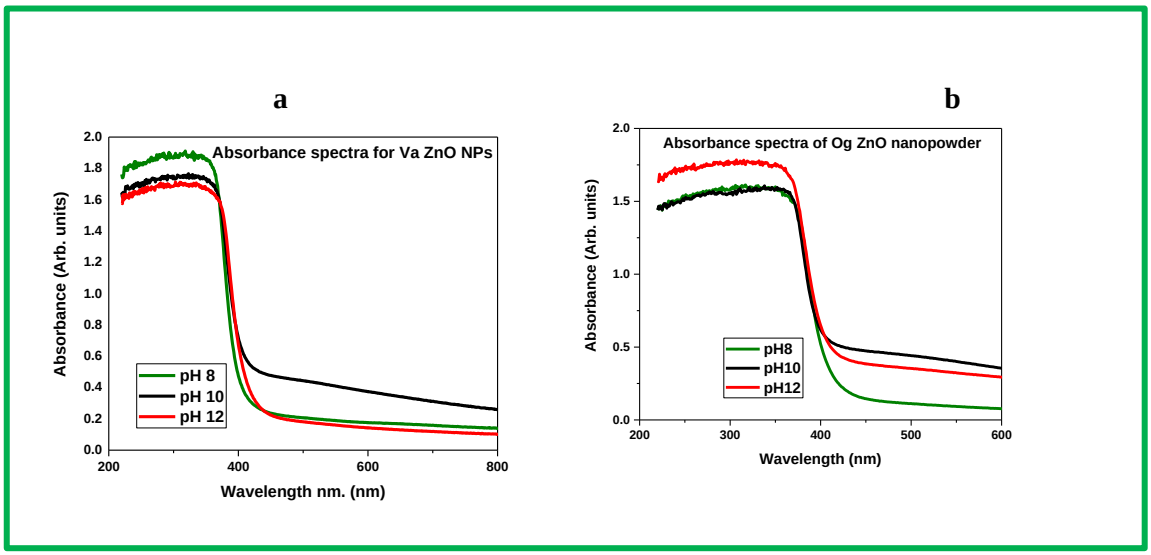


**Figure 5.4a** UV-vis spectrum of the synthesized ZnO nanoparticles

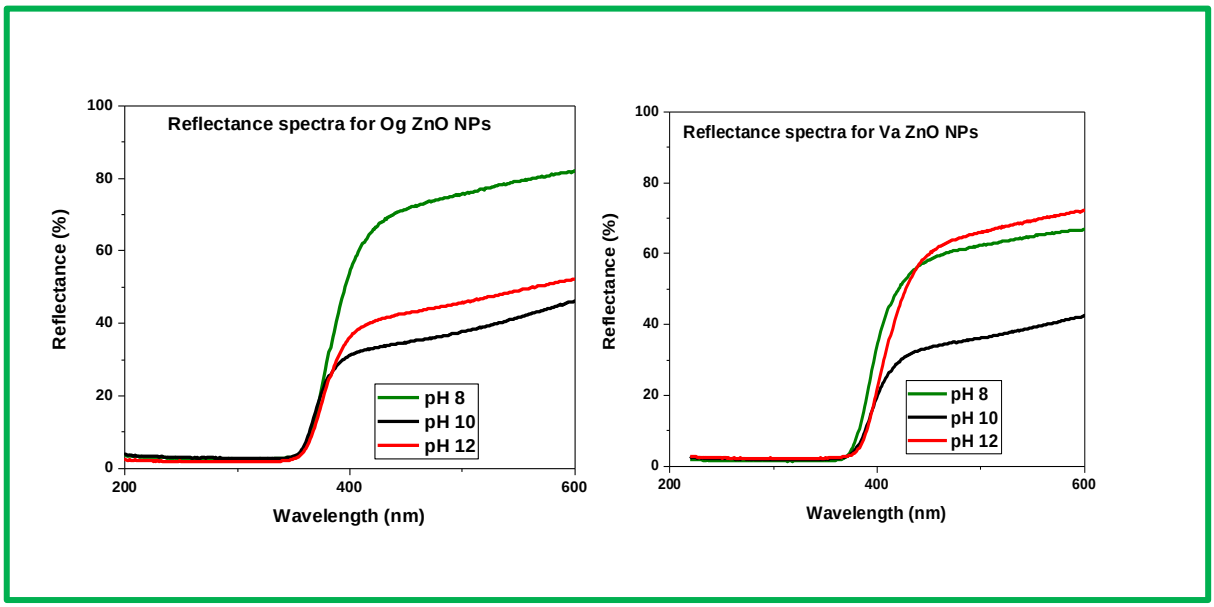


**Figure 5.4b** Reflectance spectrum of the synthesized ZnO nanoparticles

For both the Og and Va zinc oxide nanoparticles, the nanoparticles sizes increased when the pH of their synthesis was raised and agrees with Koao [153] that reported a similar trend and ascribed the observation to the dissolution of zinc hydroxide when the pH of synthesis increases. While for the Og zinc oxide nanoparticles an increase in synthesis pH produced larger nanoparticles and higher $E_g$ values, for the Va zinc oxide nanoparticles, though the nanoparticles sizes increased with pH increase, its $E_g$ values reduced with increased synthesis pH (Figures 5.5a and 5.5b). The observed trend agrees with that reported by Alias et al [154], Heo et al [155] as well as Debanath et al [156] and Pholnak et al [157] who observed size dependent $E_g$ values for their ZnO nanoparticles made using wet chemistry method. A summary of the obtained values of sizes and $E_g$ values for different synthesis pH in this present research is given in Table 5.1.

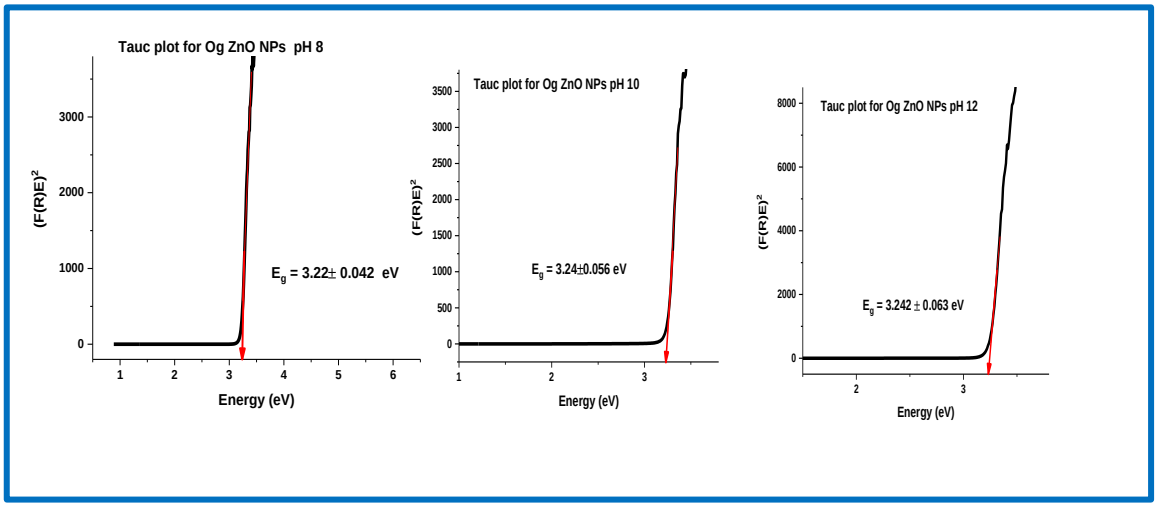


**Figure 5.5a** Tauc plot of the Og pH 8, 10 and 12 ZnO nanoparticles showing their determined energy band gap values.

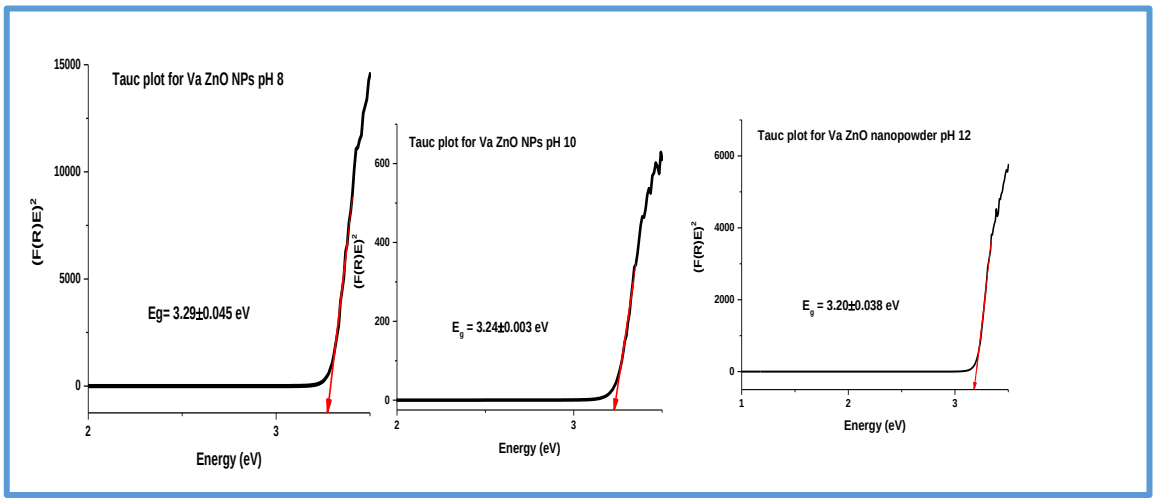


**Figure 5.5 b** Tauc plot of the Va pH 8, 10 and 12 ZnO nanoparticles showing their determined energy band gap values

**Table 5.1** Showing the sizes and optical energy band gap( $E_g$) of Og and Va zinc oxide nanoparticles (ZnO Nps) synthesized at various pH values.

| pH of synthesis of ZnO Nps | Og ZnO nanoparticles | | Va ZnO nanoparticles | |
|---|---|---|---|---|
| | Size of Nps (nm) | $E_g$ of Nps (eV) | Size of Nps (nm) | $E_g$ of Nps (eV) |
| pH 8 | 38 ±0.4 | 3.220±0.042 | 44 ±0.8 | 3.290±0.045 |
| pH 10 | 43 ± 0.6 | 3.240±0.056 | 57±0.5 | 3.240±0.003 |
| pH 12 | 63± 0.8 | 3.242±0.063 | 62±0.6 | 3.200±0.038 |

The X-ray diffraction (XRD) scan was done with a powder diffractometer with Cu Kα X-ray with λ= 0.154 nm. With the start and end set at 2$\theta$ values of 25 ° and 75 ° respectively and a step size of 0.02, the sample scan was done for 15 hrs and showed high intensity peaks with no unusual peaks (Figure 5.7 a) indicative of good crystalline structure for a typical hexagonal wurtzite structure of ZnO according to JCPDS (2000)36-1451, with the plane 101 showing the strongest reflection.

FTIR spectra of the synthesized nanoparticles was done using Perkin Elmer spectrum 100 FTIR spectrometer and scans of the samples were done in the range 600 $cm^{-1}$ - 4000$cm^{-1}$. The scan results of the ZnO nanoparticles showed that the Og ZnO nanoparticles peaks were sharper than those of the Va ZnO nanoparticles (Figure 5.7 b). The O-H bend at 1429.68 $cm^{-1}$ and the O-H stretch peak at 3312.03 $cm^{-1}$ denote the presence of phenols and flavonoids. Other functional groups identified on the nanoparticles surface were the N-H bend due to amines at 1572.43 $cm^{-1}$, the O-H stretch at 2980.49 $cm^{-1}$ for carboxylic acid and some polysaccharides.

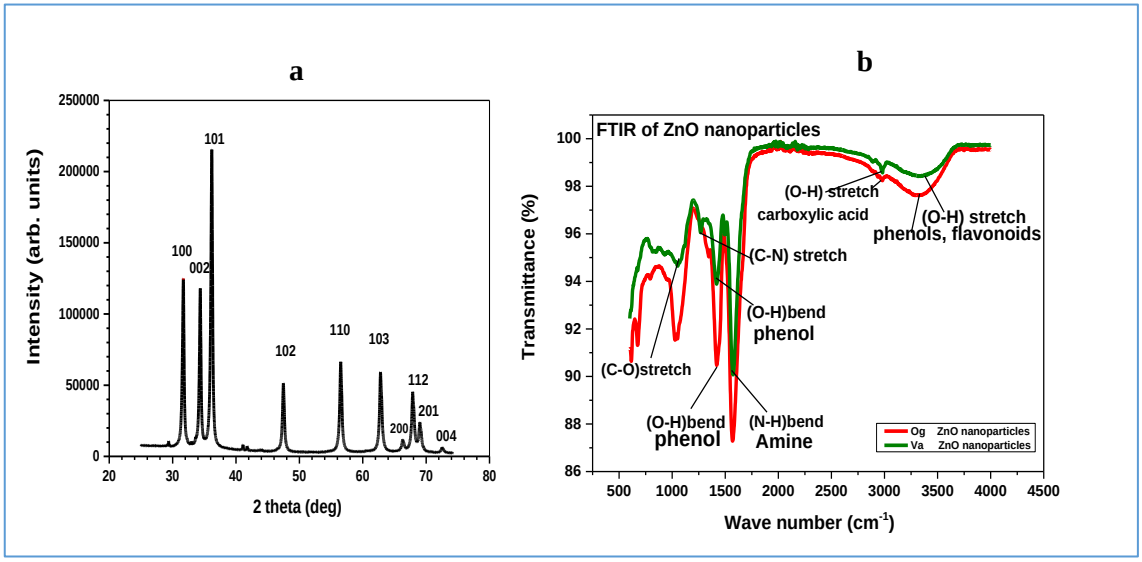


**Figure 5.6 (a)** XRD pattern **(b)** FTIR scan results of the ZnO nanoparticles

The photoluminescence spectra of the zinc oxide nanoparticles (Figure 5.8) show transmission spectra with two emission bands namely a higher wavelength peak (Energy 2.2 eV) due to singly ionized oxygen vacancies and a lower wavelength peak (Energy 3.2 eV) due to the near bandgap excitonic emission [158]. The UV emission observed to be less than 400 nm and usually described as band edge emission is due to a recombination of free excitons when they collide with themselves [159]. The green emissions with wavelengths above 500 nm could be due to some defect states [160] in the sample. Furthermore, the spectral intensities of both the Og and Va zinc oxide nanoparticles shown in Figure 5.7 were found to decrease with increased pH. The UV and green emissions for the pH 8 Og zinc oxide nanoparticles were at 2.3 eV and 3.22 eV, for the pH 10 it was at 2.35 eV and 3.24 eV and for the pH 12 it was at 2.25 eV and 3.22 eV. The values of the UV and green emissions were at 2.22 eV and 3.20 eV for the pH 8 Va zinc oxide nanoparticles, at 2.22 eV and 3.20 eV for the pH 10 ZnO nanoparticles and the peaks at 2.22 eV and 3.15 eV were for the pH12 ZnO nanoparticles.

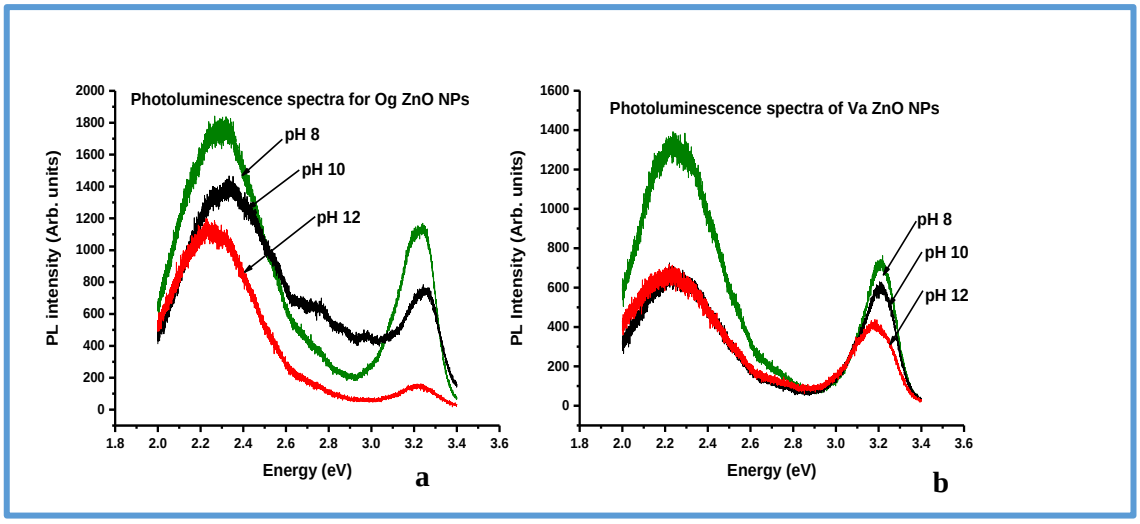


**Figure 5.7 (a)** Photoluminescence spectra for (a) Og and (b) Va ZnO nanoparticles

The SEM images (Figures 5.8 - 5.9) show that the zinc oxide nanoparticles synthesized at all the three chosen pH values were spherical in shape and in clusters, a feature Ikono et al report signifies that the ZnO nanoparticles were pure [161].

The low pH Og zinc oxide particles were found to be smaller in size than higher pH nanoparticles. Thus, for the Og zinc oxide nanoparticles sizes were found to increase in the order pH12 > pH10 > pH 8. The mean size of the Og pH 12 zinc oxide nanoparticles was 63 ± 0.8 nm, the pH 10 nanoparticles had a mean size of 43±0.6 nm and the pH 8 nanoparticles had a mean size of 38 ± 0.4 nm. Conversely, the Va zinc oxide nanoparticles made from a pH 8 solution had an average size of 44 ± 0.8 nm, those made at pH 10 had an average size of 57 ± 0.5 nm and the nanoparticles synthesized at pH 12 had an average size of 62 ± 0.6 nm.

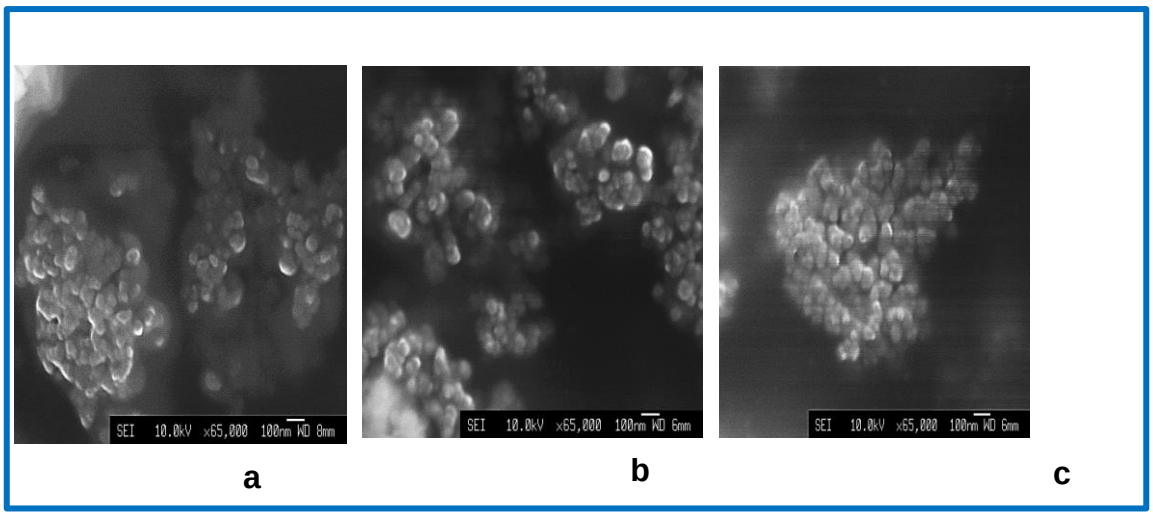


**Figure 5.8** SEM images of (a) pH 8 (b) pH 10, (c) pH 12 Og zinc oxide nanoparticles

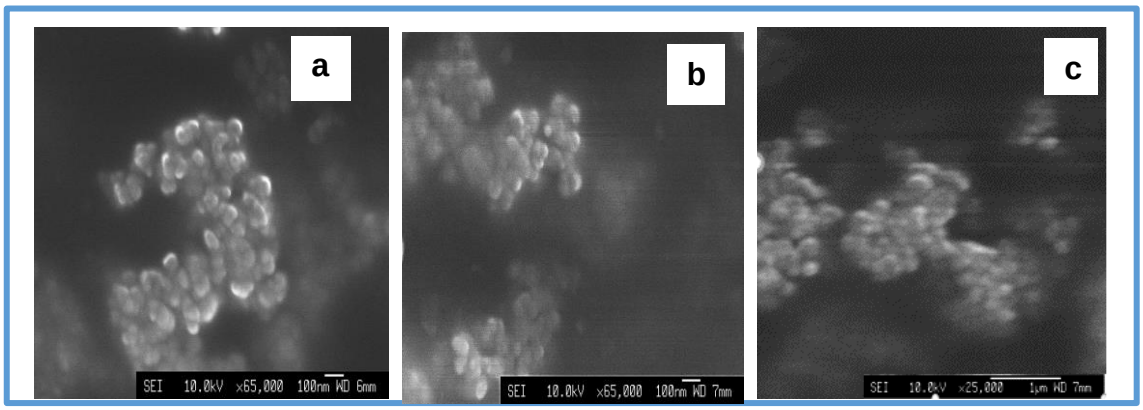


**Figure 5.9** SEM images of (a) pH 8 (b) pH 10, (c) pH 12 Va zinc oxide nanoparticles

The UV-Vis absorbance spectrum of the silver nanoparticles increased with the concentration of the aqueous $AgNO_3$ used and depended on the type of plant leaf extract used. (Figure 5.10) The surface plasmon resonance absorbance peak also increased with the concentration of the aqueous silver nitrate solution and the type of plant leaf extract used. The SPR peak wavelength ($\lambda_{peak}$) for Og silver nanoparticles was found to be 440 nm while that of the Va silver nanoparticles 437 nm. While the peak absorbance for the Og silver nanoparticles increased steadily with time up to 48 hrs and beyond, the Va silver nanoparticles peak absorbance after 48 hrs was found to have dropped drastically with a slight shift of the plasmon resonance peak. (Figure 5.10) This was attributed to some aggregation of the nanoparticles to produce larger ones.

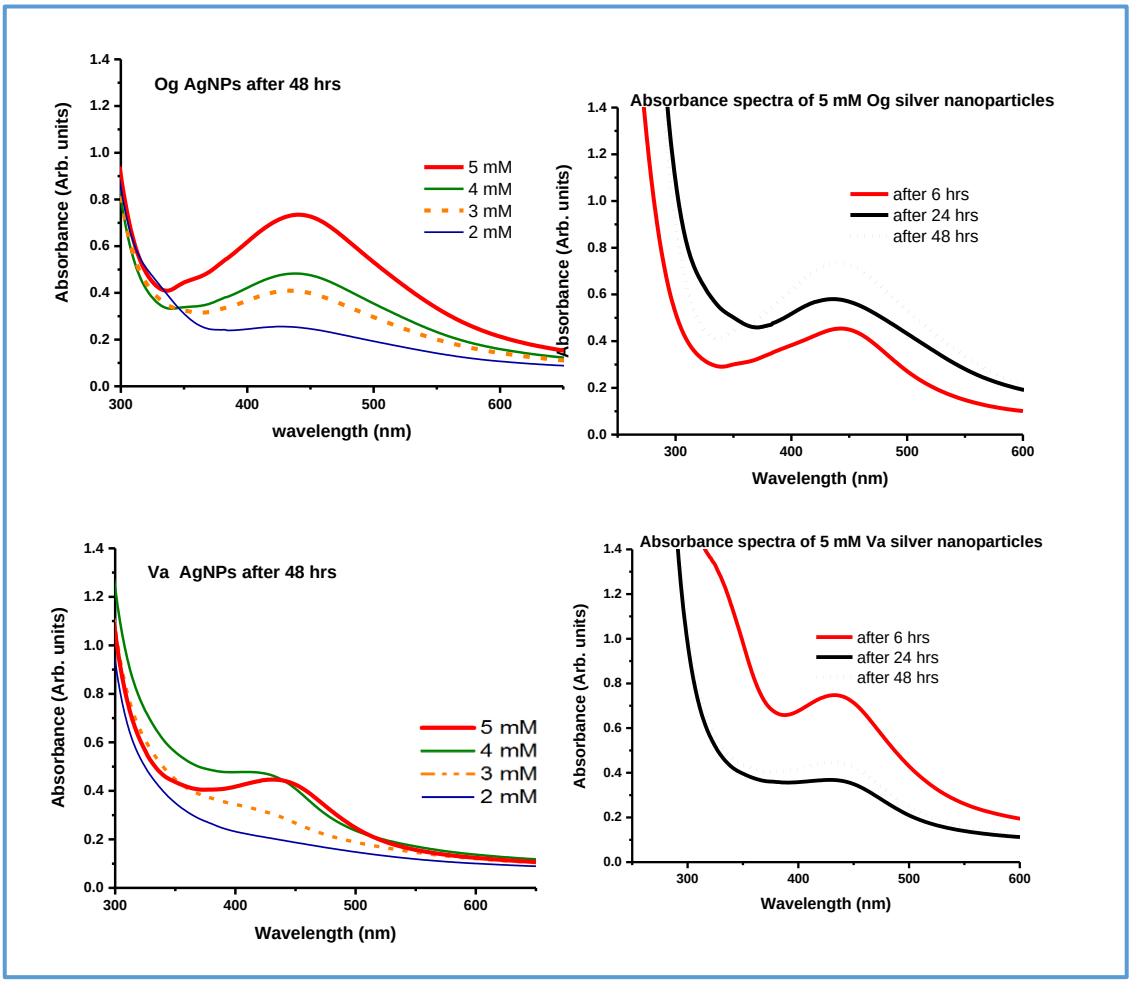


**Figure 5.10** Time dependent UV-Vis absorbance spectrum for different concentrations of the Og and Va silver nanoparticles.

The TEM images (Figures 5.11 and 5.12) of two concentrations only (2 mM and 5 mM) of both the Og and Va silver nanoparticles were analysed. The average size of the 2 mM Og silver nanoparticle was 20 $\pm$ 0.8 nm while that of the 5 mM silver nanoparticles was 68 $\pm$0.5 nm. Similarly, the 2 mM Va silver nanoparticles were of average size 18 $\pm$ 0.6 nm and the 5 mM 59 $\pm$0.7 nm. The FTIR scan of the silver nanoparticles (Figure 5.13) were done in the range 600 $cm^{-1}$ – 4000 $cm^{-1}$ and gave the identities of the functional groups present on the surface of the nanoparticles to contain the hydroxyl group (O-H) with a broad peak at 3315.89 $cm^{-1}$ for flavonoids and phenols, the C-H stretch for carboxylic acid and alcohol (alkane) and some reducing sugars also. These

biomolecules may have been responsible for the reduction of the silver ions in solution to nanoparticles.

The XRD peaks obtained are as shown in Figure 5.14. Five distinct peaks were identified though there were other un- identified peaks. The strongest peak was for the 311 plane and the synthesized silver nanoparticles were found to have the FCC crystal structure.

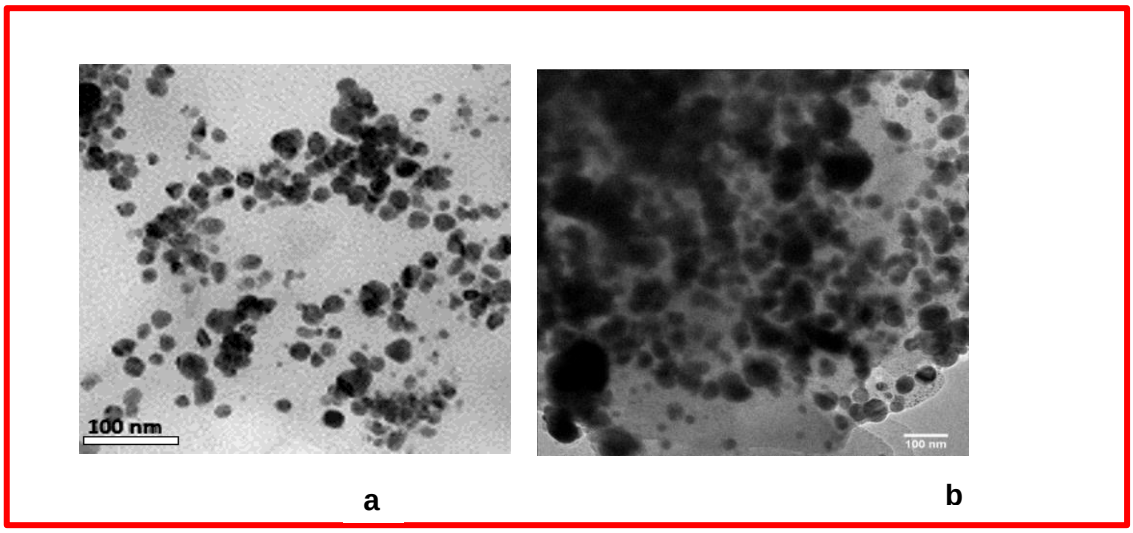


**Figure 5.11** TEM images of Og silver nanoparticles of concentrations (a) 2 mM and (b) 5 mM

In this research, the surface coverage abilities of the silver nanoparticles were explored in chapter 6 while in chapter 7, colloidal solution of the ZnO nanoparticles were used as nanofertilizer to grow Amaranthus cruentus because it has been reported that ZnO nanoparticles could be useful for agriculture [162].

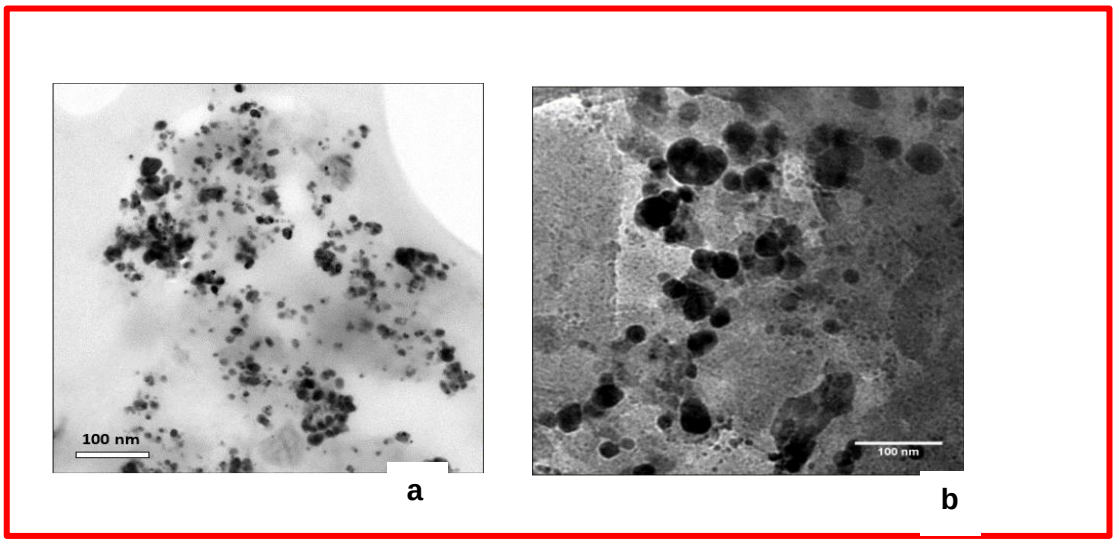


**Figure 5.12** TEM images of Va silver nanoparticles of concentrations (a) 2 mM and (b) 5 mM

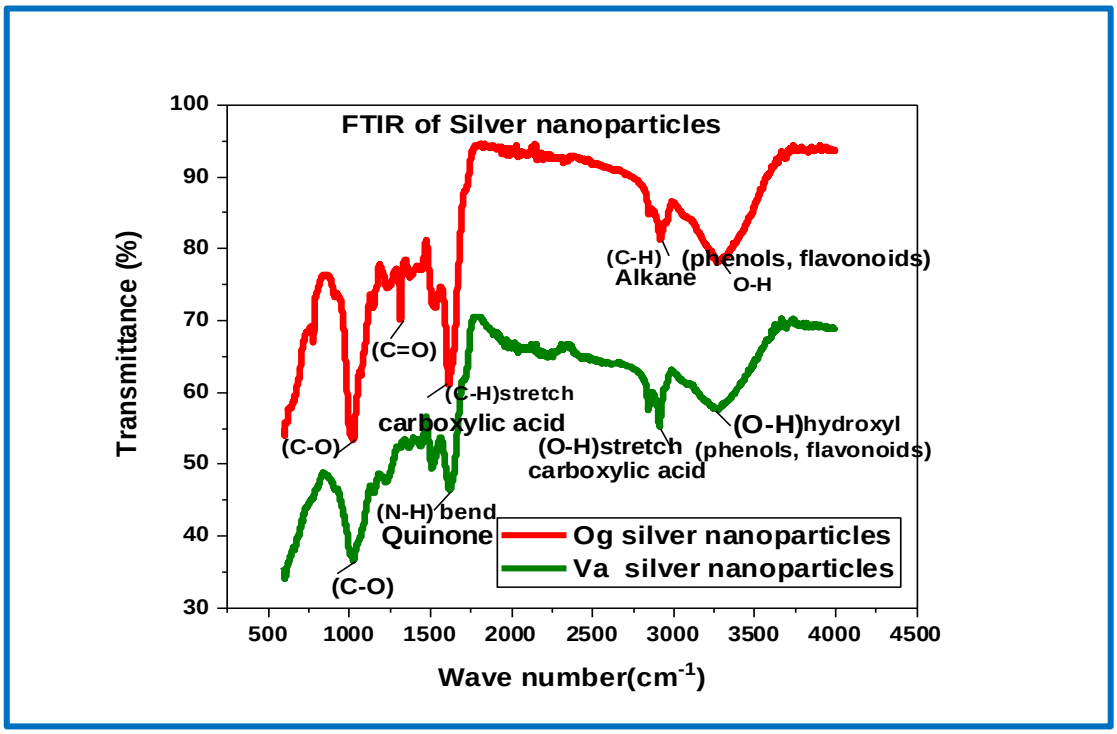


**Figure 5.13** FTIR scan results of the silver nanoparticles

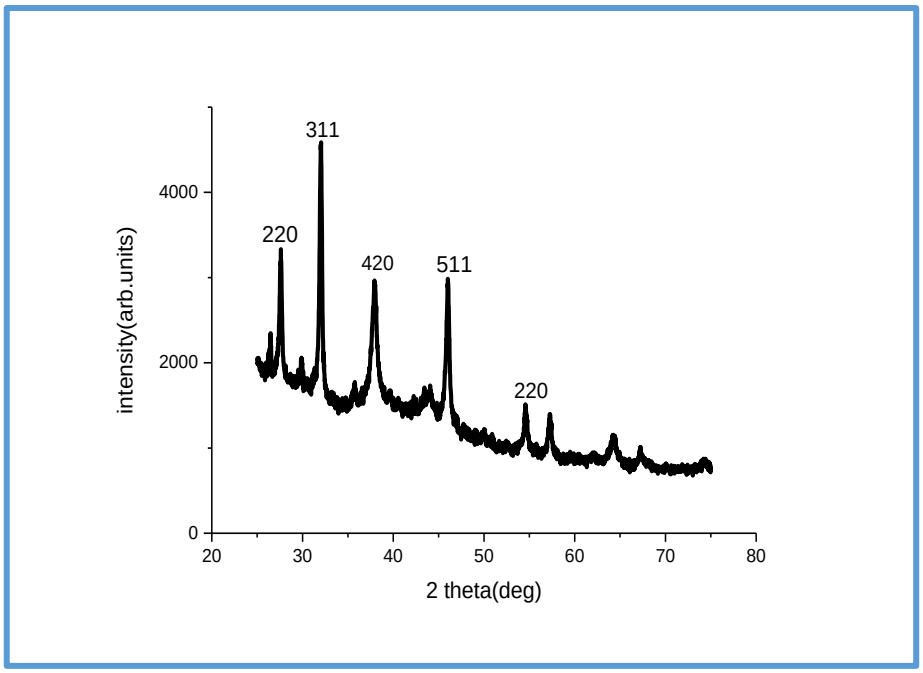


**Figure 5.14** XRD pattern of the Og silver nanoparticles

## 5.6 Conclusions

Silver and zinc oxide nanoparticles were biosynthesized using *Ocimum gratissimum* and *Vernonia amygdalina* plant leaf extracts. Their characterization using optical spectroscopy and electron microscopy revealed that they were spherical in shape. Their FTIR scan results identified biomolecules such as phenols, flavonoids, carboxylic acid and some reducing sugars, and these are suspected to have aided the reduction of the silver ions or the zinc oxide to nanoparticles.

The UV-Vis absorbance spectra of the silver nanoparticles show its surface plasmon resonance (SPR) peak absorbance to be dependent on the concentration of the precursor material (aqueous $AgNO_3$), the reaction times of the silver ions with the plant leaf extract as well as the type of plant leaf extract used. It was observed that the Va silver nanoparticles when left over a lengthy period were unstable resulting in a drop in the peak absorbance due to agglomeration. The TEM of the silver nanoparticles shows that for any concentration of the aqueous silver nitrate the silver nanoparticles were of a range of sizes which were dependent on the concentrations of the aqueous silver nitrate solution used. The XRD pattern of the silver nanoparticles showed that it had the face centred cubic (FCC) structure though with some unusual peaks.

The Og and Va zinc oxide nanoparticles were in clusters as revealed in the SEM images, and their UV-Vis absorbance spectra were pH and leaf extract dependent though their peak absorbance wavelengths from the UV-Vis spectra were lower than that of bulk zinc oxide. The obtained optical energy band gap $E_g$ of the zinc oxide nanoparticles were also found to be pH and leaf extract dependent. The sizes of the ZnO nanoparticles as obtained from SEM measurements and their values were found to be pH dependent though with opposite pH versus size dependence. While the sizes and $E_g$ of the Og ZnO nanoparticles increased with synthesis pH, their $E_g$ values increased with pH of nanoparticle synthesis. For the Va zinc oxide nanoparticles though their sizes increased with synthesis pH, their$E_g$ values decreased with pH of nanoparticle synthesis. The Photoluminescence spectra was pH sensitive and showed two emission peaks: a lower UV emission peak and a higher green emission peak. Their PL spectral

intensities were high for low pH synthesized nanoparticles but low for nanoparticles synthesized at high pH. Because the Og and Va zinc oxide nanoparticles appeared as clusters (Figure 5.8 and 5.9) Moazzen et al 2013 [163], report that such features could make them useful in surface acoustic wave (SAW) device.

This work it is hoped will add to existing knowledge on the use of *Ocimum gratissimum* and *Vernonia amygdalina* leaves.

# Chapter 6

# Electrodeposition of silver thin films in the presence of Og and Va leaf extracts

In this chapter we explored the effect of leaf extracts on the electrodeposition of silver thin films. The study included the electrochemical and structural characterization and comparison of Ag films electrodeposited with and without leaf extracts in the same concentration of aqueous $AgNO_3$ (5 mM) used in biosynthesis of Ag nanoparticles described in Chapter 5.

## 6.1 Introduction

Electrodeposition is one of the most advanced thin film deposition methods that has been widely used today in industrial applications such as electronics, photonics, magnetic recording and coatings for corrosion protection and for size and structure-controlled nanoparticles synthesis [164]. This is because Electrodeposition is a room temperature and low-cost method of thin film growth, characterised by very high selectivity and easy scalability to different length scales (from nanometres to centimetres). Electrodeposition of a metal on a foreign substrate results in the production of the thin film of that metal (which modifies the surface properties of the substrate) which often has physical and chemical properties different from the bulk of the metal. The use of electrodeposition for nanoparticle production apart from being fast and cheap as reported by Mohanty [164] gets the nanoparticles straight onto the substrates and helps in the control of its size, form and structure. The factors that can affect the deposition of the solid metal on the substrate are: (i) the concentration of metal ions in the solution; (ii) the potential (or current density) – depending on the method of electrodeposition employed be it potentiostatic or galvanostatic, (iii) the

nature of background solution (ion adsorption); iv) the solution pH and (v) temperature. In the past, electrodeposition of thin films was mainly used for decorative purposes but today it is an important industrial processing method [165,166] with wide applications in microelectronics, communication, energy generation and optical electronics and that explains the current interest in this technique. The formation of silver films and nanostructures are of interest for various applications such as medical and food packaging due to its (silver) antibacterial properties [167,168].

In this work electrodeposition of silver (Ag) films on a gold (Au) substrates was explored in the presence of leaf extracts. Plant leaf extract is employed in electrodeposition because it has been reported that the biomolecules in plant leaf extracts such as Flavonoids, terpenoids, polyphenols etc cap the film deposits preventing its direct contact between the substrate and the electrolyte and reducing metal dissolution [169]. Electrodeposition of a silver from an aqueous solution is done by application of a constant potential. The equilibrium potential (standard electrode potential) of $Ag^0/Ag^+$, $E^0$ versus standard hydrogen electrode relevant for the electrodeposition is given by the Equation 6.1

$$Ag^+ + e^- \rightleftarrows Ag_s^0 \qquad E^0 = 0.8\ V \qquad (6.1)$$

The electrodeposition of silver onto foreign substrate is illustrated schematically in Figure 6.1. At the potentials negative from the $E^0$ , the deposition of Ag takes place and the Ag film is created. This is also called bulk deposition. Changing the potentials positive from the equilibrium potential is a reverse reaction which will dissolve the Ag films.

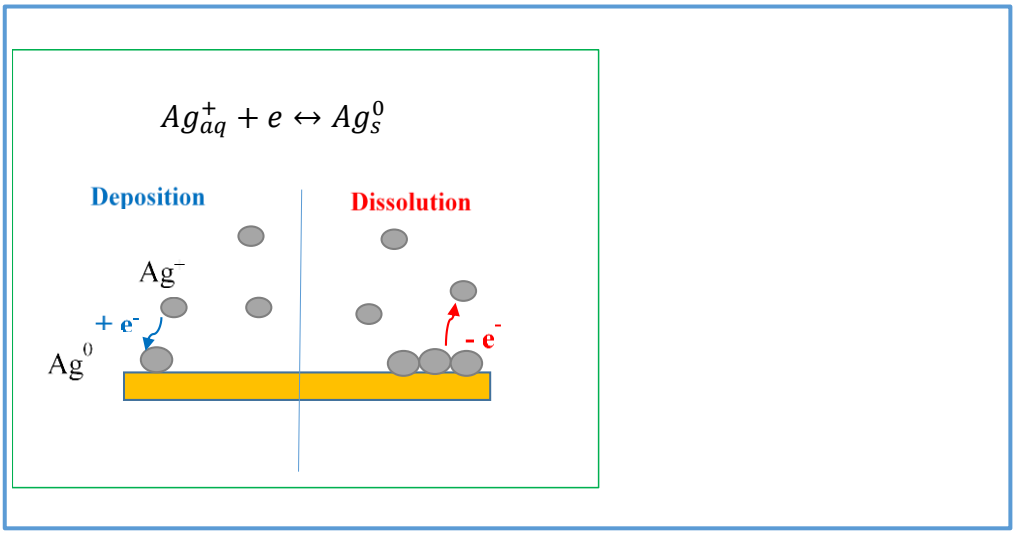


**Figure 6.1** Diagram showing the $Ag/Ag^{+}$ equilibrium and deposition and dissolution process as the potentials are changed with respect to equilibrium

In this work, thin films of silver were grown from an aqueous solution of silver nitrate ($AgNO_3$) in the presence of Og and Va plant leaf extracts. The effect of leaf extracts was characterised electrochemically at different potentials and the morphology of the created silver thin films was studied using Atomic force microscopy (AFM).

During the 10 mins electrodeposition process it was observed that the electrolyte solution changes its colour suggesting that silver nanoparticles were also forming in the solution. The sizes of silver nanoparticles produced in this way were measured and obtained results were compared with those made by the biochemical synthesis method for same length of time.

## 6.2 Literature review

The electrodeposition of zinc on mild steel substrate in an acid chloride solution [170] has been reported. The electrodeposition done with tobacco leaf extract (made from sun-dried tobacco leaves) as additive was at a fixed pH of 5 with temperatures in the range 27 ℃ −30 ℃. By varying the additive concentration as well as electroplating times (15 -18 mins), zinc deposits of masses 24.1-28.3 mg were obtained.

Zinc electrodeposition on mild steel in an acid chloride solution with cassava plant (Manihot) leaf extract has also been reported [171]. The electroplating which was also done at a fixed pH and with varied additive concentration investigated the surface coating efficiencies for different plating times and reported that after 18 mins plating time, the covered surface was devoid of pores, had the lowest corrosion rate and hence the best surface coverage efficiency of 64.5 %.

The electrodeposition of zinc on a mild steel electrode in the presence of an additive Lawsonia inermis (popularly known as Henna) leaf extract has also been reported [172]. In that work zinc bath made up of zinc chloride and excess ammonium chloride was used. By varying the deposition current density and pH of the bath solution, the researchers reported that the presence of henna leaf extract reduced the sizes of the deposited particles and that there was improved adhesion of the zinc deposits to the substrate. Henna leaf extract has also been used as an additive in the electrodeposition of Zinc-Nickel alloy on a steel surface in an acid sulphate bath [173]. A better surface coverage than that achieved with pure zinc, with no porosity was reported. In yet another report, galvanostatic deposition technique was used to study the effect of pineapple juice used as an additive to an acid-chloride electrolyte for the electrodeposition of zinc on mild steel [174]. The zinc deposition on the mild steel substrate was pH and applied current density dependent. The zinc deposits on the substrate said to be dull at low pH values was brighter at high current density values and enabled the mild steel substrate to inhibit corrosion. Though the pineapple juice improved zinc depositions on the substrate, longer electrodeposition periods produced charred zinc deposits on the steel substrate.

From the above literature review, it is evident that not much has been done on the effect of plant leaf extracts as additives for electrochemical deposition of silver on substrates and no data are available on the use of my chosen plant leaf extracts (Ocimum gratissimum (Og) and Vernonia amygdalina (Va) for silver electrodeposition. That is what this research will address.

## 6.3 Objectives of the experimental work

The main objectives of this work were to explore silver deposition on a gold substrate in the presence of the chosen plant leaf extracts with specific focus on:

(i) The effect of the plant leaf extracts on the structure of the silver deposits and in particular on parameters such as the uniformity, grain sizes and surface roughness

(ii) The silver coverage of the substrate as a function of time and deposition potential and determining the average thickness of the silver from measured electrochemical data.

## 6.4 Experimental Methods

### 6.4.1 Electrochemical cell /Electrolyte

The three-electrode cell shown in Figure 6.2 was used for the experiments. Silver films were created by electrochemical deposition method from 5 mM $AgNO_3$+0.1 M $KNO_3$ solution in the presence of the Og or Va leaf extracts as additives. The electrochemical deposition was done with 50 mL solution (45 mL of the aqueous $AgNO_3$ to which 5 mL of the Og/Va plant leaf extract was added). Potassium nitrate ($KNO_3$) was also added to this mixture to ensure a good solution conductivity. The effect of these plant leaf extracts on the resulting nanostructures was studied. The resulting nanostructures were analysed by a combination of surface and structural characterization techniques.

### 6.4.2 Cleaning and preparation of electrodes

Gold films of 250 nm (with 4-10 nm Ti adhesion layer) evaporated on glass were used as a working electrode. The gold thin films were of area 0.5 $cm^2$ and were cleaned in concentrated $H_2SO_4$ in a fume hood for about 5 mins. Thereafter, the sample was rinsed by Milli-Q water and dried using nitrogen gas.

That was followed by butane flame annealing by passing the flame over the gold surface at a height of approximately 3cm several times to remove any hydrocarbons which may have been adsorbed on the surface due to the air/environment exposure. The Au surface cleanliness was confirmed by hydrophilicity test. If a droplet of Milli-Q water completely wet the surface the surface cleanliness was confirmed. Following the test, the sample was dried with nitrogen gas and the working area of the gold substrate was then marked out with nail polish. The reference silver wire electrode and the counter Platinum electrode were cleaned by immersion in 1:1 mixture of $HNO_3$: $H_2O$ for 10 seconds, then rinsed with ultra-pure water and dried with nitrogen gas. The Platinum electrode was then annealed using red hot butane flame for few seconds and allowed to cool down before use.

## 6.5 Electrodeposition and electrochemical characterisation of silver films formed on gold substrate

### 6.5.1 Cyclic voltammetry (CV)

CV on the samples in this work was done at 10 mV/s scan rate in the range -0.05 V to 0.4 V potentials versus $Ag/Ag^+$ ref electrode (Figure 6.2). The CV was done using aqueous 5 mM $AgNO_3$ and then using 5 mM $AgNO_3$ +0.1 M $KNO_3$, with and without the plant leaf extract. Cyclic voltammetry of the aging solution was also briefly explored. Thus, the solution was left to age for about 90 mins and the its CV was repeated to see the effect of a prolonged presence of the leaf extract on the electrodeposition of silver on the gold substrate.

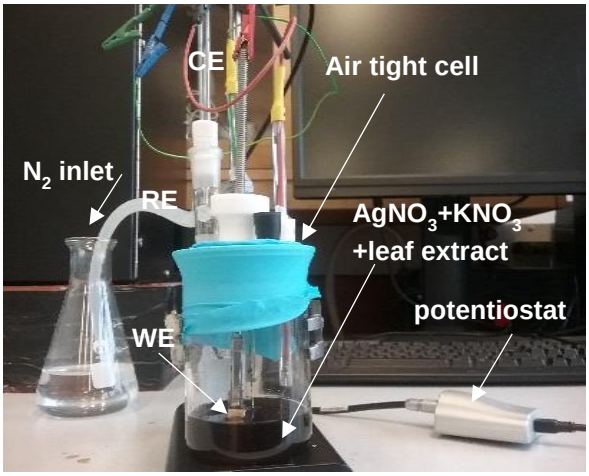


**Figure 6.2** Set up of the three-electrode electrochemical cell used for the electrodeposition of Ag

### 6.5.2 Chronoamperometry (CA)

The CA for this work was done from a solution of 5 mM $AgNO_3$ + 0.1 M $KNO_3$ with and without the plant leaf extracts using the setup of Figure 6.2. This was achieved by setting the potential initially at $E_{level\,1} = 0.3$ V for $t_1$= 20 s then stepping to the deposition potential $E_{level\,2}$ potentials of -0.15 V and later of – 0.3 V for 600 s. The charge of deposition, $Q_{dep}$, was then obtained for each potential by integrating the area under the current-time transients. This value was later used for comparison with the charge of dissolved Ag to determine the efficiency of electrodeposition. Often during deposition process some side reactions can take place and the total current measured during transients cannot be attributed only to the Ag. Therefore, after deposition of silver film, the working electrode (gold substrate) was taken out of the deposition solution, rinsed with ultra-pure water and dried with nitrogen before being moved to a separate solution (Figure 6.3) for dissolution of the Ag (using linear sweep voltammetry) to correctly estimate the thickness of the deposited silver films. When dissolution was not done, the deposited thin films after being rinsed with ultra-pure water were examined for their structure with AFM.

### 6.5.3 Linear sweep voltammetry (LSV)

In this work LSV was used to dissolve silver to be able to estimate the amount of silver which was deposited on the substrate used (gold in this case). The LSV dissolution of Ag done in the set up shown in Figure 6.3 used perchlorate-based solution 1 mM $AgClO_4$ + 0.1 M $HClO_4$ free of any ions that can adsorb on the surface, so the amount of deposited silver could be determined most accurately. As the voltage is scanned from a value $V_1 = -0.005\,V$ that is very close to the equilibrium of Ag to a more positive potential $V_2 = 0.75\,V > E_{eq}^0$ at the scan rate of 10 mV/s silver dissolution occurred.

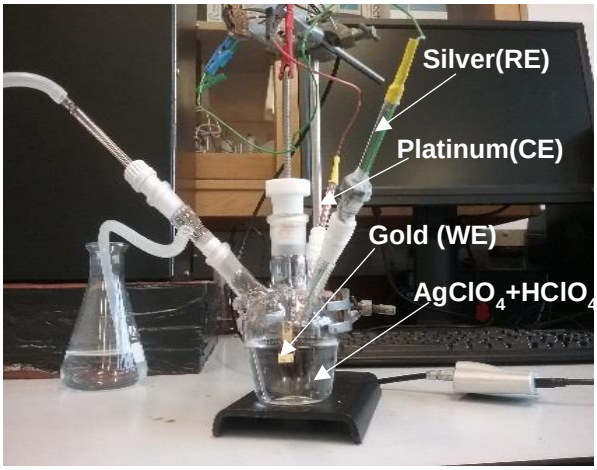


**Figure 6.3** Set up for Linear sweep voltammetry

### 6.5.4 Characterization of silver nanoparticles formed in the solution during electrodeposition

During the electrodeposition of the silver films, a colour change of the electrolyte like that observed during the biochemical synthesis of the AgNPs was observed. The mean sizes of the silver nanoparticles created in the solution were measured using the Dynamic Light Scattering (DLS) technique and the Transmission electron microscope. The TEM JEOL 2010 transmission electron microscope and the Malvern Zetasizer Dynamic Light Scattering (DLS) instrument were used. The mean sizes of the silver

nanoparticles produced by the biochemical method were then compared with the silver nanoparticles produced during the electrochemical deposition process.

### 6.5.5 AFM characterization of Ag films morphology

The surface morphology studies of the gold substrate (working electrode) after the deposition of the silver with and without leaf extracts were done using the Nano surf Easyscan 2 Atomic Force microscope (AFM) for the -300 V deposition potential. The images were analysed using Gwyddion software which facilitated the estimation of the grain sizes as well as the surface roughness of the silver deposits.

## 6.6 Results and discussion

### 6.6.1 Cyclic voltammetry results

The CVs curves (Figures 6.4 and Figure 6.5) show silver deposition on gold as well as its dissolution from Au. It illustrates the effect of the added plant leaf extracts as well as the role of the $KNO_3$ background solution which improved the conductivity of the electrolyte and the rate of electrodeposition. A Comparison of the CVs in Figure 6.4, in the solution immediately after the addition of the leaf extracts show that the kinetics of the silver deposition on the gold working electrode is affected. This is evident in the magnitude of the dissolution peaks when compared with the control CV. The lower current densities in the CV graphs in Figure 6.4 b are indications that both leaf extracts slow down the rate of silver deposition/dissolution possibly due to their adsorption on the surface of the growing film. The inhibition of deposition with the Va leaf extract is greater than that presented by the Og leaf extract. The deposition inhibition is also reflected in a slightly more negative potential of the onset of Ag deposition (negative current increase during cathodic scan) in the presence of Va extract. Because after 10 mins of electrodeposition of silver on gold, there appears to be a spontaneous formation of AgNPs (like that observed during biochemical synthesis), the size of the silver nanoparticles formed were measured with DLS instrument and the results were compared with that obtained from the biochemically synthesized AgNPs after 10 minutes. The results obtained are as displayed in Table 6.4.

The CV done with the aging solution shows two oxidation peaks (Figure 6.). It is likely that as the silver was getting deposited on the gold substrate, silver nanoparticles were simultaneously formed in the electrochemical cell solution resulting in a reduction in the amount of silver available for deposition and producing in effect reduced film thicknesses as shown in Tables 6.1- 6.3.

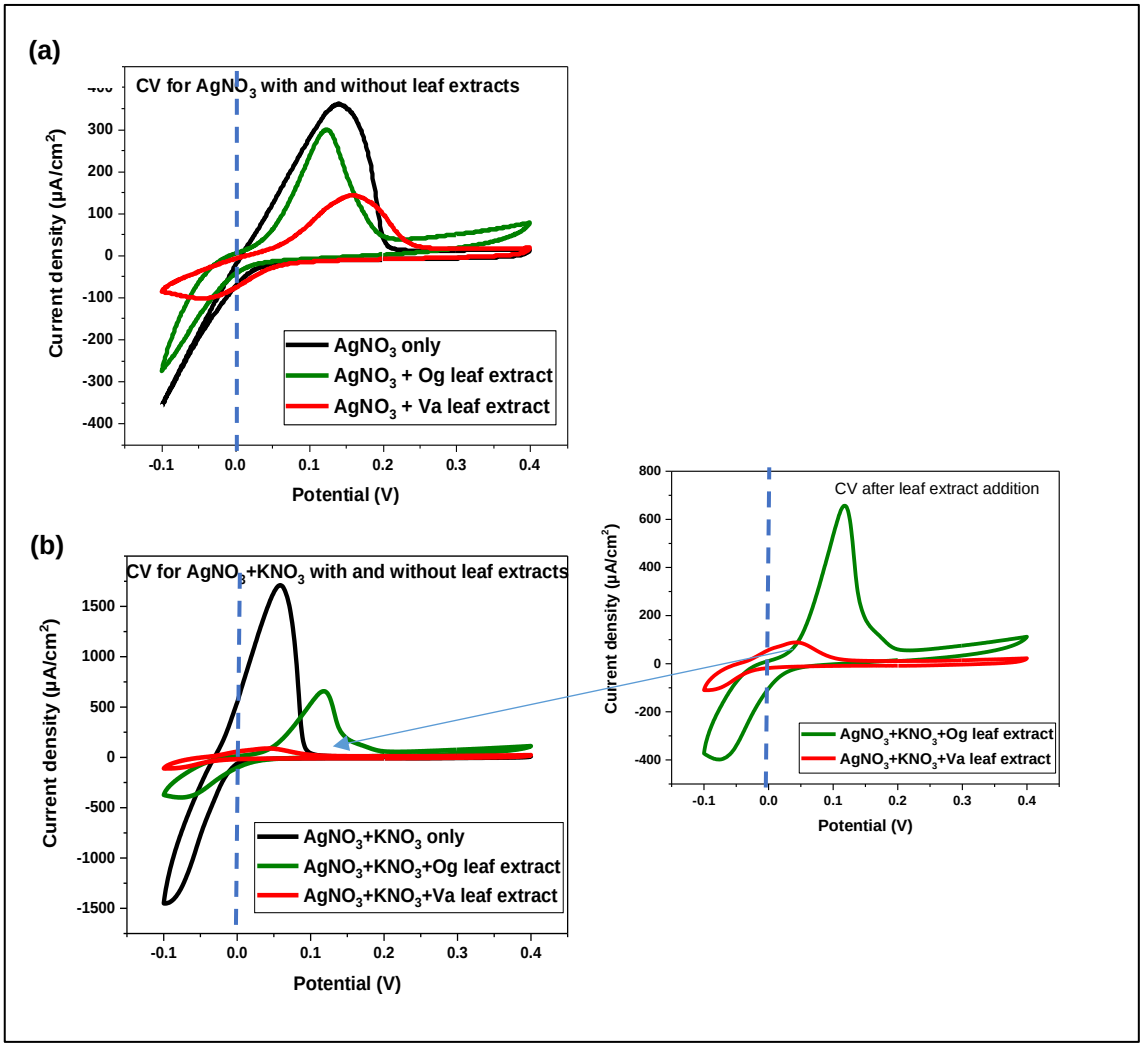


**Figure 6.4** CV plots with and without leaf extracts immediately after leaf extract addition. CVs done in a) 5 mM $AgNO_3$ and b) 5 mM $AgNO_3$+0.1 M $KNO_3$ solution at 10 mV/s. Figure b) inset shows enlarged CVs in the leaf solutions for clarity.

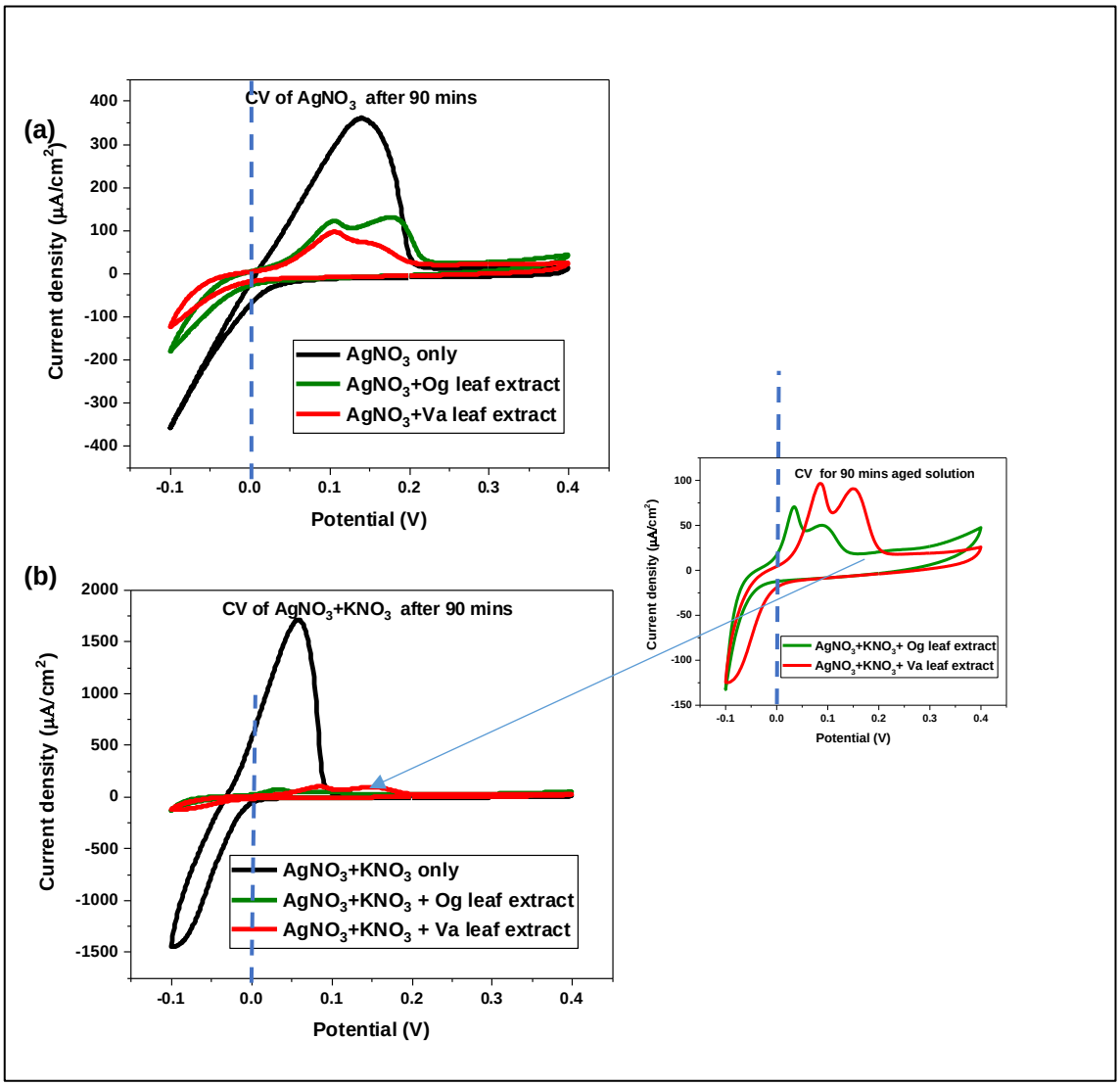


**Figure 6.5** CV plots with and without leaf extracts after ageing for 90 minutes. CVs done in a) 5 mM $AgNO_3$ and b) 5 mM $AgNO_3$+0.1 M $KNO_3$ solution at 10 mV/s. Figure b) inset shows enlarged CVs in the leaf solutions for clarity.

### 6.6.2 Chronoamperometry and Linear sweep voltammetry results

The CA graphs in Figure 6.6 show current transients during electrodeposition of Ag films at different deposition potentials in the solutions with and without leaf extracts leaves. To avoid any ambiguities with the incorporation of AgNPs during electrodeposition due to aging of the solution, the electrodeposition of the thin films was done immediately after the leaf extract addition. Again, the effect on the silver film

deposition with the addition of the background solution $KNO_3$ is illustrated in Figures 6.6a and 6.6b. A comparison of deposition currents at the two different potentials, -0.15 to -0.3 V did not show significant current changes.

The deposition efficiency and thickness of the films were determined by using the data from the LSV dissolution of Ag. The average film thickness of the silver deposits for the two electrolytes as well as the calculated efficiencies of deposition are as given in Tables 6.1and 6.2 respectively for the films deposited at -0.3. The 10 minutes depositions at the two different potentials, -0.15 and -0.3 V showed slight differences and different efficiencies, (probably due to the background processes taking place) and different film thicknesses (Tables 6.1 -6.3).

The presence of the plant leaf extracts affected the amount of silver deposited on the gold by reducing the rate of deposition as shown by lower film thickness in their presence. The average film thickness after 10 mins deposition was highest without the leaf extracts. With the plant leaf extracts, the current levels were lower which is in agreement with the effects observed in the CV experiments, with the Va leaf extract giving the lowest rate of deposition.

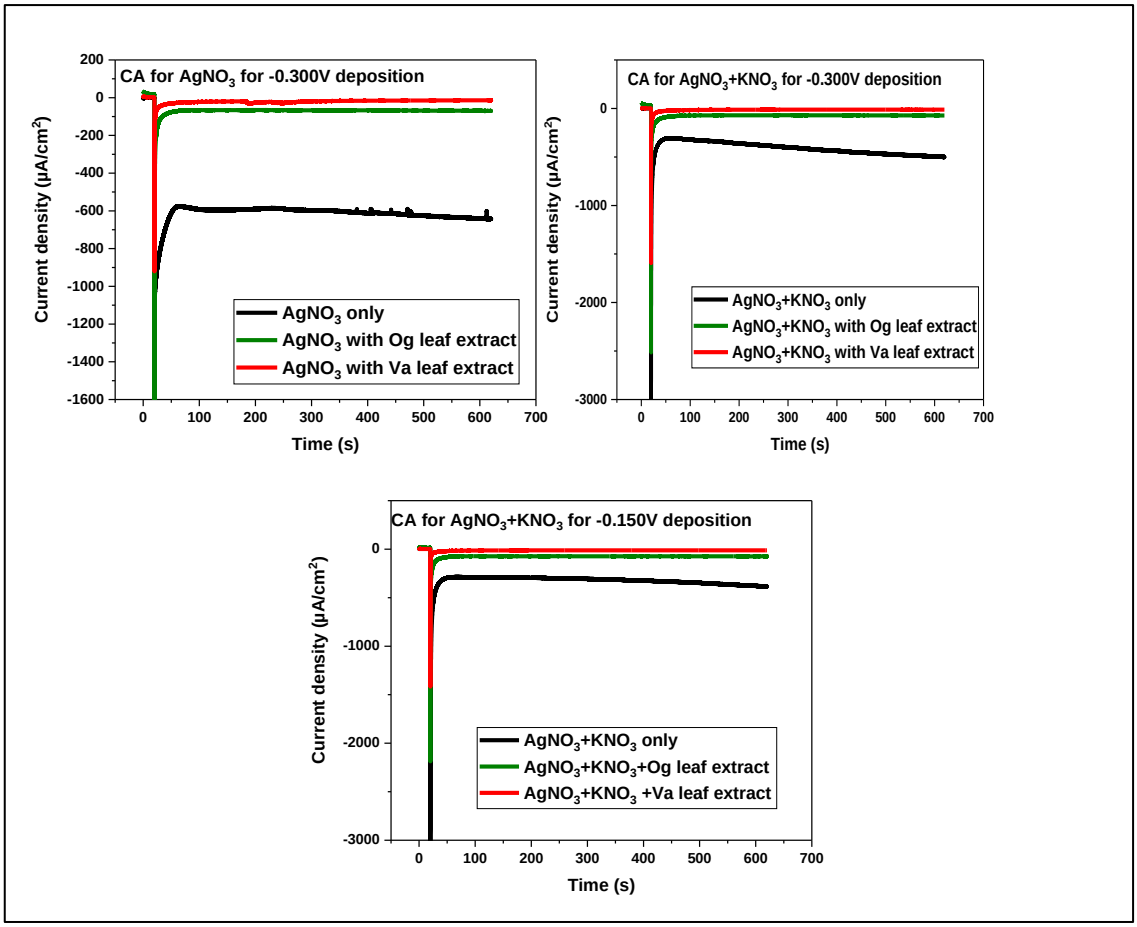


**Figure 6.6 (a)** CA graphs for silver depositions done at potentials -0.150V and -0.300V for 10 min in the solutions with and without leaf extracts.

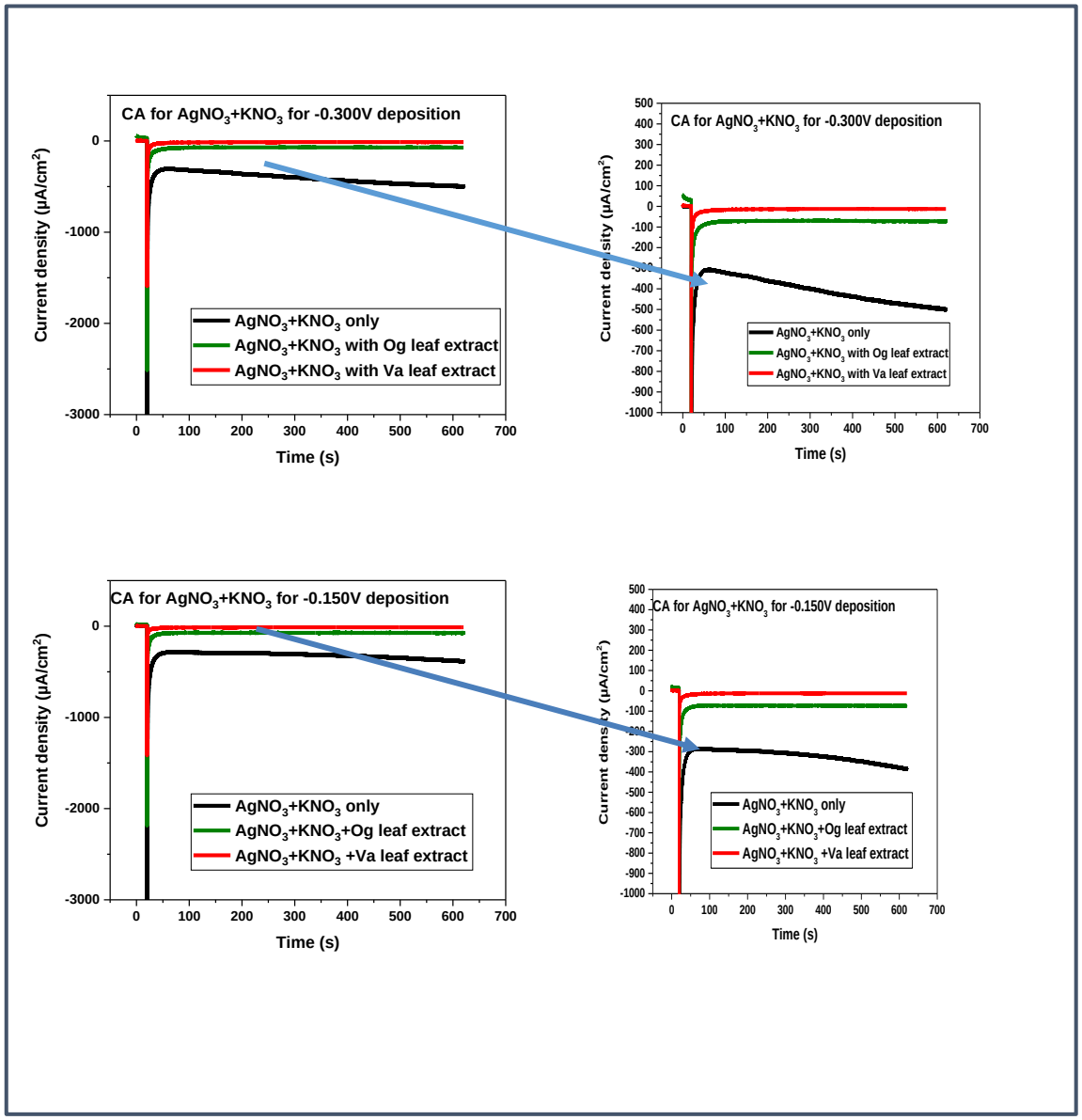


**Figure 6.6 (b)** CA graphs for silver depositions done at potentials -0.150V and -0.300V for 10 min in the solutions with and without leaf extracts with insets showing the current levels in the presence of the leaf extracts were nearly same.

The LSV graphs in Figure 6.7 indicate that the Og leaf extract yields a lower amount of silver deposit at potentials close to the equilibrium potential. However, with a more negative potential of – 300 mV, the Va leaf extract gave a lower silver film deposition on the gold.

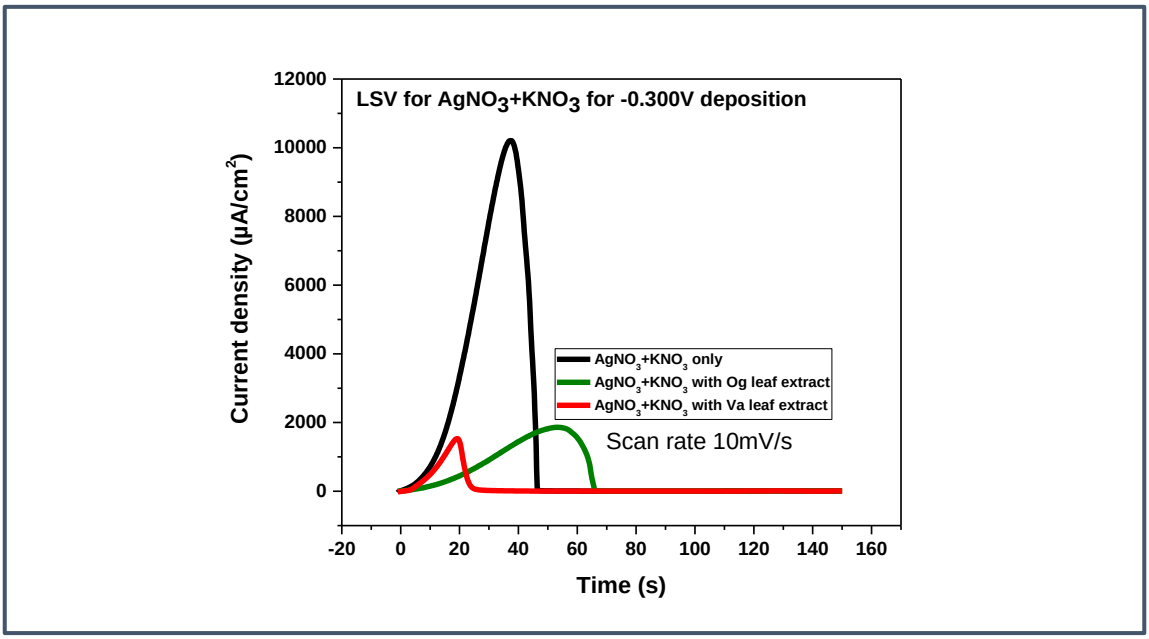


**Figure 6.7** LSV graphs for silver depositions done at -0.300 V for 10 mins.

**Table 6.1** Silver thin film deposition from 5 mM $AgNO_3$ solution with and without the plant leaf extracts at deposition potential of – 0.300 V for 10 min.

| **Electrolyte** | $\boldsymbol{Q_{dep}}(\boldsymbol{mC}/\boldsymbol{cm^2})$ | $\boldsymbol{Q_{diss}}(\boldsymbol{mC}/\boldsymbol{cm^2})$ | Deposition Efficiency $(\frac{Q_{diss}}{Q_{dep}}\%)$ | Average silver film thickness(nm) |
|---|---|---|---|---|
| $AgNO_3$ | 368 | 301 | 82 | 64.0 |
| $AgNO_3$+Og | 42 | 33 | 79 | 7.0 |
| $AgNO_3$ + Va | 12 | 11 | 92 | 2.0 |

**Table 6.2**: Silver thin film after 10 mins deposition from 5 mM $AgNO_3$+0.1 M $KNO_3$ solution with and without the plant leaf extracts at deposition potential of – 300mV and area of substrate 0.50 $cm^2$.

| **Electrolyte** | $\boldsymbol{Q_{dep}}(\boldsymbol{mC}/\boldsymbol{cm^2})$ | $\boldsymbol{Q_{diss}}(\boldsymbol{mC}/\boldsymbol{cm^2})$ | Deposition Efficiency $(\frac{Q_{diss}}{Q_{dep}}\%)$ | Average silver film thickness (nm) |
|---|---|---|---|---|
| $AgNO_3$+ $KNO_3$ | 245 | 104 | 42 | 22.0 |
| $AgNO_3$ + $KNO_3$+ Og | 45 | 31 | 69 | 7.0 |
| $AgNO_3$ + $KNO_3$ + Va | 9 | 8 | 89 | 2.0 |

**Table 6.3**: Silver thin film after 10 mins deposition from 5 mM $AgNO_3$+0.1 M $KNO_3$ solution with and without the plant leaf extracts at deposition potential of – 150mV and area of substrate 0.48 $cm^2$.

| **Electrolyte** | $\boldsymbol{Q_{dep}}$ ( $\boldsymbol{mC/cm^2}$ ) | $\boldsymbol{Q_{diss}}$ ( $\boldsymbol{mC/cm^2}$) | Deposition Efficiency ( $\frac{Q_{diss}}{Q_{dep}}$ %) | Silver film average thickness (nm) |
|---|---|---|---|---|
| $AgNO_3$+ $KNO_3$ | 195 | 117 | 60 | 25.0 |
| $AgNO_3$ + $KNO_3$+ Og | 45 | 38 | 84 | 8.0 |
| $AgNO_3$ + $KNO_3$ + Va | 8 | 7 | 88 | 1.5 |

### 6.6.3 Atomic force microscopy (AFM) results

The AFM was used to examine the morphology of the deposited Ag films. Figure 6.8 shows 5µm images of the deposits grown at the -300 mV potential with and without leaves extracts.

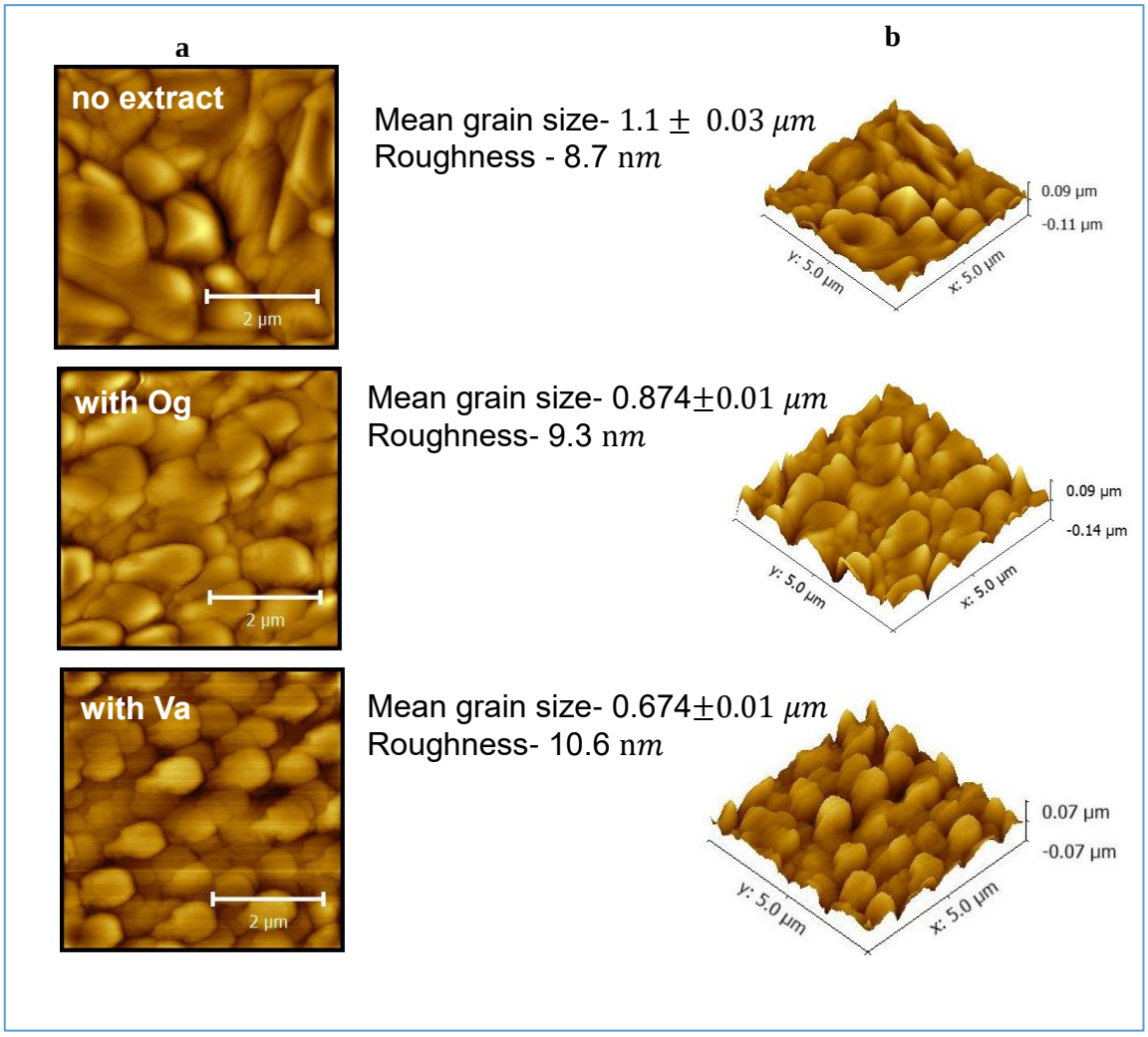


**Figure 6.8 (a)** AFM images of Ag films (b) 3D images of the silver grains on the gold from 5 mM $AgNO_3$ at – 300 mV for 10 mins with and without Og and Va plant leaf extracts

The mean grain sizes for the samples were determined by using Gwyddion software by analysing over 120 grains. The results show that the Og grains were larger( $0.874 \pm 0.03\ \mu m$) than the Va grains ($0.674 \pm 0.01\ \mu m$). The Va leaf extract however produced a higher surface roughness (Roughness- 10.6 n$m$) than the Og leaf extract (Roughness- 9.3 n$m$).

## 6.7 Silver nanoparticles formed in the solution during electrodeposition

During electrodeposition (CA) experiments changes of the electrolyte solution colour were observed. The changes were similar to those observed during biochemical synthesis suggesting the formation of the AgNPs in the solution but at the much shorter time scales. To explore if the NPs formation is the result of the side processes, the electrodeposition of Ag was conducted in a set up with the counter electrode separated in the lugin capillary tube as shown in Figure 6.9. It was observed that the solution colour changes were not induced by counter electrode but mainly at the working electrode.

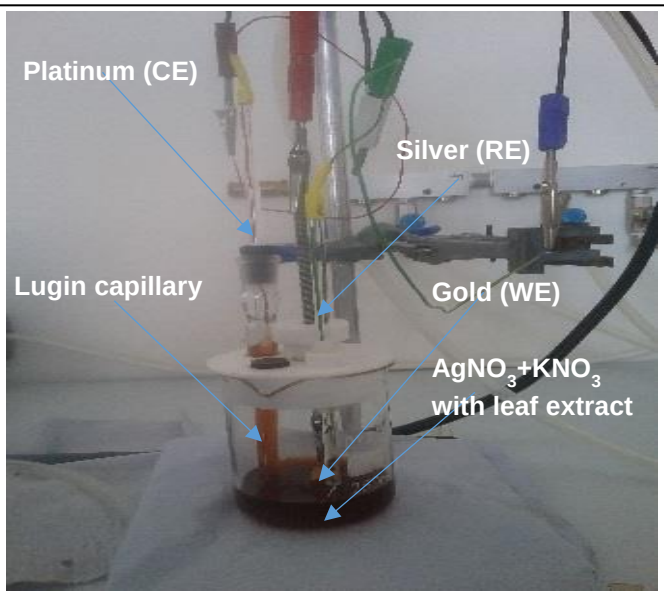


**Figure 6.9** Platinum counter electrode separated from the other electrodes.

## 6.8 Characterization of silver nanoparticles formed during electrodeposition

### 6.8.1 Transmission electron microscope (TEM) and Dynamic light scattering (DLS) results

The TEM images of the Og silver nanoparticles made during electrodeposition of the silver film on the gold are as shown in Figures 6.10. Their TEM size analysis gave the mean size of the Og silver nanoparticles to be 49±1 nm. The Va sample was not examined with TEM as this was not the focus of the work however the DLS data for both the Og and Va silver nanoparticles from both the biochemical and electrodeposition methods are presented in Table 6.4 and shows they have sizes smaller than the biochemically synthesized silver nanoparticles.

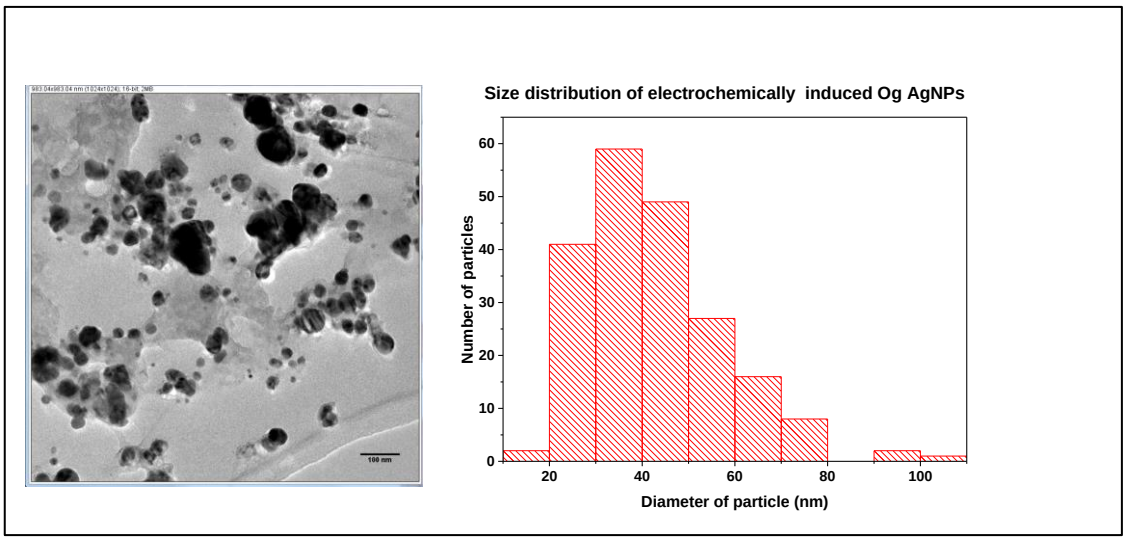


**Figure 6.10** TEM image of Og silver nanoparticles produced during electrodeposition of the silver on gold

**Table 6.4** Dynamic Light Scattering ( **DLS)** size distribution of Ag nanoparticles based on method of synthesis and leaf extract used.

| **Type of Nanoparticles** | **Method of nanoparticle synthesis** | | | |
|---|---|---|---|---|
| | **Biochemical AgNPs synthesis** | | **AgNPs formed during silver electrodeposition on gold** | |
| | **Mean size (nm)** | **Standard deviation** | **Mean size (nm)** | **Standard deviation** |
| Og Silver nanoparticles | 92 | 6.15 | 63 | 2.79 |
| Va Silver nanoparticles | 65 | 5.36 | 47 | 6.94 |

## 6.9 Conclusions

Silver thin film electrodeposition on gold film was done in the presence of Ocimum gratissimum and Vernonia amygdalina plant leaf extracts to see if the leaf extract had any effect on the morphology and film thickness of the silver deposits. Deposition of the silver film was done for 10 minutes from a three-electrode electrochemical cell with analyte of aqueous $AgNO_3$ with and without plant leaf extract. Deposition was done immediately after plant leaf extract addition and later with an aging solution. The obtained results show that the deposition of the Ag film is reduced by the leaf extract molecules adsorbed on growing Ag films which in turn affected the rate of electron transport across the surface (activation effect) as well as the effect on the transport of $Ag^+$ ions towards the electrode. The CV results were in agreement with those of the CA. Regardless of the changes which occur after the electrolyte solution aged, there is a general effect of the plant leaf extract in the solution on the overall effect of the silver deposition/dissolution kinetics. It is possible that the organic molecules in the leaf

extracts interact and adsorb on the surface of the deposited silver and that their presence around the electrode during growth may have affected the transport of the silver ions towards the electrode. The produced Ag film in the presence of the plant leaf extracts had refined grains whose sizes and surface roughness values which were also leaf extract dependent. The silver film average thickness was higher with the Og leaf extract than the Va leaf extract.

# Chapter 7

# Zinc oxide nanofertilizer for Amaranthus cruentus growth

## 7.1 Introduction

The current population explosion which the world is experiencing and the need for food security [175] has made it necessary to look for ways of boosting food production. Traditionally, organic fertilizers were relied on to achieve this, but later bulk chemical fertilizers had to be used. Most recently however, attention has shifted to other sources [176]. Beside the significant amount of resources required for their production, organic fertilizers used for planting food crops can sometimes be unhealthy, as some pathogens from them may cling to the planted crops, risking the food crop contamination. Similarly, bulk chemical fertilizers are becoming more expensive and not so affordable to all farmers. These reasons among others have made it necessary to search for alternative fertilizers and researchers are exploring the possibility of replacing organic and bulk chemical fertilizers with nanofertilizers [177].

The use of nanofertilizers is advantageous because unlike organic or bulk chemical fertilizers, only small quantities are needed for cultivating crops. Using nanofertilizer guarantees the conservation of plants natural minerals, and reduces environmental pollution [178]. With ordinary fertilizers, erosion could result in the washing off from the soil of some essential elements meant to boost the growth of crops, but with nanofertilizers these can be replaced because application of nanoparticles can be tailored and targeted and their small sizes and high surface to volume ratios make them easily absorbable [179]. Nano fertilizers apart from enhancing the growth of plants can stimulate early flowering [180] and in some cases raise their nutritional value [181] or increase their photosynthesis rate and nutrient intake [180, 182]. When nanoparticles are

applied to plants through the soil, the plants can serve as vehicles [183] for taking the nanoparticles up to its shoot through the vascular system. The nanoparticles as they make their way up the shoots, can either form new pores or enlarge already existing ones [184] [185] to accommodate whatever size of nanoparticles are passing through.

Some identified downside to the use of nanoparticles for the cultivating crops include the toxicity to the ecosystem and (in some cases) to the crops grown [186]. Toxicity is mainly from free radicals and can result in DNA destruction [186].

The type of nanoparticles used for growing a plant as well as its concentration [188] are said to affect the yield of its beneficiary plant. While low concentrations of nanoparticles can induce seed germination and enhance the resulting plant growth rate [189, 190], high concentrations of it can result in oxidative stress on the plant thwarting its growth [188].

In this research, the interactive effect of the pH and concentration of zinc oxide nanoparticles synthesized using Og and Va plant leaf extracts on the growth parameters of *Amaranthus cruentus* specifically its seedling characteristics and vegetative growth was investigated. Some aspects of the research has already been published in African Journal of Biotechnology [191] with me as the lead Author. *Amaranthus cruentus* of family *Amaranthaceae* used as spinach in some countries like mine, has protein rich grains and its leaves contain various vitamins. It is fairly affordable by low income earners and thrives in tropical climates. The effect of these nanoparticles on the growth of *Amaranthus cruentus* was studied over a period of 5 weeks in Makurdi Nigeria. This town (latitude 7.44 ° N and longitude 8.32 ° E) is located in the middle belt region of the country [192] which has an annual rainfall in the range 1200 mm -1500 mm , temperature range 21 ℃ - 35 ℃ and with relative humidity in the range 31 % - 85 %.

This work did not discuss the biological process behind the assimilation of the zinc oxide nanoparticles into the plant cells but rather showed how the pH of ZnO nanoparticles synthesis and concentration of the colloidal solution of the nanoparticle used as nanofertilizer used affect the A. cruentus growth. It also gives the different treatments which make observable changes in the seedling characteristics and

vegetative growth of the *Amaranthus cruentus* seeds and plants. Furthermore, for each of the two seed varieties and for the Og and Va zinc oxide nanofertilizer, the treatment beyond which the yield of the plants drops (the critical point) was also investigated.

## 7.2 Literature review

Zinc oxide nanoparticles used for growing plants can be chemically or bio- synthesized but the later method is preferred because chemically synthesized zinc oxide nanoparticles are reported to be toxic to plants and can lower their protein content [178] [193]. Though zinc oxide nanoparticles have been said to enhance seedling, vegetative and root growth in some plants [180], high concentrations of it are reported to induce oxidative stress [188, 194] in shoots and roots of others retarding their growth [195].

While some researchers have reported that zinc oxide nanoparticles can increase the chlorophyll content and photosynthetic pigment of plants [180, 189], others have observed a low rate of photosynthesis in the leaves of plants [196]. Zinc oxide nanoparticles are also said to raise nutrients such as starch, glutelin, protein as well as sugar levels in plants treated with it [181, 197]. Increased biomass [197-199], antioxidant ability of plant enzymes [181], early flowering [180, 193], high seed vigour [200], better vegetative growth with corresponding larger leaves [201] and better yield of shoots and seeds [180, 181] are some of the many benefits derivable from the use of zinc oxide nanoparticles.

Zinc oxide nanoparticles from a pH 5.8 solution has been used for planting *Brassica nigra* seeds [188] and a rise in its non-enzymatic antioxidant ability [188] was reported. In another research, zinc oxide nanoparticles made from a solution of pH 7.4 was re-made using a pH 7 solution for better solubility [201] and used for the irrigation farming of corn. The corn shoot was reported to have broad leaves.

The effects of zinc oxide nanoparticles on the germination of the seeds and shoots of peanuts, corn/maize, rice, soybean, sesamum, chickpea, *Brassica nigra*, onions, mung beans as well as vegetative growth of cabbage, lettuce, cauliflower and tomatoes have also been reported. While the number of seeds used for each study ranged from 5-10

seeds [194, 201] the concentration of zinc oxide nanoparticles used in growing these plants ranged from as low as 1-20 mg/l to as high as 2000 mg/l [180, 188, 194]. Also while the period of growth and study of the nanoparticles effect on the plants ranged from as short as 5 days to as high as 110 days [180, 193], methods of application of the nanoparticles to the seeds or plants were also varied. They included planting the seeds in an already zinc oxide nanoparticles treated soil or soaking the seeds in the nanoparticles before planting. Other methods adopted were irrigation farming of the chosen crops or spraying of the chosen plant shoots with the ZnO nanoparticles after a regular time interval [180, 193].

While the reported researches investigated the effect of zinc oxide nanoparticles on a wide variety of crops and some used ZnO nanoparticles made from solution of a specific pH value, none of them studied the interactive effect of the concentration and pH of synthesis of ZnO nanoparticles on *Amaranthus cruentus* seeds or plants. That is what this present research will address.

Therefore, zinc oxide nanoparticles made from solutions of three different pH values (pH 8, 10 and 12) were used and six different concentrations (10, 100, 500, 1000, 1500 and 2000 mg/l) of their colloidal solutions were used as nanofertilizer for the study. The choice of the stated range of pH of synthesis of the zinc oxide nanoparticles stems from the fact that high pH of nanoparticles synthesis can shorten the precipitation time but raise the purity level of the nanoparticles [202].

## 7.3 Materials and Methods

Colloidal solutions of Og and Va zinc oxide nanoparticles synthesized were used as nanofertilizer for growing two varieties of *Amaranthus cruentus* namely the black-seeded (BS) and pale-seeded (PS) varieties. The zinc oxide nanoparticles solutions were applied thrice to the soil in which the seeds were planted. These were: before the planting, a week after the first seeds emerged and two weeks after the first seed emergence. The effect of the pH of synthesis of the ZnO and the concentration of the colloidal solution of zinc oxide nanofertilizer on the seedling characteristics of the *Amaranthus cruentu*s namely the emergence percent (%E), the emergence index (EI)

and the emergence rate index (ERI) were determined using the equations 7.1-7.3. The vegetative growth the plant namely its height, leaf area and yield percent (equation7. 4) were also studied.

$$\% \text{ E} = \frac{number\ of\ seedlings\ that\ emerge}{number\ of\ seeds\ planted} \tag{7.1}$$

$$\text{E I} = \frac{\sum number\ of\ days\ after\ first\ seed\ emerges \times number\ of\ seeds\ that\ emerge\ that\ day}{total\ number\ of\ seeds\ that\ emerged} \tag{7.2}$$

$$\text{ERI} = \frac{Emergence\ index}{Emergence\ percentage} \tag{7.3}$$

### 7.3.1 Seed planting and soil preparation

Two varieties of *Amaranthus cruentus* were chosen for the study. These are the black-seeded variety (Figure 7.3 a) and the pale-seeded variety (Figure 7.3 b). The seeds were treated as follows: (i) soaked in nanoparticle solution for 10 mins before planting, (ii) soaked in water for 10 mins, and (iii) not soaked in either water or nanoparticles.

In this study, it was assumed that the *A. cruentus* seeds used are of good quality and therefore have no defects, hence are expected to grow well. The soil in which the *A. cruentus* seeds were planted was first analysed for its constituent elements before the planting and after harvesting the plants. The soil analysis before the planting showed it to be of pH 6.00 and made up of 79.5 % of sand, 10.5 % clay and 10.0 % silt. Organic carbon was 1.50 %, while its zinc content was 0.24 mg $kg^{-1}$. The pots used for the planting each contained $8 \times 10^{-3}\ m^3$ of soil treated with 50 ml of the liquid nanofertiliser, but the blank control pots contained untreated soil. The seeds were planted in the soil at a depth of 0.7 cm and there were three replications (Figure 7.2) of each soil treatment. The pots were housed in a screen house (Figure 7.1) to protect the germinating seeds and subsequently growing plants from all other factors, except the effects of the applied nanofertilizer. One hundred seeds were planted in each pot in

accordance with the international Seed Testing Association (ISTA) prescription [203]. After determining the emergence percent for each seed variety and treatment, the plants were thinned from one hundred to eight. Four of these eight plants were tagged and labelled (Figure 7. 3 c) for all other investigations that were done.

**Figure 7.1** Screen house to shield the plants from factors other than those investigated

**Figure 7.2** layout of pots containing plants with three replications of each treatment

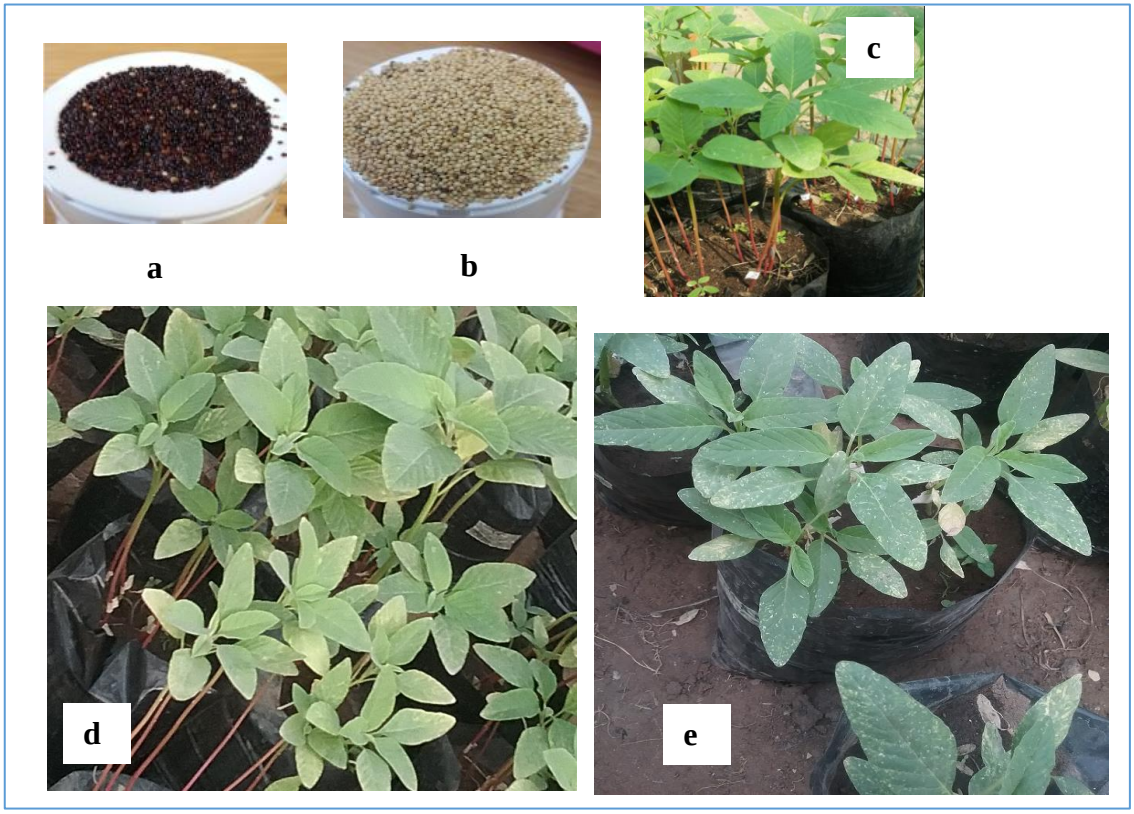


**Figure 7.3** (a) Amaranthus cruentus black seeded (b) pale seeded varieties.

The period of the whole study was five weeks. At the end of the five weeks and for each pot, which had nanoparticles in the soil, and hence each treatment including the control, the fresh plants were harvested, and the fresh weight was determined. The plants were then dried in an oven set to 70 ℃ for 72 hours and their dry weight in each case was also measured. From these data the yield of the plants was determined using equation (7.4) below:

$$Yield\ \% = \frac{Dry\ weight\ of\ plants}{Fresh\ weight\ of\ plants} \times 100 \qquad (7.4)$$

The seedling characteristics were studied for a period of one week. Four factors were considered in this study. These were (i) pH of the biosynthesised zinc oxide nanoparticles, (ii) seed varieties of the *Amaranthus. cruentus*, (iii) concentration of the colloidal solution of the zinc oxide nonfertilizer, and (iv) seed soaking.

### 7.3.2 Zinc oxide nano fertilizer

Zinc oxide nanoparticles from three different pH solution namely pH8, pH 10 and pH 12 referred to as P1, P2 and P3 respectively and with concentrations of its colloidal solutions: 10, 100, 500,1000, 1500, and 2000 mg/L designated as N1, N2, N3, N4, N5, and N6 respectively were used for the study. The blank control pots which contained untreated soil /plants were labelled as P0N0.

### 7.3.3 Statistical analysis

The data resulting from the interactive effect of the pH and concentration of the applied nanoparticles on the plants under investigation was subjected to the analysis of variance (ANOVA) and the tests were done at 5 % probability (or 95 % confidence Interval CI) using Genstat release 10.3 DE. The effect of the seed soaking before planting was found to be insignificant and hence ignored. The obtained results for the effect of pH and concentration on the percent emergence (%E), Emergence index (EI), Emergence Rate Index (ERI) and leaf Area are plotted using bar charts (Figures 7.4-7.9, and 7.14) and to add credibility to the results, error bars were added. By drawing lines across, from the bottom of the error bar with the highest dependent variable (%E, EI, ERI etc) or from the top of the error bar with the lowest dependent variable it was possible to tell which differences were significant and which ones were not.

## 7.4 Results and discussions

## 7.5 Seedling characteristics

The planted seeds took two days to start emerging from the soil and all the viable seeds germinated after ten days. The response of the treated seeds in each case was compared with that of the blank control (P0N0). Tables 7.1a and b give an overview of which

treatments gave good results and which ones produced poor results for each seed variety.

### 7.5.1 Percent emergence (%E)

This gives the number of seeds that germinate out of the 100 planted. High percentages of emergence are desirable. The Og zinc oxide nanoparticles synthesized at all three pH levels raised the percent emergence of the pale-seeded variety above that of the control. The best percent emergence of 69 % for the P1N2 treatment given to the pale-seeded variety is from the error bar analysis (Figure 7.4) significantly different from the outcome of the other treatments. This result is 19 % higher than the value recorded for the control PS variety and 38 % higher than the value obtained for the control BS variety. The worst percent emergence of 29 % (P3N1) for the black-seeded variety was significant for most PS treatments but was not significantly different from the values obtained for other BS treatments. The poor % E result from the pH 12 nanoparticles, could be because of their large sizes which as explained in the introductory part of this chapter, made them unable to penetrate the plant cell membrane and create the desired growth enhancement.

For the Va zinc oxide nanoparticles, a similar trend was observed as most of the treatments favoured the pale-seeded variety. The P3N1 treatment gave the best percent emergence of 67 % for the pale-seeded variety, which was significantly different from those of other treatments. The control (P0N0) for the BS variety gave the worst percent emergence of 33 % which was significantly different from the results of some treatments given to the PS variety (Figure 7.5). Tables 7.1 a and 7.1 b give a summary of the plant performances for different treatments.

**Table 7.I a** Summary of the Og zinc oxide Nano fertilizer treatments that produce good or poor results for each seed variety.

| Parameter | Og ZnO Nano fertilizer | | | |
|---|---|---|---|---|
| | Best treatment | Seed variety/Results | Worst treatment | Seed variety/Results |
| % E | P1N2 | PS (69 %) | P3N1 | BS (29 %) |
| E I | P1N2 | BS (2.28) | P0N0 | BS (4.00) |
| ERI | P1N3 | PS (3.89) | P0N0 | BS (9.8) |

**Key:** PS→ Pale- seeded Amaranth. BS→ Black- seeded Amaranth.

P1 = pH 8, P2 = pH 10, P3 = pH 12. N1 = 10 $mgl^{-1}$; N2 = 100 $mgl^{-1}$; N3 = 500 $mgl^{-1}$

**Table 7.I b** Summary of the Va zinc oxide Nano fertilizer treatments that produce good or poor results and for which seed variety.

| Parameter | Va ZnO Nano fertilizer | | | |
|---|---|---|---|---|
| | Best treatment | Seed variety/Results | Worst treatment | Seed variety/Results |
| % E | P3N1 | PS (67 %) | P0N0 | BS (33 %) |
| E I | P1N2 | PS (2.34) | P0N0 | BS (5.00) |
| ERI | P1N3 | PS (3.33) | P0N0 | BS (10.00) |

**Key:** PS→ Pale- seeded Amaranth. BS→ Black- seeded Amaranth.

P1 = pH 8, P2 = pH 10, P3 = pH 12. N1 = 10 $mgl^{-1}$; N2 = 100 $mgl^{-1}$; N3 = 500 $mgl^{-1}$

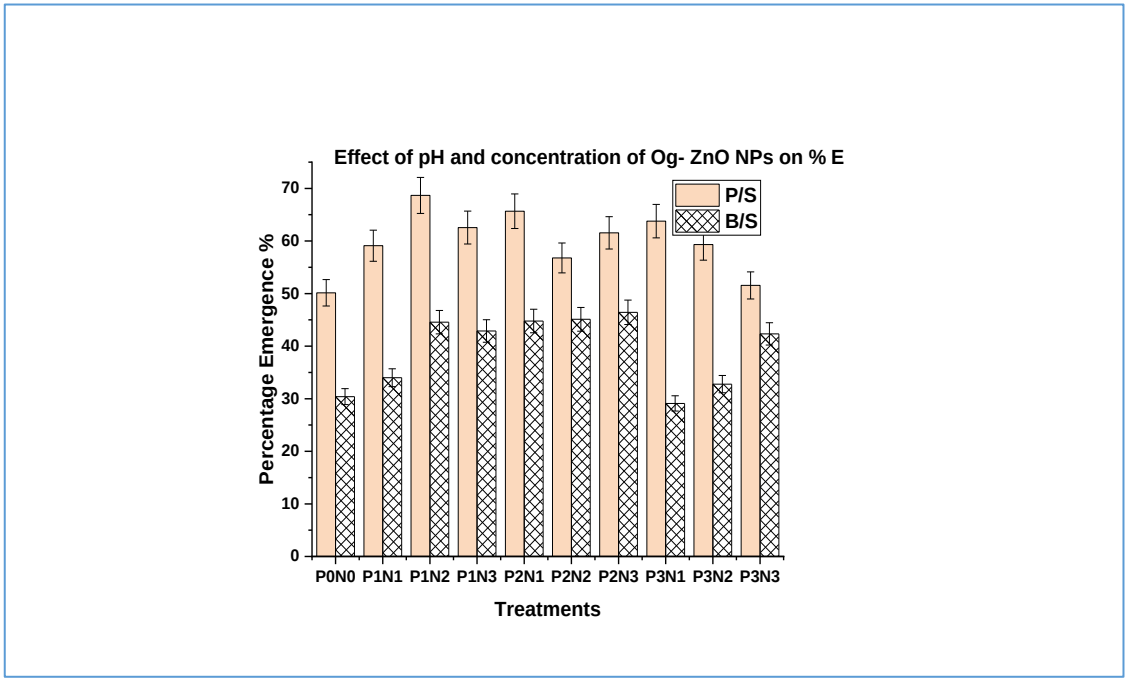


**Figure 7.4** Interactive effect of pH and concentration of colloidal solutions of Og zinc oxide nanoparticles on the percentage emergence of the *Amaranthus cruentus* seed.

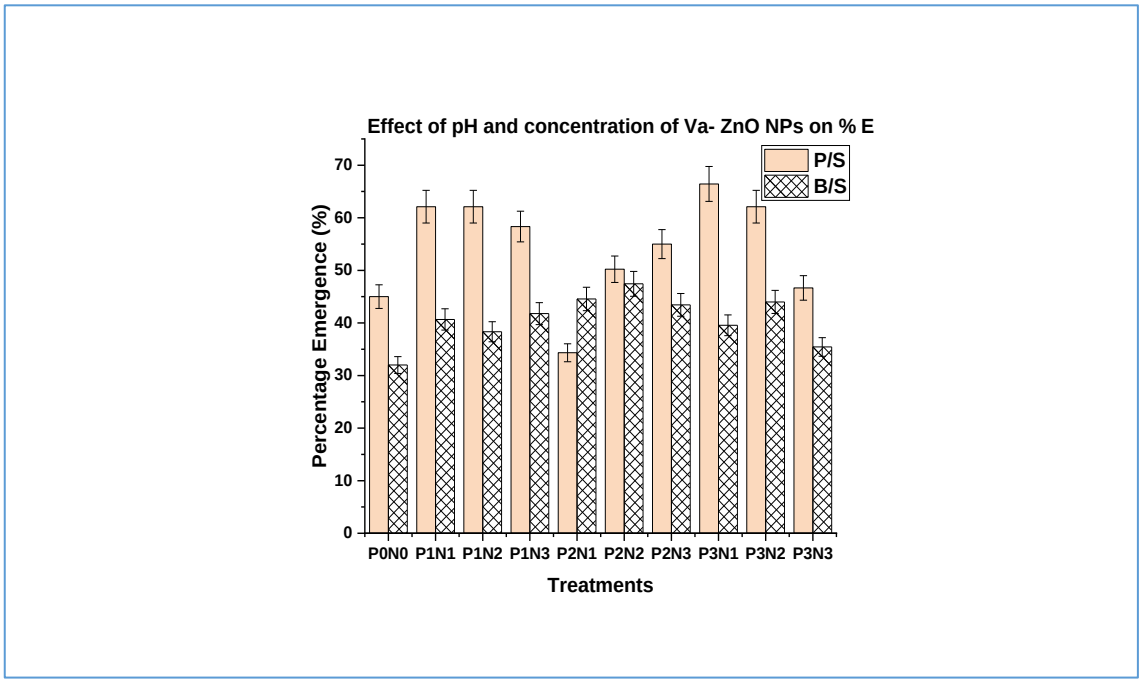


**Figure 7.5** Interactive effect of pH and concentration of colloidal solutions of Va zinc oxide nanoparticles on the percentage emergence of the *Amaranthus cruentus* seed.

### 7.5.2 Emergence index (EI)

The emergence index gives an indication of the uniformity of growth of both the pale-seeded and black-seeded varieties. For the Og zinc oxide nanoparticles, the control (P0N0) had the worst EI values of 4 for the black-seeded variety and 3.5 for the pale-seeded variety (Figure 7.6). These values are significantly different from those of other treatments. The best EI value of 2.28 was obtained for the BS variety (P1N2) but this is not significantly different from the values obtained for other treatments. For Va zinc oxide nanoparticles however the worst EI value of 5 was obtained for the BS variety of the control (P0N0) and was significantly different from the results of the other treatments. The best EI value of 2.34 (P1N2) obtained for the pale-seeded variety is significant when compared to the outcome of BS (P3N2) but is not significant when compared with the results from other treatments given to PS plants (Figure 7.7).

A summary of key EI performance results of the seeds is given in Tables 7.1 a and b.

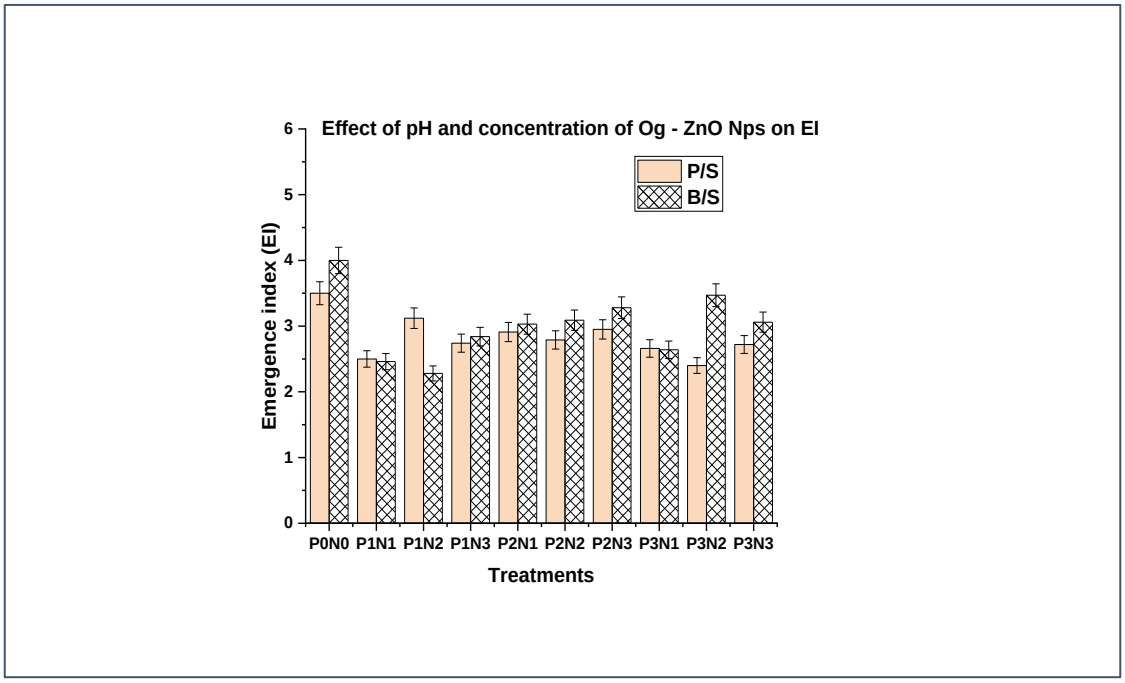


**Figure 7.6** Interactive effect of pH and concentration of colloidal solutions of Og zinc oxide nanoparticles on the emergence index of the *Amaranthus cruentus* seeds.

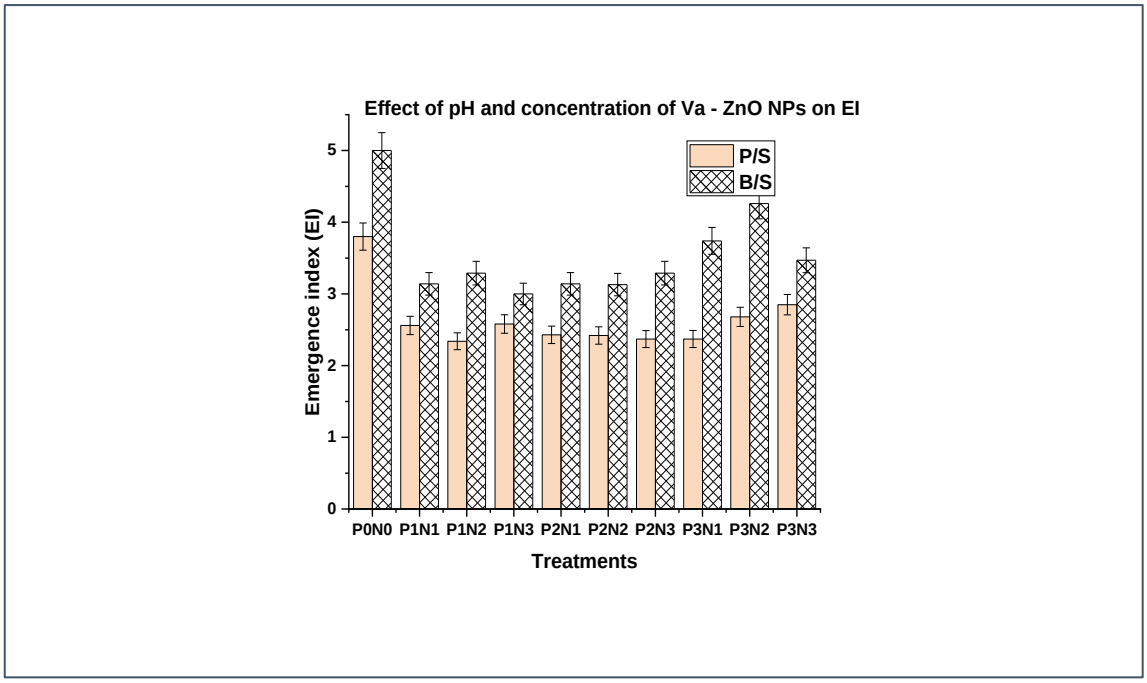


**Figure 7.7** Interactive effect of pH and concentration of colloidal solutions of Va zinc oxide nanoparticles on the emergence index of the *Amaranthus cruentus* seed.

### 7.5.3 Emergence rate index (ERI)

This term gives the ease with which the planted seeds germinate. Lower ERI are better than higher ones. Obtained results show that for both the Og and Va zinc oxide Nano fertilizer, the control P0N0 had the worst ERI values for the BS variety. For the Og zinc oxide nanoparticles, the best ERI value of 3.9 (P1N3) obtained for the pale seeded variety was not significantly different from the outcome of the treatment given to other PS plants but it was significant for P3N1 and P3N2 treatments given to the BS variety (Figure 7.8). For the Va ZnO Nano fertilizer however, the control (both BS and PS) had the worst ERI values of 10 for the BS plants. The best ERI value of 3.33(P3N1) obtained for the PS variety is significant for most BS plants but not significantly different from values observed for other PS plants (Figure 7.9). A summary of key results is also shown in Table 7.1b.

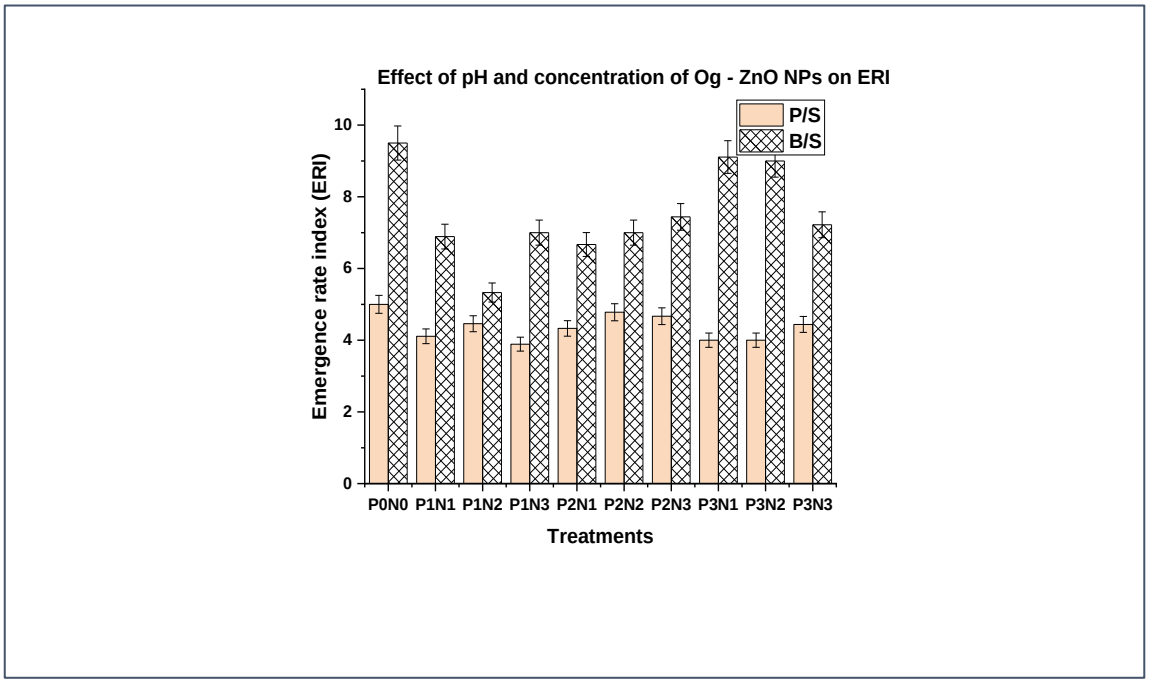


**Figure 7.8** Interactive effect of pH and concentration of colloidal solutions of Og zinc oxide nanoparticles on the emergence rate index of the *Amaranthus cruentus* seeds.

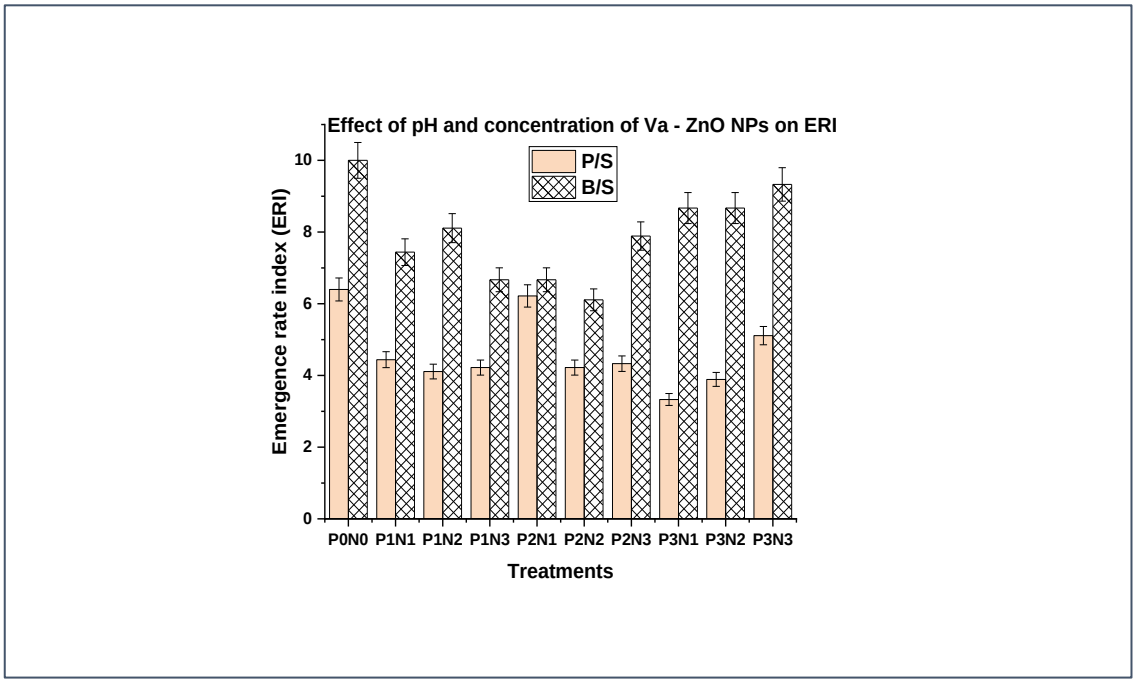


**Figure 7.9** Interactive effect of pH and concentration of colloidal solutions of Va zinc oxide nanoparticles on the emergence rate index of the *Amaranthus cruentus* seeds.

## 7.6 Vegetative growth of the *Amaranthus cruentus*

### 7.6.1 Plant height

The effect of the nanoparticles on the height of the plant for a period of five weeks was studied and comparison as before was made with that of the control (P0N0). In most cases and for the two seed varieties, the plants got to their maximum height after four weeks and beyond this there seemed to be no reasonable increase in height (Figures 7.10 - 7.13). In all cases the control (P0N0) was the shortest. It was also observed that for the Va zinc oxide Nano fertilizer treated black seeded variety plants, their heights generally increased when treated with nanoparticles synthesized at lower pH (Figure 7.10a). This means that smaller nanoparticles favoured height enhancement of the pale and black- seeded variety (Figure 7.10b). Similarly, the PS plants treated with pH 8, 10 mg/l Og zinc oxide nanofertilizer, were the tallest while the control (P0N0) plants were the shortest. (Figures 7.11a and b).

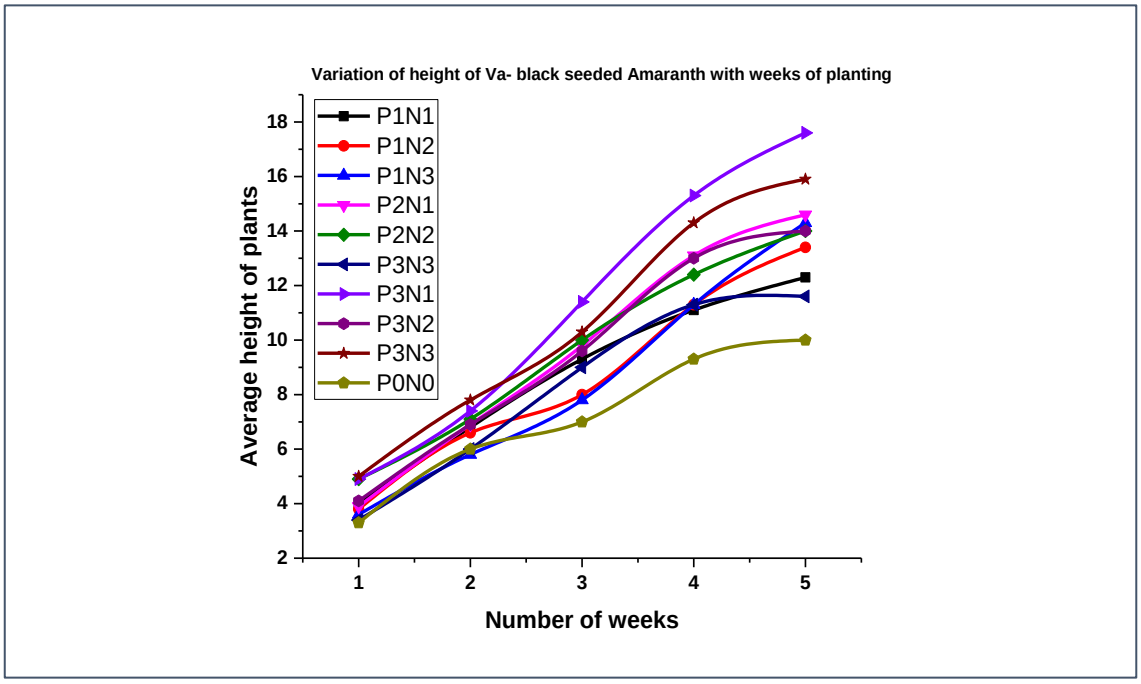


**Figure 7.10a** Variation of height of Va – *Amaranthus cruentus* black-seeded plants with weeks of planting

It was observed that while low pH synthesized nanoparticles produced taller plants, high pH synthesized nanoparticles produced shorter plants. It was also observed that the pale- seeded plants had thicker stems and grew taller than the black seeded variety.

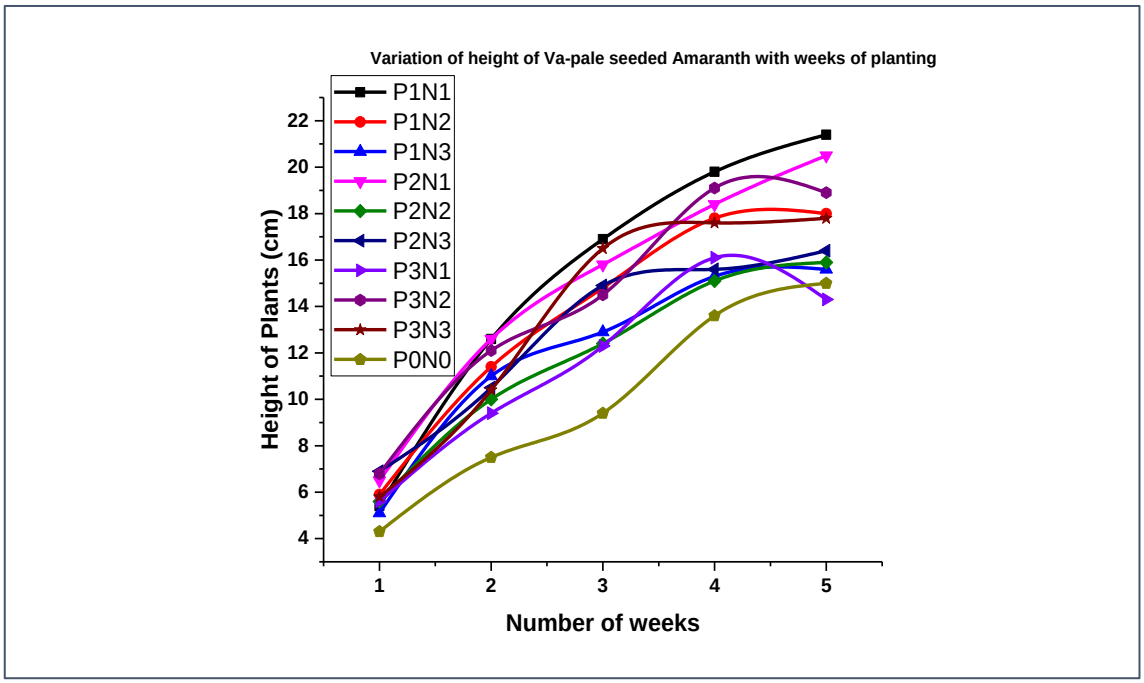


**Figure 7.10b** Variation of height of Va – *Amaranthus cruentus* pale-seeded plants with weeks of planting

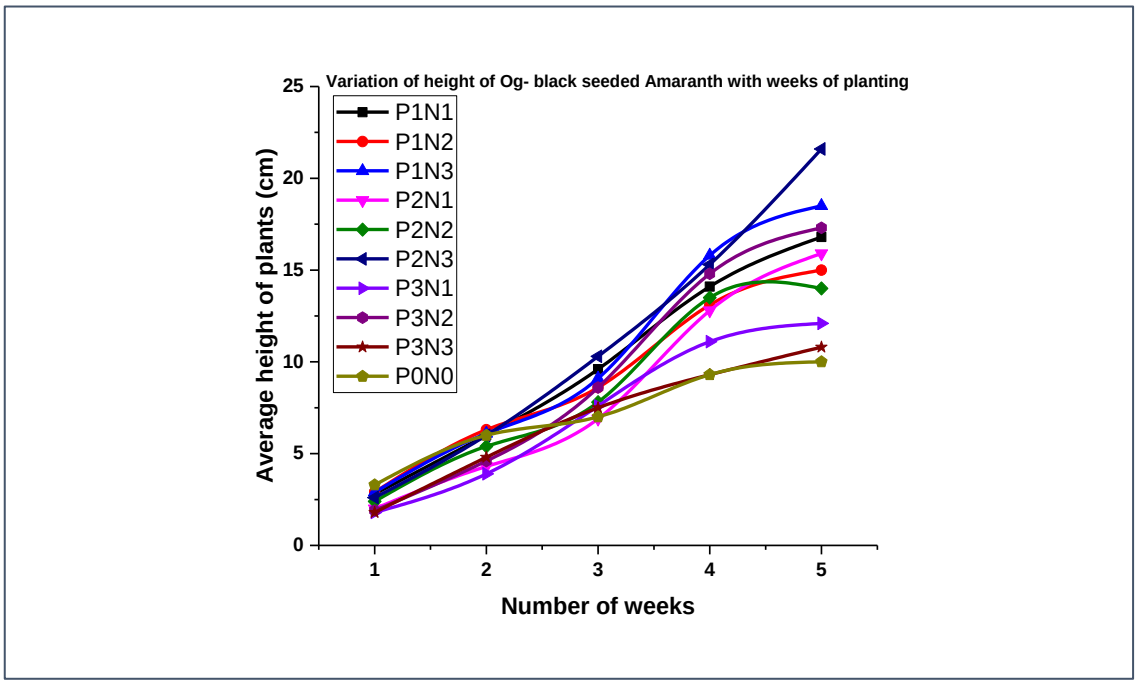


**Figure 7.11a Variation** of height of Og – *Amaranthus cruentus* black-seeded plants with weeks of planting

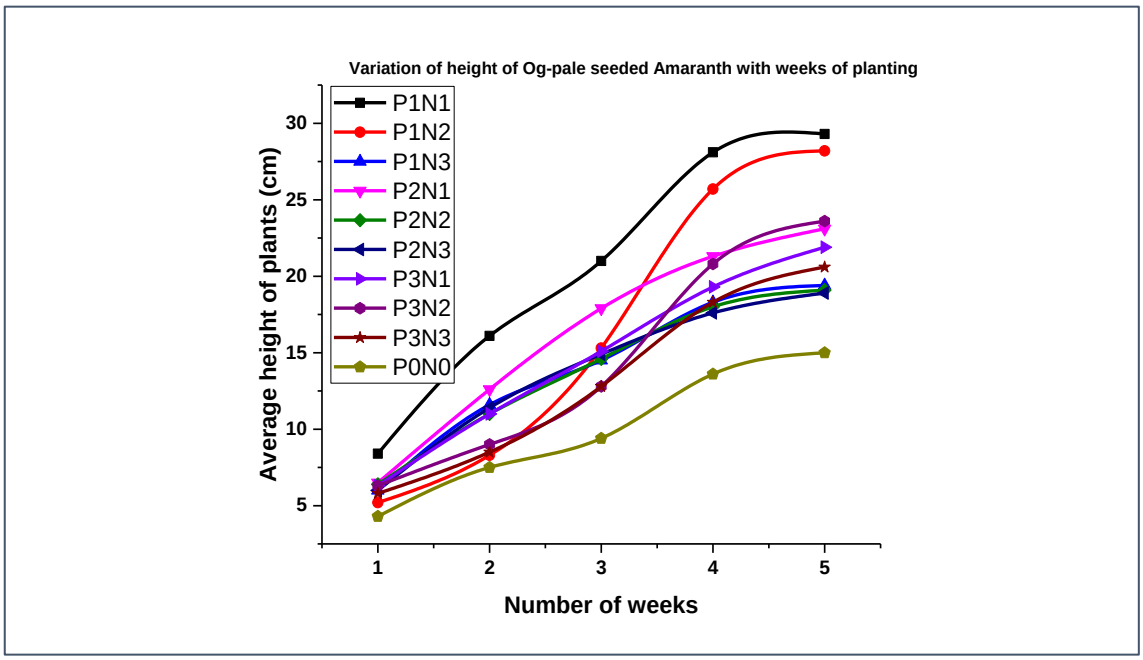


**Figure 7.11b Variation** of height of Og – *Amaranthus cruentus* pale-seeded plants with weeks of planting

### 7.6.2 Leaf Area

For all the three pH levels, the black seeded variety plants which were given the Og zinc oxide nanoparticles treatment had a better shoot growth than the pale seeded variety except for the control. For the Og zinc oxide nanoparticles the treatment which produced large leaves of area 63 $cm^2$ was P2N3 for the BS variety, This value was significantly different from the result of all other treatments. This same treatment resulted in the worse leaf area of 4 $cm^2$ for the PS plants and the result was also significantly different from the outcome of other treatments Thus, while the black-seeded variety had more broad leaves for a given treatment, the pale-seeded variety produced scanty and mostly narrow leaves.

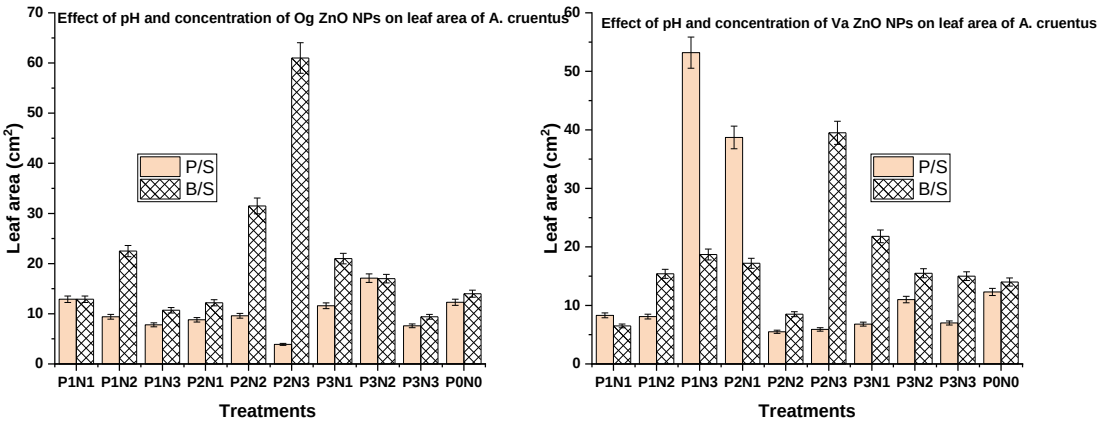


**Figure 7.12 Variation** of Leaf Area of Og and Va – *Amaranthus cruentus* black and pale-seeded treated plants.

For the Va zinc oxide nanoparticles, the P1N3 treatment given to the PS plant had the broadest leaf of area 53 $cm^2$ which was significantly different from the result of all other treatments. The narrowest leaf was of area 5 $cm^2$ due to nanoparticles made in pH 10, 100mg/L solution but this result though significant for the BS variety was not significant for the pale seeded plants.

### 7.6.3 Yield of plants

The yield percent was calculated to see how much dry biomass resulted from the fresh plants harvested. Furthermore, it was used to identify the particular nanoparticle concentration beyond which there was a sharp decrease in the yield of the *Amaranthus cruentus* plants (critical point). In all cases, the control P0N0 gave the lowest yield. . Generally, for both the Og and Va zinc oxide nanoparticles synthesized at all three pH levels except for the Og pH 12 zinc oxide nanoparticles which showed the black seeded variety as having a high yield percent, the pale seeded variety gave better yield percent than the black seeded variety. Table 7.2 gives a summary of the yield of the investigated plant.

While the critical point for the pH 8 Va ZnO nanofertilizer was found to be 10 mg/l for the black seeded variety, it was 500 mg/l for the pale seeded variety. For the Og zinc oxide nanoparticles, the critical point for the black seeded variety was 100 mg/l while for the pale seeded variety two points (Figure 7. 13) namely the 10 mg/l and 500 mg/l concentrations were identified.

**Table 7.2** ZnO Nano fertilizer Treatments and yield outcome for Black seeded (BS) and pale seeded (PS) varieties

| Nano - ZnO pH | Va Nps | | Og Nps | | Maximum Yield % for each pH for the Og /Va nanoparticles |
|---|---|---|---|---|---|
| | Treatment | Seed variety/yield | Treatment | Seed variety/yield | |
| pH 8 | P1N1<br>P1N3 | BS (23%)<br>PS (29%) | P1N2<br>P1N1<br>P1N3 | BS (19%)<br>PS (23%)<br>PS (21%) | PS (Va NPs) 29%<br>PS (Og NPs) 23% |
| pH 10 | P2N1<br>P2N3 | BS (27%)<br>PS (23%) | P2N3<br>P2N3 | BS (25%)<br>PS (60%) | PS (Og NPs) 60%<br>BS (Va NPs) 27% |
| pH 12 | P3N3<br>P3N3 | BS (22%)<br>PS (25%) | P3N1<br>P3N3<br>P3N3 | BS (35%)<br>BS (16%)<br>PS (18%) | PS (Va NPs) 25%<br>BS (Og NPs) 35% |

**KEY:** Nps – nanoparticles
BS – Black seeded PS – Pale seeded

For the Va pH 10 ZnO nanoparticles, the critical points were 100 mg/l for the black seeded variety and 500 mg/l for the pale seeded variety while for the Og zinc oxide nanoparticles treated plants and for both the black seeded and pale seeded varieties, the critical point was 500 mg/l, though with a slight yield increase for the 1500 mg/l concentration (Figure 7.14).

The critical point for the pH 12 Va ZnO nanoparticles (Figure 7.15) treated plants was found to be 500 mg/l for both plant varieties but for the Og ZnO nanoparticles treated black seeded plants, three points were observed. These were 10 mg/L 500 mg/L and 1500 mg/l concentrations with the yield percent decreasing in that order. For the pale seeded variety, the critical point was observed at 500 mg/l concentration. Thus from these analysis, the pale seeded variety had the highest yield and this agrees with the results of the seedling characteristics for the same variety. For all nanoparticles and for all synthesis pH, there was a sharp decrease in yield for treatments done with 1000 mg/L-2000 mg/L ZnO Nano fertilizer concentration.

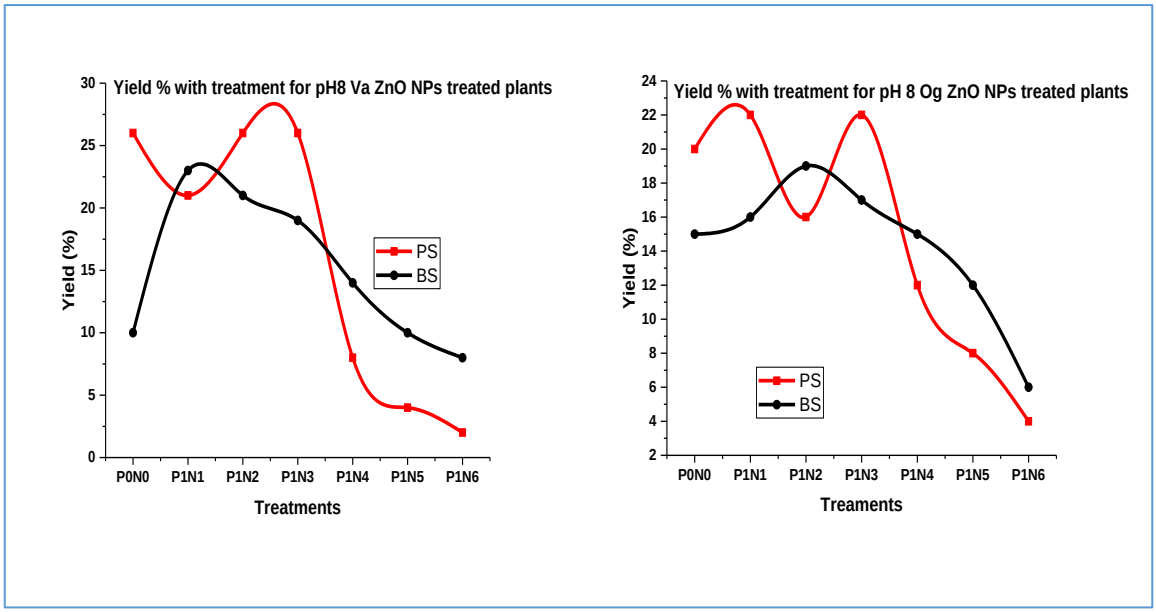


**Figure 7.13** pH 8 zinc oxide nanoparticles effect on yield for BS and PS A. cruentus

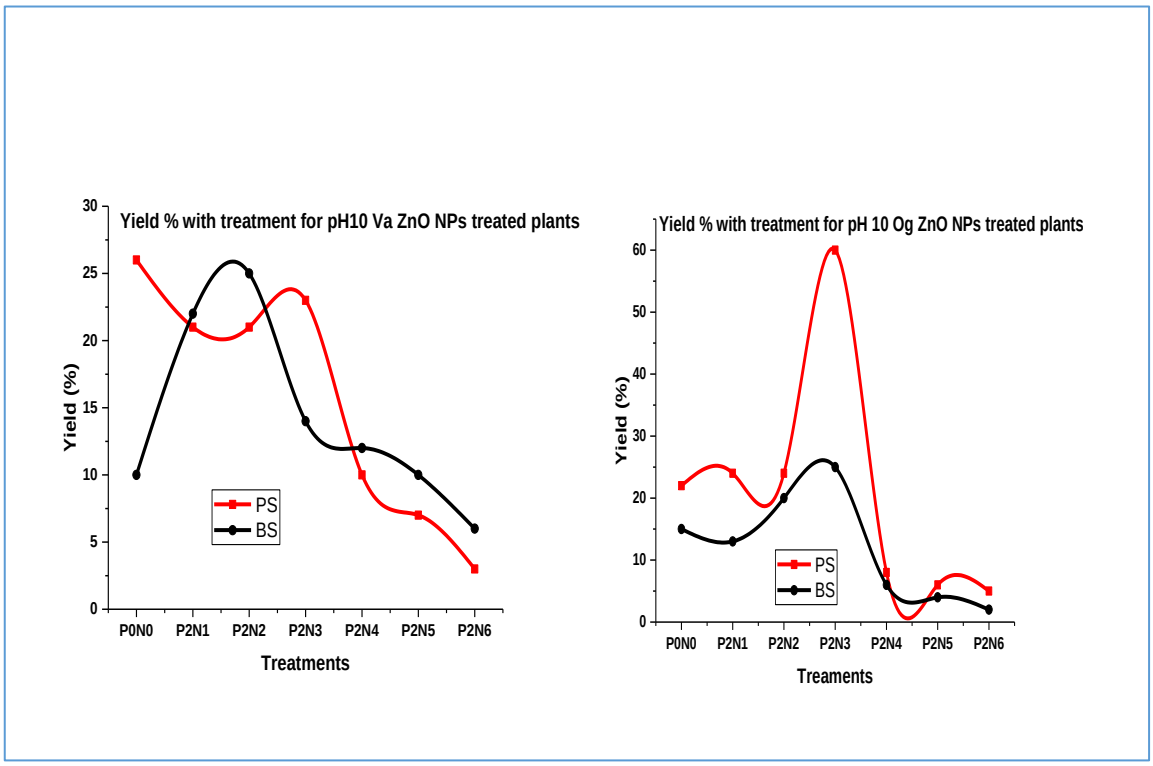


**Figure 7.14** pH 10 zinc oxide nanoparticles effect on yield for BS and PS *Amaranthus cruentus*

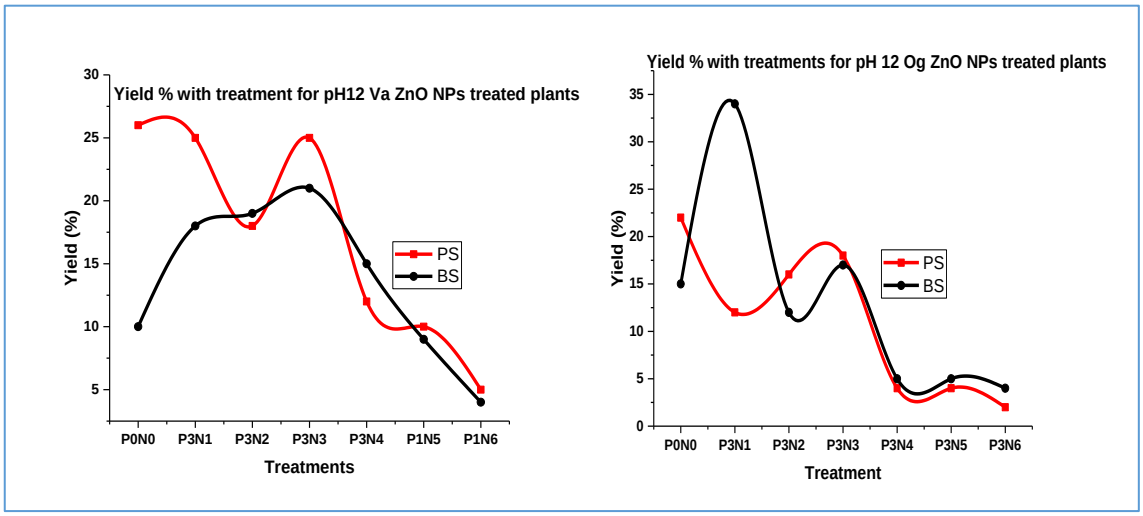


**Figure 7.15** pH 12 zinc oxide nanoparticles effect on yield for BS and PS *Amaranthus cruentus*

## 7.7 Conclusions

The study on the response of the Amaranthus cruentus seedling characteristics and vegetative growth to the different zinc oxide Nano fertilizer treatments showed some interesting results. In most cases, the treated seeds/plants showed improved characteristics over the control (P0N0) which were not treated with the zinc oxide nanoparticles.

The pale-seeded variety had higher Emergence percent than the black-seeded variety and a high concentration of the ZnO Nano fertilizer reduced the E % of both seed varieties. A high concentration of the Og ZnO nanoparticles synthesized at all three pH levels increased the Emergence Index (EI) values. From the ERI analysis, the Va ZnO Nano fertilizer gave a better value for the pale-seeded variety than the Og ZnO nanofertilizer. The results of the seedling characteristics show that key factors to be mindful of while using the ZnO nanofertilizer are the pH of synthesis of the nanoparticles and therefore their sizes. The concentration of the colloidal ZnO Nano fertilizer used is also a feature to watch out for as high concentrations of the nano fertilizer did not favour these growth parameters. While good uniformity of growth of the Amaranthus Cruentus plants are achievable with low concentrations of Og ZnO Nano fertilizer, faster plant growth can be achieved using Va ZnO Nano fertilizer and this obviously should be the choice of any serious-minded farmer.

The vegetative growth results showed that low concentrations of pH 8 ZnO Nanoparticles when used as fertilizer produced taller plants. The pale-seeded variety given the Og ZnO nanofertilizer had narrow leaves however, low concentration of the pH 10 ZnO nanofertilizer gave the PS variety the best yield of 60 %. Though the black-seeded variety produced more leaves, it was shorter and had a lower yield. For any researcher who might be interested in extending this work, the concentration of the nanoparticles used should be carefully chosen depending on the parameters of interest. This work could also be extended to investigate the toxicity levels of the used ZnO Nano fertilizer in the Amaranthus cruentus plant leaves in order to advise prospective consumers.

# Chapter 8

## 8.1 Conclusions and recommendations for further work

### 8.1.1 Conclusions

Silver and zinc oxide nanoparticles biosynthesized using Ocimum gratissimum (Og) and Vernonia amygdalina (Va) plant leaf extracts were characterised using optical spectroscopy and electron microscopy. The nanoparticles which were predominantly spherical though with some agglomeration had varied sizes which were plant leaf extract dependent. The silver and zinc oxide nanoparticles from their XRD scans were found to have good crystalline structure and while the silver nanoparticles had the FCC structure, the zinc oxide nanoparticles had the hexagonal wurtzite structure. Their FTIR spectra revealed the presence of some biomolecules among whom were flavonoids, phenols and some reducing sugars thought to have aided in the production of the nanoparticles.

The Og and Va silver nanoparticles had surface Plasmon resonance in the range 437 – 440 nm which falls within the range reported by available literature from similar researches. While the Og silver nanoparticles had a peak absorbance which increased steadily with time and concentration of the precursor material ($AgNO_3$), the Va silver nanoparticles did not sustain the increase in absorbance with time because after 48 hrs its peak absorbance dropped with a slight shift towards longer wavelengths, a behaviour which is probably due to some instability in the nanoparticle solution and maybe some aggregation of smaller nanoparticles into larger ones.

The zinc oxide nanoparticles SEM images showed that it was in clusters, a feature which Ikono et al[161] say is an indication of its purity and which Moazzen et al[163] report could make them useful in surface acoustic wave (SAW) devices. Colloidal

solutions of different concentrations of the ZnO nanoparticles was used as nanofertilizer for planting the pale-seeded (PS) and black-seeded (BS) varieties of Amaranthus cruentus seeds and its seedling characteristics as well as its vegetative growth were studied over a period of five weeks.

The pale seeded variety had the best percent emergence, Emergence index and Emergence rate index results while the control (P0N0) showed worst seedling characteristics. Though the black seeded plants had broader leaves, they were shorter and produced a lower yield percent. In contrast, the pale seeded variety treated with low concentrations of the pH 10 zinc oxide nanoparticles were taller. Though for most treatments, the PS variety had narrow leaves, they were taller and had the highest yield percent of 60 %. This result agreed with the observations of the seedling characteristics

In general, the ZnO Nano fertilizer improved the growth parameters of the *Amaranthus cruentus* when compared with the control which had no nanoparticle treatment. It was also observed that the nanofertilizer concentrations greater than 500 mg/L had adverse effect on the plant growth, thwarting its growth in some cases and producing some yellow leaves (Chlorosis) in others. Thus, in using these ZnO nanoparticles as nanofertilizer, their sizes, pH of synthesis as well as the concentration of their colloidal solutions are factors to be mindful of. Furthermore, the toxicity level of the ZnO nanofertilizer in the leaves of the Amaranthus cruentus plants grown needs to be determined to ascertain how safe it is for prospective consumers. The electrodeposition studies showed that the plant leaf extracts played a role in the morphology of the produced silver thin films. Silver films deposited on the gold in the presence of the plant leaf extracts as the AFM images show, had more refined and uniform grains than the control with the Og silver average film thickness greater than the Va silver average film thickness. Furthermore, the Va silver film had smaller grains and a higher surface roughness than the Og silver film which had larger grains with a lower surface roughness.

### 8.1.2 Recommendations for further work

In view of the key findings reported, the following are the recommendations for further work:

- The silver nanoparticles could be made using plant leaf extract of a higher concentration than what this work used.
- For the ZnO nanofertilizer experiment, the toxicity level of the ZnO nanoparticles in the Amaranthus plant leaves should be studied to know if it is safe for human consumption and another soil analysis could be done after harvesting the plants to see if the zinc constituent in the soil changed. This might then give an idea of how much the plants actually used.
- The electrodeposition side experiment with the aging solution could be explored with aging times ranging from 30 mins to 120 mins and the morphology of the silver film produced could be compared with that produced immediately after leaf extract addition. Furthermore, more explanation should be sought for the two oxidation peaks produced during the CV of the aged solution.

# Bibliography

[1] Sabir S, Arshad M and Chaudhari S.K (2004) Review Article: Zinc oxide nanoparticles for revolutionizing Agriculture: Synthesis and Applications. Hindawi Publishing corporation. The scientific world journal Vol. 2014 Article ID 925494: 1-8

[2] Kittel C, (1996) Introduction to Solid State Physics 7th Edition: 176-179 *s*

[3] Fundamentals of Semiconductor Physics. Energy Bands. www.optique-ingenieur.org/en/courses.. Visited 12/2/2017

[4] Ibach H., Lüth H., Solid-State Physics An Introduction to Principles of Materials Science Chapter 6 pg 135 Springer Dordrecht Heidelberg London New York 2009

[5] Ashcroft N.W., and Mermin N.D., Solid State Physics. Holt –Saunders International Editions: Philadelphia 1976

[6] Habil I, Zimmermann H, (2000), Basics of optical emission and Absorption-Springer Chapter1 Integrated silicon optoelectronics PHOTONICS vol 3: 1-10

[7] Paranthaman M.P., Wong-Ng W., Bhattacharya R.N., Semiconductor Materials for Solar Photovoltaic cells Springer international publishing Switzerland 2016

[8] Rodriguez JA, Wang X, Hanson JC and Liu G (2003) The behaviour of mixed-metal oxides: Structural and electronic properties of $Ce_{1-x}Ca_xO_2$ and $Ce_{1-x}Ca_xO_{2-x}$ journal of Chemical Physics 119,5659

[9] Rodriguez JA., Chaturvedi S., Kuhn M., Hrbek J. (1998) Synthesis, Properties and Applications of Oxide Nanomaterials J Phys.Chem B 102,5511

[10] Skudrzyk E (1971) Reflection and Transmission of plane waves at normal incidence. In: The Foundation of Acoustics. Springer, Vienna: 295-312. https://doi.org/10.1007/978-3-7091-8255-0_16. Visited 10/01/2018

[11] Reflection and refraction of a plane wave at oblique incidence. https://courses .physics.ucsd.edu/2011…Visited 10/01/2018

[12] Electronic Polarisation of a water molecule. A combined Quantum Chemical and Statistical mechanical treatment. J Phys. Chem, 1996, 100(45): 17791-17796

[13] Pinchuk A, Plessen G.V, Kreibig U (2004) Influences of interband electronic transitions on the optical absorption in metallic nanoparticles. J Phys D Appl.Phys 37(22):3133-3139

[14] Harikoshi Satoshi and Serpone Nick Introduction to Nanoparticles. Microwaves in Nanoparticle synthesis 1st Edition 2013 Wiley-VCH Verlag GmbH &Co KGaA9

[15] Yao Y., Yi B., Xiao J., and Li Z., (2007) Localised surface plasmon resonance spectroscopy and sensing Annual review of Physical Chemistry 58: 267-297

[16] Horikoshi S, Serpone N, Microwaves in Nanoparticle Synthesis First Edition, 2013 Published by Wiley-VCH Ver lag GmbH& Co. KG$\alpha$A. Chapter 1- Introduction to Nanoparticles:1-24

[17] Schaadt D.M, Feng B, Yu E.T, (2005) Enhanced semiconductor optical absorption via surface plasmon excitation in metal nanoparticles. Applied Physics Letters 86, 06 3106

[18] Englebienne P., Hoonacker A.V and Verhas M., (2005) Surface plasmon resonance: principles, methods and applications in biomedical sciences spectroscopy 17, 255-273

[19] Willets K.A, Van Duyne R.P (2007) Localised surface plasmon resonance spectroscopy and sensing Annual Review of Physical Chemistry58: 267-297

[20] Agrawal A, Kriegel I, Milliron D.J., (2015) Shape dependent field enhancement and plasmon resonance of oxide Nanocrystals. Journal of Physical Chemistry 119, 6227-6238

[21] Yeschchenko O.A, Dmitruk I.M, Alexeenko A.A, Kotko A.V, Verdal J, Pinchuk A.O (2012) Size and Temperature effects on the surface plasmon resonance in silver Nanoparticles 7(4): 685-694

[22] Kelly K.L, Coronado E., Zhao L.L., and Schatz G.C., (2003) The optical properties of metal nanoparticles: The influence of size, shape and dielectric environment. J Phys Chem B 107(3): 668-677

[23] Novo C., Alison M. et al (2007) Influence of the medium refractive index on the optical properties of single Gold triangular Prisms on a substrate Journal of Physical Chemistry C Vol 112(1):3-7

[24] Kulkarni S.K, Nanotechnology: Principles and Practises, Capital publishing company, 2007: 72

[25] Shinde K.N., Dhoble S.J., Swart H.C., (2012) Phosphate phosphors for solid state lighting 41. Chapter 2Springer series in Material Science 174 http//doi 10.1007/978-3-642-34312-4-s2: 41

[26] Toney E.J., (2002) Characterization of materials- Photoluminescence spectroscopy. http//doi.org/10.1002/0471266965.com 058. John Wiley and sons.

[27] Perkowitz S., (1993) Optical characterization of semiconductors, infrared, Raman and Photoluminescence spectroscopy. Vol 14, first edition Academic press: 23-32s

[28] Dispersion relations and phonons. Condensed Matter Physics. Rudi Winter's web. User.aber.ac.uk/ruw/teach/334 visited 06/02/2019

[29] Hookes' law. www.chem.ucla.edu/~harding/IGOC/H/hookes_lawhtml visited 10/08/2018

[30] Guinier A, (1963) X-Ray Diffraction, Chapter 1, University of Paris. W.H. Freeman and Company, San Francisco

[31] Stephen R., Rice B.S.A., Ross J., (2000) Physical Chemistry. Chapter 3 (the solid state) Oxford University Press 2nd Edition.

[32] Vitalij K.P and Zavalij P.Y (2005) Fundamentals of powder diffraction and structural characterisation of materials. Springer

[33] B.D Cullity, Elements of X-ray Diffraction, Addison Wesley Reading MA, 1978

[34] D.S. Balaji, S. Basavaraja, R. Deshpande, D. Bedre Mahesh, B.K. Prabhakar, A. Venkataraman (2009) Extracellular biosynthesis of functionalized silver nanoparticles by strains of *Cladosporium cladosporioides* fungus Colloids Surf. B Biointerf., 68 : 88-92

[35] Barna A., Pécz B., (1989) TEM sample preparation by ion milling/amorphization. Elsevier Micron Vol 30(3): 267-276.

[36] Rao D.V.S., Muraleedharan K, Humphreys C.J., (2010) TEM specimen preparation techniques Microscopy: Science, Technology, Applications and Education:1232-1244.

[37] Kim H.J., Choi S.H., Bae H-B and Lee T.W., (2012) Transmission electron Microscopy (TEM) sample preparation of $Si_{1-x}Ge_x$ in c-plane Sapphire substrate.

[38] Makowiecka M., Kepinski L., and Jurczy K.M., (2008) Nanoscale Hydrogen Storage Materials studied by TEM. Rev Adv. Mater.Sci 18(2008):621-626.

[39] A. N Mallika, A.R Reddy, K.V Reddy. Annealing effects on the Structural and optical properties of ZnO nanoparticles with PVA and CA as chelating agents. Journal of Advanced ceramics 4(2), 123, (2015) doi:10.1007/s40145-015-0142-4

[40] Sun Y., (2012) Watching nanoparticles Kinetics in liquid. Materials today, Vol15(4): 140-147

[41] Jones P.F., (1975) New applications of Photoluminescence Techniques for Forensic Science. Forensic Science, Chapter 19: 183-196.

[42] Ibach H., Lüth H., (2009) Solid State Physics. An introduction to principles of Materials Science 4th Edition, Springer Dordrecht Heidelberg. London.

[43] Greivenkamp, J.E., (2004) Field guide to Geometrical Optics Vol FG01 Bellingham, WA: SPIE The international Society for Optical Engineer.

[44] Toney J.E., Photoluminescence Spectroscopy (2002) https://doi.org/10.1002/0471266965.com058

[45] Trupke T., Mitchell B., Weber JW, McMillan W., Bardes RA, and Kroeze R. (2012) Photoluminescence imaging for photovoltaic applications. Energy Procedia Elsevier 15(2012): 135-146

[46] Smith B.C. Fundamentals of Fourier Transform infrared spectroscopy, CRC press, 1996

[47] Staurt B, Modern infrared Spectroscopy, Wiley, New York, 1996

[48] Griffiths P.R, De Haseth J, A, Fourier Transform Infrared spectroscopy, Wiley, New York, 1986

[49] Infrared Spectroscopy Absorption Table https://chem:libretexts.org(visited 15/12/2015)

[50] IR Absorption Table-webspectra https://webspectra.chem.ucla.edu/irtable.html (visited 27/01/2016).

[51] Bhambhani A., Middaugh C.R., (2012) A formulation method to improve the physical stability of macromolecular based drug products:

[52] Technology:DynamicLightScatteringhttps;//ls instrument.ch/en/technology/dynamic-light-scattering-dls. Visited 10/01/2018

[53] Kholodenko A.L., Douglas JF (1995) Generalised Stokes-Einstein equation for spherical particle suspensions, physical review E Vol 51(2):1081-1090

[54] Patravale V., Dandekar P., Jain R., (2014) Nanoparticle Drug delivery Chapter 3 Characterization techniques for nanoparticulate carriers, 1st Edition. Woodhead publishing

[55] Eshuis A., Harbers G., Doornink D.J., and Mynlieff P.F (1985) Experimental Determination of particle size distributions in colloidal systems by Dynamic light scattering. Application to Polystyrene Latex Spheres and to Nonionic Micro emulsions. American Chemical Society. Langmuir 1985 1: 289-293

[56] Lim J., Yeap S.P., Che H.X., Low S.C., (2013) Characterisation of magnetic nanoparticles by dynamic light scattering. Nanoscale Research Letters 8(1):1-14

[57] Williams P. M., Oatley-Radcliffe D.L., and Hilal N (2017) Membrane Characterisation 1st edition Chapter 17 Feed solution Characterisation : 379-404

[58] Kestell A.E., De Lorey G.T., (2010) Nanoparticles: Properties, Classification, Characterisation and Fabrication. Nanotechnology, Science and Technology. Nova science Publishers Chapter5:17-41

[59] Guiner A., (1963) X-Ray Diffraction In crystals, imperfect crystals and Amorphous Bodies W.H Freeman and Company Printed in USA.

[60] Pecharsky V.K., and Zavalij P.Y. (2005) Fundamentals of powder diffraction and structural Characterisation of Materials. Springer 2005 ISBN 0-387-24147-7

[61] Kalska-Szostko B, Electrochemical Methods in Nanomaterials preparation in Recent trend in Electrochemical Science and Technology InTech, 2012

[62] Dobre, N., Golgovici F., Anicai L., Buda M. (2014) Cyclic Voltammetry of Silver Nanoparticles on Platinum, Gold and Glassy Carbon Electrodes. REV. Chim (Bucharest) 2014. **65**(5): p. 578-581.

[63] Kasem KK, Platinum as a reference electrode on electrochemical measurements . Platinum Metals Rev, 2008,52(2):100 doi: 10.1595/147106708x297855

[64] Chen R, et al, Use of Platinum as the counter electrode to study the activity of non precious metal catalysts for the hydrogen evolution reaction, ACS energy letters, 2017,2: 1070-1075

[65] Brett C.M.A., Brett A.M.O Electrochemistry principles, methods and applications. Oxford University Press Eds, 1993

[66] Bockris J., Khan S.U.M Surface electrochemistry: A molecular level approach.

[67] Staikov G (2007) Electrocrystallization in Nanotechnology. WILEY-VCH Verlag GmbH &Co KGaA, Weinheim

[68] Schwarzacher, W., Electrodeposition: a technology for the future. Electrochemical Society Interface, 2006. **15**(1): p. 32-33.

[69] Cheng S., Xing D., Call D.F., Logan B.E., (2009) Direct Biological conversion of electric current into Methane by Electromethanogenesis. Environ Sci Technol : 3953-3958

[70] De Oliveira R.R.L., Albuquerque D.A.C., Cruz T.G.S., Yamaji F.M. and Leite F.L. (2012). Measurement of the Nanoscale Roughness by Atomic Force Microscopy: Basic Principles and Applications, Atomic Force Microscopy: 147-174

[71] Nanosurf Easyscan 2 (www.nanosurf.com) Your modular scanning Probe Microscopy system

[72] Prabhu KS, Lobo R, Shirwaikar AA, and Shirwaikar A (2009) Ocimum gratissimum*:* A Review of its chemical, Pharmacological and Ethnomedicinal Properties The open complementary medicine journal 1: 1-15

[73] Adebolu T.T., Salau A.O., (2005) Antimicrobial activity of leaf extracts of Ocimum gratissimum on selected diarrhoea causing bacteria in South western Nigeria African Journal of Biotechnology Vol. 4 (7), pp. 682-684, July 2005

[74] Bukar A.M, Isa M.A., Bello H.S., Abdullahi A.S., (2013) Antibacterial Activity of Aqueous and Ethanolic Leaf Extracts of Vernonia Amygdalina On Selected Species of Gram Positive And Gram Negative Bacteria. International Journal of Environment Vol 2 (1): 147-152

[75] Rabelo M, Souza EP, Soare PMG (2003) Antinociceptive properties of the essential oil of Ocimum gratissimum L (Lubiatae) in mice, Braz. J Med. Biol. Res 2003:36:521-524

[76] Kabir O.A, Olukayode O, Chidi E.O, Ibe Christopher C I, and Kehinde A.F (2005) Screening of crude extracts of six medicinal plants used in South-West Nigeria unorthodox medicine for anti-methicillin resistant Staphylococcus aureus activity. BMC complementary and Alternative Medicine 5:6: 1-7

[77] Dakole J.B.L., Leth C.D., Vismer H.F., Torp J, Guemdjom E.F.N., Mbeffo M, Tangue O, Fotio D, Zollo PHA, Nkengfack AE (2009) Food preservative potential of essential oils and fractions from Cymbopogon citratus, Ocimum gratissimum and Thyinus vulgaris against mycotoxigenic fungi. International journal of food microbiology,131:2-3:151-156

[78] Effraim KD, Jacks TW, Sodipo OA (2003) Histopathological studies on the toxicity of Ocimum gratissimum leave extract on some organs of rabbit. Afr. J Biomed. Res 2003:6:21-24

[79] Ijeh II, Omodamiro OD, Nwanna IJ (2005) Antimicrobial effects of aqueous and ethanolic fractions of two species Ocimum gratissimum and Xylopia aethiopica. Afr. J. Biotech 4: 953-956

[80] Orafidiya l. O., Adesina S.K, Igbeneghu O.A., Akinkunmi E.O., Adetogun G.E., Salau A.O. (2006) The effect of honey and surfactant type on the antibacterial properties of the leaf essential oil of Ocimum gratissimum Linn against common wound-infecting organisms. Int. J Aromatherapy 16:57-62

[81] Udochukwu U, Omeje FI, Uloma IS, Oseiwe FD (2015) Phytochemical analysis of Vernonia amygdalina and Ocimum gratissimum extracts and their antibacterial activity on some drug resistant bacteria American journal of research communication 3(5): 225-235

[82] Ugwoke C.E.C, Nzekwe U, Ameh G.I (2010) Phytochemical constituents and ethnobotany of the leaf extract of bitter leaf (Vernonia amygdalina Del Journal of Pharmaceutical and Allied Sciences 7(3):

[83] Inyang E (2003) *Conventional and traditional uses of plants*. Verdict Press Nigeria: 65-90

[84] Momoh MA, Adikwu MU and Oyi AR (2010) Vernonia amygdalina extract and CD4+ cell counts: ''An immune study'' Global Journal of Biotechnology and Biochemistry 5(2): 92-96

[85] Ebong P. E, Atangwho I. J., Eyong E.U., Egbung G.E. (2008) The antidiabetic efficacy of combined extracts from two continental plants: Aradirachta indica (A. Juss) (Neem) and Vernonia amygdalina Del (African bitter leaf) American Journal of Biochemistry and Biotechnology 4(3): 239-244

[86] Sinisi A., Munoz E., Abay S.M., Habluetzel A., Appendino E., Millan E et al, (2016) Poly-electrophilic sesquiterpene lactones from Vernonia amygdalina: new members and differences in their mechanism of thio trapping and in bioactivity. J Nat. Prod. 78(7): 1618-1623

[87] Quasie O., Zhang Y, Zhang H., Luo J., Kong L., (2016) Four new steroid saponins with high oxidized side chains from the leaves of Vernonia amygdalina. Phytochem Lett. 15: 16-20

[88] Farombi EO, Owoeye O, (2011) Antioxidative and chemopreventive properties of Vernonia amygdalina and Garcinia bioflavonoid. International journal of environmental research and public health.8(6): 2533-2555

[89] Erasto P., Grierson D.S., Afolayan A.J., (2007) Evaluation of antioxidant activity and the fatty acid profile of the leaves of Vernonia amygdalina growing in South Africa. Food Chemistry 104: 636-642

[90] Ifeoluwa T.O., Akinbiyi A.A., Aderiike A., Abimbola O.A., Oyetunde T.O. (2018) Vernonia amygdalina: A folkloric herb with anthelminthic properties: Beni-Suef University Journal of Basic and Applied Sciences 7: 43-49

[91] Izevbigie E.B. (2003) Discovery of water-soluble anticancer agents (Edotides) from a vegetable found in Benin city Nigeria. Exp.Biol. Med 228: 293-298

[92] Ghamba PE, Balla H, Goje LJ, Halidu A, Dauda MD (2014) Invitro-antimicrobial activities of Vernonia amygdalina on selected clinical isolates. Int. journal of current microbiology and applies sciences 3(4): 1103-1113

[93] Atangwho I.J., Ebong P.E., Eyong E.U, Williams I.O., Eteng M.U., Egbung G.E (2009) Comparative chemical composition of leaves of some antidiabetic medicinal plants Azadirachta indica, Vernonia amygdalina and Gongronema latifolium. African Journal of Biotechnology 8(18): 4685-4689

[94] Korkina L.G., Afanas'ev I.B. (1997) Antioxidant and Chelating properties of flavonoids. Adv. Pharmacol 38:151-163

[95] Ho W.Y., Liang W.S., Yeap S.K., Beh B.K., Yousr A.H.N., Alitheen N.B (2013) Invitro and in vivo antioxidant activity of Vernonia amygdalina water extract. African Journal of Biotechnology 11(17) :4090-4094

[96] Srivastava N., Bezwada R. (2015) Flavonoids: The Health Boosters White paper. Hillsborough NJ: Indofine Chemical company

[97] Wang H.K., Xia Y., Yang Z.Y., Natschke S.L., Lee K.H. (1998) Review: Recent advances in the discovery and development of flavonoids and their analogues as antitumor and anti-HIV agents. Adv. Exp. Med. Biol. 439: 191-225

[98] Ren W., Qiao Z., Wang H., Zhu L., Zhang L (2003) Review: Flavonoids promising anticancer agents. Med. Res.Rev. 23(4): 519-534

[99] Egorova E.M., Revina A.A., (2000) Synthesis of metallic nanoparticles in reverse micelles in the presence of quercetin. Colloids Surf. A Physicochem Eng. Asp. 168: 87-96

[100] Yasin S., Liu L., Yao J. (2013) Biosynthesis of silver nanoparticles by Bambo leaves extract and their antimicrobial activity. Journal of Fibre Bio engineering and informatics 6(1):77-84

[101] Croteau R., Kulchan T.M., Lewis N.G. (2000) Natural products (secondary metabolites) in Biochemistry and Molecular Biology of plants pp 1250-1318 (Buchanan B., Gruissem W and Jones R Editors) Rockville, MD American Society of Plant Biologists.

[102] Dixon R.A., Pasinetti G.M (2010) Flavonoids and Isoflavonoids from plant Biology to Agriculture and neuroscience plant physiol. 154(2): 453-457

[103] Mittal A.K., Chisti Y., Banerjee U.C (2013) Synthesis of metallic nanoparticles using plant extracts. Elsevier Biotechnology Advances 13(2): 346-356

[104] Dubey M., Bhadauria S., Kushwah B (2009) Green synthesis f Nano silver particles from extract of Eucalyptus hybrid (safeda) leaf. Dig.J. Nanomater. Biostruct. 4: 537-543

[105] Huang J.L., Li Q.B., Sun D.H., Lu Y.H., Su Y.B., Yang X et al (2007) Biosynthesis of Silver and Gold nanoparticles by novel sundried Cinnamomum camphora leaf. Nanotechnology 18, 2007.

[106] Marchiol L, Synthesis of metal nanoparticles in living plants, Italian Journal of Agronomy, Vol 7: e 37 pp 274-282, 2012

[107] Hsin-I Peng, Miller BL (2011) Recent advancements in optical DNA biosensors: exploiting the plasmonic effects of metal nanoparticles Analyst 136: 436-447

[108] Selid PD, Hanying X, Collins EM, Zhao JX (2009) Sensing Mercury for biomedical and Environmental monitoring. Sensors 2009(9):5446-5459 doi:10.3390/s90705446

[109] Horikoshi S, Serpone N, Microwaves in Nanoparticle Synthesis First Edition, 2013 Published by Wiley-VCH Ver lag GmbH& Co. KG$\alpha$A. Chapter 1- Introduction to Nanoparticles:1-24

[110] Cristiana B, Ivan I, Blandino P and Robbie K (2007) Nanomaterials and nanoparticles: Sources and Toxicity. Biointerphases 2(4): 1-103

[111] Rajput N, (2015) Methods of preparation of Nanoparticles – A review. International journal of Advances in Engineering and Technology 7(4): 1806-1811

[112] Vithiya K, Sen S (2011) Biosynthesis of Nanoparticles. International Journal of Pharmaceutical Sciences and Research 2(11): 2781-2785

[113] Malik P, Shankar R, Malik V, Sharma N, Mukherjee TK (2014) Green chemistry based benign routes for nanoparticle synthesis J. nanopart. 2014: doi:10.1155/2014/302429

[114] Li X, Xu H., Chen Z-S., Chen G., (2011) Biosynthesis of nanoparticles by microorganisms and their applications. Article ID 270974: 1-16

[115] Shah M, Fawcett D, Sharma S, Tripathy SK (2015) Green synthesis of metallic nanoparticles via biological entities. Materials 2015, 8(11):7278-7308

[116] Emeka EE, Ojiefoh OC, Aleruchi C, Hassan LA, Owoseni CM, Mfon R, Dare EO, Adesuji ET (2014) Evaluation of antibacterial activities of silver nanoparticles green-synthesized using pineapple leaf (Ananas comosus) 2014(57): 1-5

[117] Moghaddam K.M., (2010) An introduction to microbial metal nanoparticles preparation method. J Young invest. 19(19): 1-6

[118] Vithiya K., Sen S., (2011) Biosynthesis of nanoparticles. International Journal of Pharmaceutical Sciences and Research. IJPSR Vol2(11): 2781-2785

[119] Keat CL, Aziz A, Eid AM, Elmarzugi NA (2015) Biosynthesis of nanoparticles and silver nanoparticles. Bioresources and Bioprocessing 2: 47:1-11

[120] Ahmed S, Ahmad SM, Swami BL Ikram S (2016) green synthesis of silver nanoparticles using Azadirachta indica. aqueous leaf extract. Journal of Radiation research 9(1):1-7

[121] Ahamed M, Alsalhi MS, Siddiqui MKJ (2010) Silver nanoparticles applications and human health. Clinica Chimica acta Elsevier 411(23-24): 1841-1848

[122] Ghiuta I, Cristea D, Munteanu D (2017) Synthesis methods of metallic nanoparticles-An overview. Bulletin of the Transilvania University of Brasov 10(59) No. 2: 133-140

[123] Senapti U. S, Jha D.K. and Sarkar (2013) Green synthesis and characterization of ZnS nanoparticles Res.J. physical sci 1(7): 1-6

[124] Panigrahi S, Kundu S, Ghosh S, Nath S, Pal T, (2004) General Method of synthesis for metal nanoparticles. Journal of Nanoparticle Research 6(4):411-414

[125] Nikam A.V, Prasad B.L.V and Kulkarni A.A (2018) Wet chemical synthesis of metal oxide nanoparticles: a review. CrystEngComm 20(35):5091-5107

[126] Pascal C, Pascal J.L, Favier F, Moubtassim M.L.E, Payen C. (1999) Electrochemical synthesis for the control of Y-$Fe_2O_3$ Nanoparticle size, Morphology, microstructure and magnetic behaviour. Chem.Mater 11(1):141-147

[127] Cabrera L, Gutierrez S, Menendez I N. Morales M.P, Herrasti P, Magntite nanoparticles: electrochemical synthesis and characteristics. Electrochim Acta, 53(8)3436-3441

[128] Hanim M.A, A. Electroless Plating as Surface Finishing in Electronic Packaging Comprehensive Materials Finishing (Elsevier) Vol3, 2017 :220-229

[129] Tierno P, Goedel W.A (2006) Using electroless deposition for the preparation of Micron sized polymer/metal core/shell particles and Hollow metal spheres. Journal of Physical Chemistry B 110(7): 3043-3050

[130] SENSBIOSYN (Biosensors and sensors for the industrial biosynthesis process of widely used commercial antioxidants: nutraceuticals as additives for food and aquaculture promoting. http://www.sensbisyn.com. Visited 4/9/18

[131] Harper A and Anderson M.R. Electrochemical Glucose Sensor-Developments using electrostatic assembly and carbon nanotubes for Biosensor construction. Sensors 2010, 10: 8248-8274 doi:10:3390/s 100908248

[132] Li X, Xu H, Chen Z-S, and Chen G (2011) Biosynthesis of nanoparticles by microorganisms and their applications Journal of Nanomaterials 2011(2011):1-16

[133] Singh P, Kim Y-J, Zhang D, Yang D-C (2016) Review: Biological synthesis of nanoparticles from plants and microorganisms. Trends in Biotechnology 34(7):588-599

[134] Saxem A, Tripathi RM, Zafar F, Singh P (2012) Green synthesis of silver nanoparticles using aqueous solution of Ficus benghalensis leaf extract and characterization of their antibacterial activity. Material letters 67(2012):91-94

[135] Iravani S (2011) Green synthesis of metal nanoparticles using plants. Green chem 13:2638-2650 doi:10.1039/C1GC15386B.

[136] Makarov VV, Love AJ, Sinitsyna OV, Makarov SS, Yaminsky I.V, Taliansky ME and Kalinina NO (2014) Green Nanotechnologies: Synthesis of metal nanoparticles using plants. Acta Naturae 6(1): 35-44

[137] Mohammad V, Umar A, Hahn Y-B, (2010) *ZnO Nanoparticles; Growth, Properties and Applications.* Metal oxide and nanostructures and their applications Chapter 4, American Scientific Publishers: 1-36

[138] Patil RS, Mangesh KR, Sanjay SK, Bioinspired synthesis of highly stabilized silver nanoparticles using Ocimum tenuiflorum leaf extract and their antibacterial activity, Elsevier Spectrochemica Acta part a; Biomolecular spectroscopy 91: 234-238, 2012

[139] Espitia P., Otoni C.G. et al, (2012) ZnO nanoparticles: Synthesis, Antimicrobial activity and food packaging applications. Food and Bioprocess Technology Vol 5(5): 1447-1464 Espitia PJP, Soares N.F.F Combra JSR et al https:// doi.org/10.1007/s 11947-012-07976-6

[140] Hossain MK, Minelli A, Sadaf F, Ulfa M (2014) Synthesis and Optical Characterization of morphologically different ZnO nanoparticles and their interaction with hydrogen, nan. O mat. Master, pp 1-11, 2014

[141] Soosen S.M, Bose L, George K.C (2009) Optical properties of ZnO Nanoparticles SB Academic review XVI (1,2): 57-65

[142] Quin L, Shing C, Sawyer S, Dutta P (2011) Enhanced ultraviolet sensitivity of zinc oxide nanoparticle photoconductors by surface passivation Optical materials Elsevier 33: 359-362

[143] Tejaswi T, Rao KV, Chakara CS, Silver nanoparticles synthesis and stabilization by different species of Ocimum and characterization for its antimicrobial activity, Impressco International Journal of current Engineering and Technology vol 3(2) pp 501-506, 2013

[144] Dare EO, Oseghale CO, Labulo AH, Adesuji ET, Elemike EE, Onwuka J, Bamgbose T, Green synthesis and growth kinetics of nanosilver, Springer J. Nanostruct. Chem (5) pp 85-94, 2014

[145] Abdulsalam H, Sivarag R, Venckatesh R, Green synthesis and characterisation of ZnO nanoparticles from Ocimum basilicum L, Infona Material letters Vol 131, pp16-18, 2014

[146] Nweze ET, Eze E, Justification for the use of Ocimum gratissimum L in herbal medicine and its interaction with disc antibiotics, BMC Complementary and Alternative medicine (91) pp 37, 2009

[147] Alias S.S, Ismail A.B, Mohamad A.A (2010) Effect of pH on ZnO nanoparticle properties synthesized by Sol-Gel centrifugation. Journal of Alloys and Compounds (Elsevier) 499(2010): 231-237

[148] Oskam G (2006) Metal oxide nanoparticles: Synthesis, Characterization and Application. Journal of Sol-Gel Science and Technology 37(3):161-164

[149] Singhal G, Bhavesh R, Kasariya K, Sharma A.R, and Singh R.P (2011) Biosynthesis of silver nanoparticles using Ocimum sanctum (Tulsi) leaf extract and screening its antimicrobial activity. Journal of Nanoparticle Research 13(7) 2981-2988

[150] Castro L, Blazquez M.L, Munoz J. A, Gonzalez F.G and Ballester A (2014) Mechanism and applications of metal nanoparticles prepared by bio-mediated process Reviews in Advanced Sciences and Engineering 3(3):199-216

[151] Liqiao Q, Christopher S, Sawyer S, Dutta P.S (2011) Enhanced ultra-violet sensitivity of Zinc oxide nanoparticles photoconductors by surface passivation. Elsevier Optical Materials (933): 359-362

[152] Koch U., Fojtik A., Weller H., Henglein A., (1985) Photochemistry of semiconductor colloids preparation of extremely small ZnO par-SAO/NASA ADS. Chemical Physics Letters, Vol122(5): 507-510

[153 Koao l. F, Dejene F.B, Swart H.C (2015) Effect of pH on the properties of ZnO nanostructures prepared by chemical bath deposition method 56th Proceedings of South Africa Institute of Physics: 43-48

[154] Alias S.S, Ismail A.B, Mohamad A.A(2010) Effect of pH on ZnO nanoparticle properties synthesized by Sol-gel centrifugation journal of Alloys and compounds (Elsevier) 499(2010):231-237

[155] Heo S.N, Park K.Y, Seo Y.J, Ahmed F, Anwar M.S, Koa B.H (2013) Effect of solution concentration on the functional properties of ZnO nanostructures: Role of Hexamethylenetetramine. Electronic materials letters 9(3):261-265

[156] Debanath MK, Karmakar S (2013) Study of blueshift of optical band gap in zinc oxide (ZnO) nanoparticles prepared by low – temperature wet chemical method. Materials letters 111(2013):116-119

[157] Pholnak C., Lertworapreecha M., Sirisathitkul C., Suwanboon S (2016) Antibacterial and physical properties of ZnO with pH – sensitive morphology. Journal of experimental Nanoscience Vol 11(7):1320-1330

[158] Sangeetha G, Rajeshwari S, Venckatesh R (2011). Green synthesis of zinc oxide nanoparticles by aloe barbadensis miller leaf extract: Structure and optical properties. Mater. Res. Bull. 46(12):2560-2566.

[159] Chithra M.J., Sathya M., Pushpanathan K. (2015) Effect of pH on crystal size and photoluminescence property of ZnO nanoparticles prepared by chemical precipitation method. Acta metallurgica sinica (English Letters) 28(3): 394-404 doi:10.1007/s40195-015-218-8

[160] Montenegro D.N, Hortelano V, Martinez O., Martinez-Tomas M.C., et al (2013) Non-radiative recombination centers in catalyst-free ZnO nanorods grown by atmospheric-metal organic chemical vapour deposition. Journal of Physics D: Applied Physics Vol 46(23)

[161] Ikono R., Amalia P.R., et al, (2012) Effect of pH variation on particle size and purity of Nano zinc oxide synthesized by Sol-Gel Method. International Journal of Engineering & Technology IJET Vol12(6): 5-9

[162] Sabir S, Mohammad A, Chaudhari SK (2014) Zinc oxide nanoparticles for revolutionizing Agriculture: synthesis and Applications (ID 025494) Hindawi Publishers pp 1-8, 2014

[163] Moazzen MAM, Borghei SM, Taleshi F (2013) Change in the morphology of ZnO nanoparticles upon changing the reactant concentration Appl Nanosci (2013) 3; 295-302

[164] Mohanty U.S (2011) Electrodeposition: a versatile and inexpensive tool for the synthesis of nanoparticles, nanorods, nanowires, and nanoclusters of metals. J Appl Electrochem 41:257-270 doi 10.1007/s10800-010-0234-3

[165] Schwarzacher, W., Electrodeposition: a technology for the future. Electrochemical Society Interface, 2006. **15**(1): p. 32-33.

[166] Mustatea G., Vidal L., Calinscu L (2015) A phytochemical approach designed to improve the coating of nanoscale silver films onto plastic wrappings intended to control bacterial hazards. Journal of Nanoparticle Research (2015):1-12

[167] Silver particle films photochemically generated on food packaging materials enhance antibacterial activity. Centre for Nanotechnology in Society, Arizona State University. http://nice.asu.edu/nano/silver-particle-films..visited 14/09/2018

[168] Meenakshi R (2016) Pickling inhibitor to electroplating: A plant extract. International journal of Advanced Research in Chemical science (IJARCS) 3(1): 7-10

[169] Loto C, Loto R.T (2013) Effect of Nicotiana Tobaccum extract additive on the Quality of electroplating of zinc on mild steel. Polish Journal of Chemical Technology 15(1):38-45

[170] Loto C.A, Olofinjana A, Loto R.T (2014) Effect of Manihot esculenta C leaf extract additive on the zinc electroplating on mild steel in acid chloride solution 9(2014): 3746-3759

[171] Selvi, MT, K Nancy, J Felicita Florence, A study on the effect of pharmacologically active Lawsonia Inermis Linn leaf extract on zinc electrodeposition on mild steel. International journal of research and development in Pharmacy and life sciences, 2015.4(1):1362-1370.

[172] Florence J.F, Rajendran S, Srinivasan K.N (2015) A study on the effect of Lawsonia inermis Linn (Henna) leaf extract on Zinc-Nickel alloy electrodeposition on

mild steel from acid sulphate bath. International journal of innovative science Engineering and Technology 2(11):505-516

[173] Alsultani, KF and Tajaldeen LM, Investigation of Pineapple as addition on the electrodeposition of Zn-n$Al_2O_3$ on Carbon Steel in acidic medium. International journal of chemical Engineering and applications, 2016,7(2):146-150

[174] Beddington, J.R., et al., The role for scientists in tackling food insecurity and climate change. Agriculture & Food Security, 2012. **1**(1): p. 10.

[175] Kochakinezhad, H., et al., A comparison of organic and chemical fertilizers for tomato production. Journal of Organic Systems, 2012. **7**(2): p. 14-25.

[176] Rameshaiah, G., J. Pallavi, and S. Shabnam, Nano fertilizers and nano sensors–an attempt for developing smart agriculture. Int J Eng Res Gen Sci, 2015. **3**(1): p. 2091-2730.

[177] Liu, R. and R. Lal, Potentials of engineered nanoparticles as fertilizers for increasing agronomic productions. Science of the total environment, 2015. **514**: p. 131-139.

[178] Cifuentes, Z., et al., Absorption and translocation to the aerial part of magnetic carbon-coated nanoparticles through the root of different crop plants. Journal of nanobiotechnology, 2010. **8**(1): p. 26.

[179] Prasad, T., et al., Effect of nanoscale zinc oxide particles on the germination, growth and yield of peanut. Journal of plant nutrition, 2012. **35**(6): p. 905-927.

[180] Singh, N., et al., Zinc oxide nanoparticles as fertilizer for the germination, growth and metabolism of vegetable crops. Journal of Nanoengineering and Nanomanufacturing, 2013. **3**(4): p. 353-364.

[181] Venkatachalam, P., et al., Zinc oxide nanoparticles (ZnONPs) alleviate heavy metal-induced toxicity in Leucaena leucocephala seedlings: A physiochemical analysis. Plant Physiology and Biochemistry, 2017. **110**: p. 59-69.s

[182] Lin S, Reppert J., et al, (2009) Uptake, Translocation and Transmission of Carbon Nanomaterials in Rice plants. Small 5(10): 1128-1132. https://doi.org/10.1186/1471-2229-9-45

[183] Corredor ., Testillano P.S., Coronado M.J., et al (2009) Nanoparticle penetration and transport in living pumpkin plants in situ subcellular identification plant Biol. 9, 45

184] Navarro E., Baun A., Behra R Hartmann N.B., Filser J., Miao A.J., et al (2008) Environmental behaviour and ecotoxicity of engineered nanoparticles to algae, plants and fungi. Ecotoxicology 17(5): 372-386

[185] Agrawal S., Rathore P (2014) Nanotechnology Pros and Cons to Agriculture: A review. International journal of current Microbiology and Applied sciences Vol3(3): 43-55

[186] Mishra S., Keswani C., Abhilash P.C., Fraceto L.F., and Singh H.B (2017) Integrated approach of Agri-nanotechnology: Challenges and Future Trends. Frontiers in Plant Scince Vol8. 471:1-12 doi:10.3389/f pls 2017.00471

[187] Zafar, H., et al., Effect of ZnO nanoparticles on Brassica nigra seedlings and stem explants: growth dynamics and antioxidative response. Frontiers in plant science, 2016. **7**.

[188] Venkatachalam, P., et al., Enhanced plant growth promoting role of phycomolecules coated zinc oxide nanoparticles with P supplementation in

cotton (Gossypium hirsutum L.). Plant Physiology and Biochemistry, 2017. **110**: p. 118-127.

[189] Hernandez-Viezcas, J., et al., Spectroscopic verification of zinc absorption and distribution in the desert plant Prosopis juliflora-velutina (velvet mesquite) treated with ZnO nanoparticles. Chemical engineering journal, 2011. **170**(2): p. 346-352.

[190] Mfon R.E, Odiaka N.I., Sarua A (2017) Interactive effect of colloidal solution of zinc oxide nanoparticles biosynthesized using Ocimum gratissimum and Vernonia amygdalina leaf extracts on the growth of Amaranthus cruentus seeds. African Journal of Biotechnology Vol 16(26): 1481-1489

[191] History of Makurdi, location and urban growth www.jotscroll.com/forums/3posts. Visited 10/9/2018

[192] Laware, S. and S. Raskar, Influence of zinc oxide nanoparticles on growth, flowering and seed productivity in onion. Int J Curr Microbiol Appl Sci, 2014. **3**(7): p. 874-881.

[193] Sedghi, M., M. Hadi, and S.G. Toluie, Effect of nano zinc oxide on the germination parameters of soybean seeds under drought stress. Annals of West University of Timişoara, Ser. Biology, 2013. **16**: p. 73-78.

[194] Boonyanitipong, P., et al., Toxicity of ZnO and TiO2 nanoparticles on germinating rice seed Oryza sativa L. International Journal of Bioscience, Biochemistry and Bioinformatics, 2011. **1**(4): p. 282.

[195] Wang, X., et al., Zinc oxide nanoparticles affect biomass accumulation and photosynthesis in Arabidopsis. Frontiers in plant science, 2015. **6**.

[196] Mahajan, P., S. Dhoke, and A. Khanna, Effect of nano-ZnO particle suspension on growth of mung (Vigna radiata) and gram (Cicer arietinum) seedlings using plant agar method. Journal of Nanotechnology, 2011. .

[197] Narendhran, S., P. Rajiv, and R. Sivaraj, Influence of zinc oxide nanoparticles on growth of Sesamum indicum L. in zinc deficient soil. Int J Pharm Pharm Sci, 2016. **8**(3): p. 365-371.

[198] Panwar, J., et al. Positive effect of zinc oxide nanoparticles on tomato plants: A step towards developing nano-fertilizers. in Proceedings of 3rd international conference on environmental research and technology *(ICERT)*. 2012.

[199] Adhikari, T., et al., Characterization of zinc oxide nano particles and their effect on growth of maize (Zea mays L.) plant. Journal of plant nutrition, 2015. **38**(10): p. 1505-1515.

[200] Taheri, M., et al., The effects of zinc-oxide nanoparticles on growth parameters of corn (SC704). STEM Fellowship Journal, 2016. **1**(2): p. 17-20.

[201] Ikono, R., et al., Effect of pH variation on particle size and purity of nano zinc oxide synthesized by Sol–Gel Method. Int J Engl Technol, 2012. **12**: p. 5-9.

[202] Milivojevic M., Ripka Z., Petrovic T.,(2018) ISTA RULES CHANGES IN SEED GERMINATION TESTING AT THE BEGINNING OF THE 21$^{ST}$ CENTURY. Biblid:1821-4487 22:40-45

# Appendix A

**List of Acronyms**

| | |
|---|---|
| TEM | Transmission Electron Microscopy |
| SEM | Scanning Electron Microscopy |
| UV-Vis | Ultraviolet-visible |
| PL | Photoluminescence |
| NUV | Near Ultra-violet |
| He-Cd | Helium Cadmium |
| FTIR | Fourier Transform Infrared |
| XRD | X-ray diffraction |
| DLS | Dynamic Light Scattering |
| AFM | Atomic Force Microscopy |
| SPR | Surface Plasmon Resonance |
| SAW | Surface Acoustic Wave |
| CV | Cyclic Voltammetry |
| CA | Chronoamperometry |
| LSV | Linear Sweep Voltammetry |
| WE | Working Electrode |
| RE | Reference Electrode |
| CE | Counter Electrode |
| PVP | Polyvinylpyrrolidone |
| %E | Emergence Percent |
| EI | Emergence Index |
| ERI | Emergence Rate Index |

# Appendix B

# Publication and Presentations

### Publication

R.E Mfon, N.I. Odiaka, A. Sarua (2017). *Interactive effect of colloidal solution of zinc oxide nanoparticles biosynthesized using Ocimum gratissimum and Vernonia amygdalina leaf extracts on the growth of Amaranthus cruentus seeds*. African Journal of Biotechnology 16(26):1481-1489

### Presentations

Rebecca E. Mfon, Simon R. Hall, and Andrei Sarua. *Characterisation of silver and zinc oxide nanoparticles biosynthesized using Ocimum gratissimum and Vernonia amygdalina leaf extracts*. MRS Spring Meeting, Convention centre Phoenix Arizona USA., 28th March- 1st April 2016

Rebecca Emmanuel Mfon, Natasa Vasiljevic and Andrei Sarua. *Silver nanoparticles fabricated via green synthesis using plant leaf extracts*. SPIE Micro technologies VIII, Alimara Hotel, Barcelona Spain, 7th may-10th May 2017

### Poster

Rebecca Emmanuel Mfon, Dr. Simon Hall, Dr Andrei Sarua. *Characterisation of silver and zinc oxide nanoparticles biosynthesized using Ocimum gratissimum leaf extract.* Physics PG conference, University of Bristol, United Kingdom s(June, 2015).